CZECH TECHNICAL UNIVERSITY IN PRAGUE

FACULTY OF MECHANICAL ENGINEERING

DEPARTMENT OF MECHANICS, BIOMECHANICS AND MECHATRONICS

CELL MECHANICS

Dissertation

Ing. Katarína Mendová

Doctoral study programme: Mechanical Engineering

Field of study: Biomechanics

Supervisor: prof. RNDr. Matej Daniel, Ph.D.

2024 Prague

Title: Cell mechanics

Year: 2024

Author: Ing. Katarína Mendová

Supervisor: prof. RNDr. Matej Daniel, Ph.D.
Department of Mechanics, Biomechanics and Mechatronics,
Faculty of Mechanical Engineering,
Czech Technical University in Prague

University: Czech Technical University in Prague
Faculty: Faculty of Mechanical Engineering
Department: Department of Mechanics, Biomechanics and Mechatronics
Address: Technická 4, 160 00, Prague, Czech Republic

Field of study: Biomechanics

Number of pages: 86

Number of figures: 84

Number of tables: 16

Keywords: Liposomes; microfluidic device; mechanical properties; Young´s modulus; area compressibility modulus

Declaration

Herewith, I declare that the thesis comprises only my original work except where indicated, and due acknowledgement has been made in the text for all other material used.

In Prague: Signature:

Acknowledgement

I would like to thank my supervisor, prof. Matej Daniel, Ph.D., for his leadership, valuable advice, and his working deployment. Furthermore, I would like to thank my colleagues from the Faculty of Mechanical Engineering. My big thanks go to my whole family, who have always supported me and surrounded me with love.

Annotation

As revealed in the literature, there is significant variability in the mechanical properties of living cells. This variability may arise from differences in cell mechanical properties or from variations in experimental setups. To address the latter, we developed a method to manufacture artificial cells to serve as a reference in mechanical testing. In this study, liposomes produced by a microfluidic device were used as standards for testing. To correlate the measured data with the constitutive properties of biomembranes, we developed mathematical models of cell indentation based on a liquid shell description of the biomembrane. Our findings demonstrate that the mechanical properties of liposomes are significantly influenced by the test method and the data processing method used. Additionally, we observed that the commonly used Hertz model underestimates the effect of cell size.

Anotace

Z dostupné literatury o mechanice buněk vyplývá, že živé buňky vykazují různé mechanické vlastnosti. Tato variabilita může být způsobena jak samotnými mechanickými vlastnostmi, tak experimentálním testováním buněk. Pro ověření druhé možnosti jsme vyvinuli metodu výroby umělých buněk, které se pro mechanické testování používají jako referenční. V naší studii sloužily, jako reference pro testování, liposomy vyrobené pomocí mikrofluidního zařízení. Navrhli jsme také matematické modely buněčné indentace s využitím popisu kapalného pláště biomembrány tak, abychom propojili naměřená data s konstitutivními vlastnostmi biomembrány. Výsledky ukázaly, že vlastnosti liposomů jsou značně ovlivněny metodou testování a způsobem zpracování dat. Dále jsme ukázali, že běžně používaný Hertzův model podceňuje vliv velikosti buněk.

Content

List of Figures

List of Tables

List of Symbols

AM ..... additive manufacturing

DLP ..... digital light processing

FRR ..... flow rate ratio

GUVs ..... giant unilamellar vesicles

nanoDMA ..... dynamic nanoindentation

SLA ..... stereolithography

TFR ..... total flow rate ratio

A [m²] ..... contact area

a [m] ..... contact radius

a_0 [m²] ..... diameter of the inner cylinder

C_0 [nm^{-1}] ..... intrinsic curvature

C_1, C_2 [nm^{-1}] ..... principal curvatures

C_m [nm^{-1}] ..... curvatures along the meridians

C_p [nm^{-1}] ..... curvatures parallels of latitude

d [m] ..... maximum indentation depth

E [Pa] ..... Young´s modulus

E^* [Pa] ..... effective modulus

E_r [Pa] ..... reduced modulus

G [k_BT] ..... energy for the membrane

h [m] ..... height

h_0 [m] ..... initial height

H [m^{-1}] ..... mean curvature of the membrane

k [Nm^{-1}] ..... stiffness

K [m^{-2}] ..... Gaussian curvature

Ki [Nm^{-1}] ..... indentation system stiffness

Ks [Nm^{-1}] ..... specimen stiffness

K_G [J] ..... Gaussian modulus of the membrane

K_B [J] ..... Bending modulus of the membrane

K_A [J/m^2] ..... Area compressibility modulus

p [Pa] ..... pressure

p_0 [Pa] ..... pressure at the centre of the contact area

r_{c0} [m] ..... central radius

t [m] ..... cell membrane thickness

U_B [J] ..... deformation energy

U_c [J] ..... adhesion energy

U_{def} [J] ..... total deformation energy

U_S [J] ..... stretching energy

u_z [m] ..... vertical displacement

x [m] ..... displacement

γ [J/m] ..... specific surface energy

δ [m] ..... displacement of the spherical tip

ε [-] ..... relative deformation

Θ [1] ..... relative area change

ν [-] ..... Poisson's ratio

σ [Pa] ..... membrane stress

ATP ..... Adenosine triphosphate

BiotinDOPE Dioleoyl-sn-glycero-3-phosphoethanolamine

DNA ..... Deoxyribonucleic acid

DPPA ..... Dipalmitoyl phosphatidic acid

DPPC ..... Dipalmitoyl phosphatidyl choline

DPPG ..... Dipalmitoyl phosphatidyl glycerol

DPPR ..... Dipalmitoyl phosphatidyl ethanolamine

DPPS ..... Dipalmitoyl phosphatidyl serine

DSPC ..... Distearoyl phosphatidyl choline

HA ..... Hyaluronic acid

PBS ..... Phosphate buffer solution

PhL ..... Phospholipids

RNA ..... Ribonucleic acid

Introduction

All living things are built from fundamental units called cells. These cells perform a variety of essential functions, including providing structure, support, growth, transport, energy production, and reproduction [1]. Biomechanics study of how mechanical forces influence both a cell's form and function, further exploring how cells generate and respond to these physical signals [2]. By studying cellular biomechanics, we gain valuable insights into how cells interact with their surrounding environment, maintain their shape and integrity, sense and adapt to mechanical stimuli, regulate gene expression and differentiation, and ultimately contribute to tissue development and disease processes [1].

The mechanical properties of individual cells are intricately linked to crucial biological processes [3]. Consequently, alterations in these mechanical properties have been associated with various pathological phenomena and diseases [1]. Prior research has established a clear connection between the mechanical characteristics of cells and biological systems within living organisms, with specific examples including adhesion, migration, and cell division [4].

Intriguingly, research suggests that knowledge of a cell's mechanical properties and its response to specific external stimuli could play a role in the early detection of cancer [3]. Recent advancements in experimental techniques have paved the way for measuring the mechanical properties of individual cells and even their subcellular structures. Among these techniques, Atomic Force Microscopy (AFM) is the most widely used to assess cell properties. However, this technique often treats the cell as a linear elastic material characterized by a single modulus of elasticity. This approach presents limitations, as real cells are highly heterogeneous, composed of soft, non-linear materials that are difficult to accurately represent as a simple elastic continuum. Additionally, measurements of the same cell using various methods can yield significantly different results, even with repeated measurements on a single cell. This highlights the need for an engineering approach to cell measurement, one that utilizes standardized protocols while acknowledging the inherent properties of living cells.

The focus of this thesis is twofold: first, we will provide a detailed description of existing experimental methods for measuring cell mechanics. Second, we will introduce novel design, manufacturing, and testing of a novel experimental cell model. This research will involve a comparative analysis of this artificial testing standard's properties across experimental methods and data analysis approaches.

1 State of art

1.1 Cell structure

Cells (Fig. 1) exhibit remarkable structural complexity. The plasma membrane (Fig. 2) a selectively permeable barrier, encloses the cell, regulating the flow of materials. This critical structure not only protects the cell's interior but also maintains its shape and integrity. A gel-like substance called the cytoplasm fills the inner space of cell, acting as a platform for various specialized structures called organelles to carry out their essential functions. One of the most important organelles is the nucleus, typically found near the center and enclosed by its own membrane. This nucleus houses the cell's genetic material, DNA, which acts as the blueprint for everything the cell does, from growth and reproduction to its specialized tasks [5][6][7][8]. Another crucial organelle is the endoplasmic reticulum, a network of membranes that comes in two flavors: rough ER, studded with ribosomes for protein production, and smooth ER, responsible for fat metabolism and detoxification within the cell [6][7][8].

The Golgi apparatus, a network of flattened sacs, acts, modifies, sorts, and distributes proteins and lipids received from the endoplasmic reticulum, ensuring they reach their designated destinations within or outside the cell. Powering these cellular activities are the mitochondria. These double-membraned organelles generate energy in the form of ATP (adenosine triphosphate). Meanwhile, lysosomes, membrane-bound sacs filled with digestive enzymes break down waste materials, worn-out organelles, maintaining cellular hygiene and defense. Finally, ribosomes, tiny molecular machines made of RNA and protein, are responsible for protein synthesis. They translate the genetic instructions from the nucleus into functional proteins that carry out various cellular tasks [6].

The cytoskeleton, a complex network of interlinking protein filaments (microfilaments, intermediate filaments, and microtubules), provides structural integrity for the cell, maintains its shape, and facilitates essential cellular processes like movement and intracellular transport [6]. In animal cells, centrioles, barrel-shaped organelles composed of microtubules, play a crucial role in cell division. They participate in the formation of the mitotic spindle, a structure that ensures the accurate segregation of chromosomes during cell replication [6].

These cellular components function in a highly coordinated manner, each contributing specialized functionalities essential for the cell's survival, growth, and differentiated tasks within multicellular organisms. This intricate interplay between structures and their functions empowers the cell to adapt to its environment, respond to stimuli, and fulfill its designated roles within complex biological systems [6].

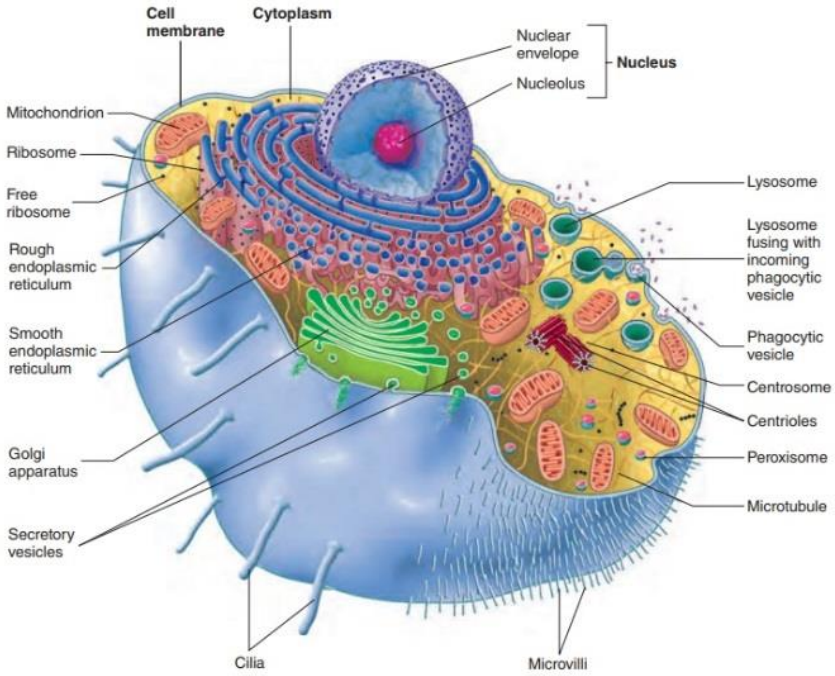

Fig. 1 Cell structure [7]

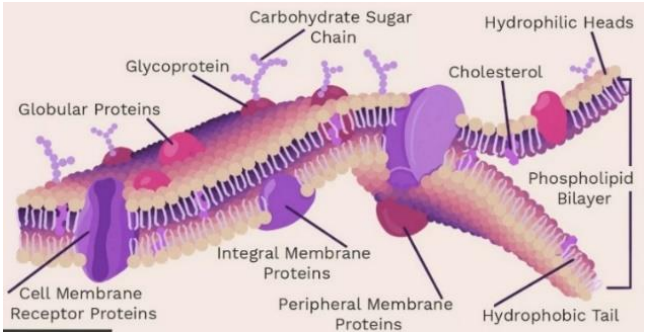

Fig. 2 Cell membrane structure [8]

1.2 Liposome as a basic cell model

Liposomes (Fig. 3) are colloidal, vesicular structures consisting of one or more concentric bilayers formed from phospholipids [9]. Liposomes can be categorized based on various structural parameters, allowing for tailored design for specific applications [10].

Unilamellar vesicles, categorized by size as small unilamellar vesicles (SUVs; 20-100 nm), large unilamellar vesicles (LUVs; 100-250 nm), and giant unilamellar vesicles (GUVs; 1-100 µm). They offer a valuable tool for studying cell membrane mechanics due to their similar size range to cells and hence can be consist of a single phospholipid bilayer, mimicking the fundamental structure of the cell membrane [9][10].

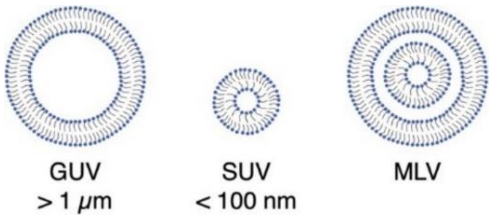

Fig. 3 Classification of liposomes [11]

1.2.1 Phospholipids

Phospholipids are amphipathic molecules. They possess a unique structure consisting of a glycerol backbone, a phosphate group, and two fatty acid tails [9].This structure allows them to self-assemble into bilayers in an aqueous environment. The hydrophilic head group, composed of the glycerol and phosphate moiety, is attracted to water due to its polarity. Conversely, the hydrophobic fatty acid tails, which can be saturated or unsaturated, are uncharged and tend to avoid water [9].

Tab. 1 Synthetic phospholipids [10]

DPPC	Dipalmitoyl phosphatidyl choline
DSPC	Distearoyl phosphatidyl choline
DPPR	Dipalmitoyl phosphatidyl ethanolamine
DPPS	Dipalmitoyl phosphatidyl serine
DPPA	Dipalmitoyl phosphatidic acid
DPPG	Dipalmitoyl phosphatidyl glycerol

As shown in Fig. 4, the phospholipid bilayer is a well-defined structure formed by the assembly of numerous phospholipid molecules. This unique arrangement of hydrophilic and hydrophobic domains is essential for the selective permeability and barrier function of the cell membrane [10].

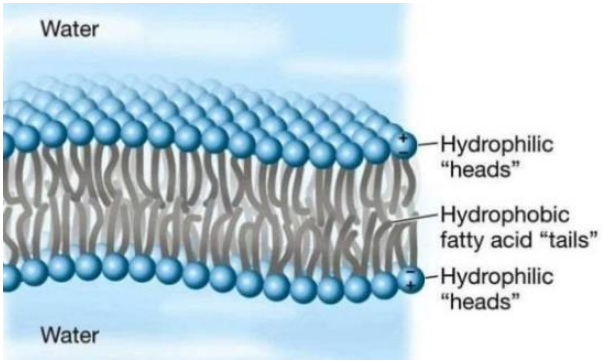

Fig. 4 Phospolipid bilayer [12]

1.3 Methods of giant liposome preparation

Giant unilamellar vesicles (GUVs) have been widely accepted as artificial cell models due to their comparable size range to real cells [11] [13]. The first step in liposome formation is to thoroughly mix and dissolve the lipids in an organic solvent [14]. If a water-miscible organic solvent is used, liposomes can be formed by subsequently mixing the alcoholic lipid solution with an aqueous phase. The aim of this process is to obtain a clear and homogeneous lipid solution. Fig. 5 illustrates various methods of liposome production, including both conventional techniques and recently introduced in microfluidic approaches [13].

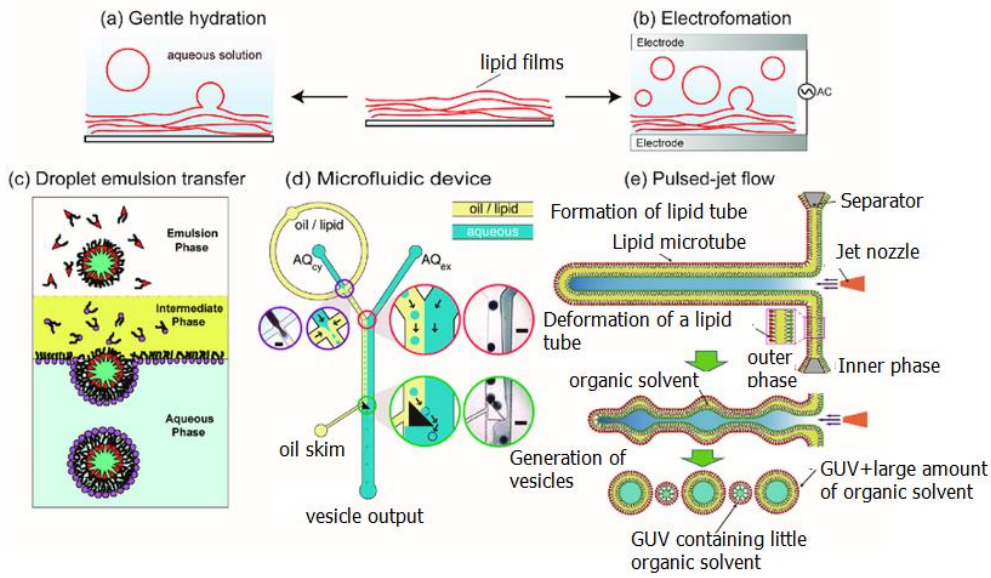

Fig. 5 Illustration of giant liposome formation (a) gentle hydration method (b) electroformation method (c) droplet emulsion transfer method (d) microfluidic devices of cell-sized lipid vesicle formations (e) pulsed-jet flow method [13]

1.3.1 Gentle hydration method

Lipid solutions are typically prepared at concentrations of 10-20 mg/ml in a chosen organic solvent [15]. The gentle hydration technique involves the application of chloroform-dissolved phospholipids to a glass microtube. The solvent is then evaporated under a stream of argon or nitrogen gas, resulting in the formation of a thin lipid film [15]. This film is then hydrated with an aqueous solution, such as pure water or phosphate buffered saline (PBS). This hydration step triggers the self-assembly of the lipids into giant unilamellar vesicles (GUVs) with diameters ranging from 1 to 100 µm [10][13]. Conversely, smaller nano-sized liposomes can be obtained by subjecting the lipid films to vigorous mixing techniques such as vortexing or sonication [10][13]. The typical hydration time for GUV formation is approximately 1 hour. Fig. 5 (a) and Fig. 6 illustrate the key steps in this preparation process [15].

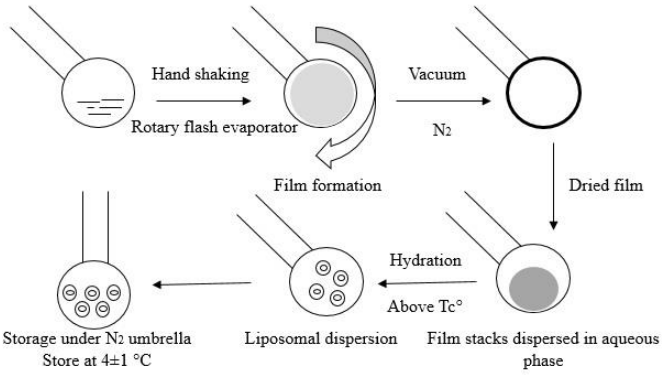

Fig. 6 Lipid hydration method - handshaking method

Sonication, as shown in Fig. 7, is a commonly used technique for the preparation of SUVs, typically yielding vesicles with diameters in the range of 15 to 50 nm [10][15]. Two primary instruments are used for sonication: probe-tip sonicators and bath sonicators. Probe-tip sonicators deliver a high energy input to the lipid suspension, but this can lead to overheating and degradation of the lipids. In addition, probe tips can release titanium particles into the suspension, requiring their removal prior to

centrifugation [15]. In contrast, bath sonication involves placing a test tube containing the lipid suspension in a bath sonicator for 5-10 minutes.

The resulting suspension typically appears slightly cloudy due to the presence of larger residual particles [10]. These larger particles are then removed by centrifugation to obtain a clear suspension of purified SUVs (small unilamellar vesicles) [10][15].

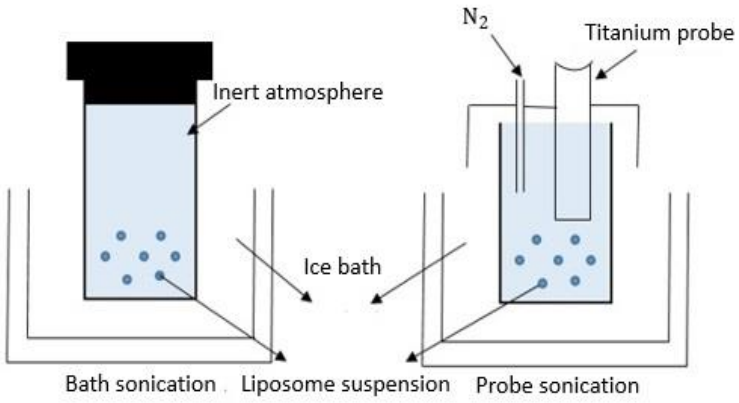

Fig. 7 Sonication

1.3.2 Eletroformation

Lipid films are prepared using a droplet deposition technique [13][16]. The lipid layer is then deposited onto an indium tin oxide coated glass surface by electroforming. An alternating current electric field is then applied to induce hydration of the lipids within the films, particularly those containing hydrated solutions such as pure water or low salt phosphate buffered saline (PBS), eletroformation is shown in Fig. 5 (b) [13][16].

1.3.3 Droplet emulsion transfer method

Liposome formation is achieved by a two-step process. First, water-in-oil (w/o) emulsions are prepared by either vortex focusing or sonication. These emulsions consist of an aqueous phase containing PBS and a phospholipid solution dissolved in an organic solvent, typically mineral oil. The w/o emulsions are then added to the oil phase in a microtube. In the final step, the w/o emulsions are added to a preformed lipid monolayer located at the interface between the oil and aqueous phases. This process triggers the formation of liposomes as shown in Fig. 5 (c) [13].

1.3.4 Microfluidic method

Microfluidic hydrodynamic focusing (MHF), shown in Fig. 5 (d) and Fig. 8 is a technique used to produce liposomes with a uniform size distribution [17][18][19]. This method allows precise control of liposome size by manipulating the flow rate ratio (FRR) and total flow rate ratio (TFR) between the water streams and the lipid solution. The lipids dissolved in the organic solvent (typically alcohol) diffuse into the aqueous phase until the alcohol concentration falls below a critical threshold [17][18][19].

Several factors influence the final size of the liposomes: crossflow ratios, lipid composition and concentration, variations in fluid flow rates due to viscosity differences, and the dimensions of the microfluidic channels [17][20]. Both the FRR between the lipid and water phases and the TFR can be adjusted to regulate the size of the focused stream in which liposome formation occurs [21].

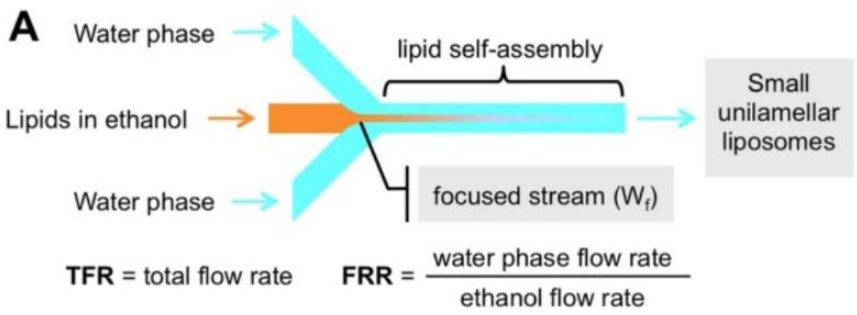

Fig. 8 MHF technique [17]

1.3.5 Bulk method

Bulk method (Fig. 9) of producing liposomes involves the rapid injection of a lipid solution dissolved in solvents such as chloroform or methanol into a large volume of buffer. However, this technique has several drawbacks. Firstly, the resulting liposomes exhibit significant heterogeneity in size and morphology. Secondly, the liposomes produced are highly diluted, requiring further concentration steps. In addition, the complete removal of the organic solvent, often ethanol, proves challenging due to its formation of an azeotrope with water [17].

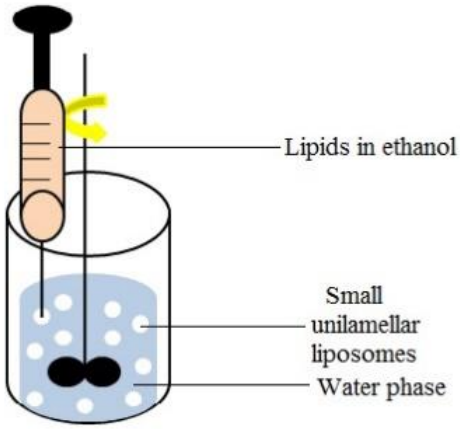

Fig. 9 Bulk method of liposomes production

1.3.6 Pulsed jet flow method

Monodisperse giant unilamellar vesicles (GUVs) with diameters ranging from 300 µm to 600 µm can be produced using a pulsed jet flow technique in conjunction with the droplet contact method, as shown in Fig. 5 (e) [13][22].In this method, a pulsed jet flow generated by a microjet is directed at a planar lipid bilayer. The force exerted by the jet flow stretches the bilayer, ultimately leading to the formation of free vesicles. The size of these vesicles can be precisely controlled by manipulating the duration of the jet flow application. By repeating this process, significant volumes of monodisperse GUVs can be obtained [13][22].

2 Mechanical testing of cells and vesicles

Cellular mechanics play a crucial role in numerous biological processes. Deviations from these mechanical properties are often associated with various pathological conditions and diseases. Individual cells are constantly exposed to external mechanical forces that can affect their morphology and internal architecture. To gain insight into these complex relationships, researchers employ specialized tools to quantify the mechanical properties of individual cells.

2.1 Force application techniques

The force probe technique is a powerful tool in cell mechanics research. It uses nanoscale probes, such as micropipettes, cantilevers, or beads, to apply or measure forces at the cell surface or even to manipulate structures within the cell. These probes can be attached to specific targets such as the cell membrane, the cytoskeleton, or individual molecules. The application of force is precisely controlled by a piezo actuator, a magnetic field, or an optical trap. The deflection of the probe, carefully monitored by a camera, laser, or interferometer, allows the force applied to be calculated from the known stiffness of the probe. This technique provides valuable insights into the mechanical properties and interactions between cells and molecules, as well as revealing the cellular response to external stimuli and environmental changes [23][24][25].

Fig. 10 provides a comprehensive overview of the various test methods used to characterise cell mechanics. Atomic force microscopy (AFM), nanoindentation and compression testing are described in more detail.

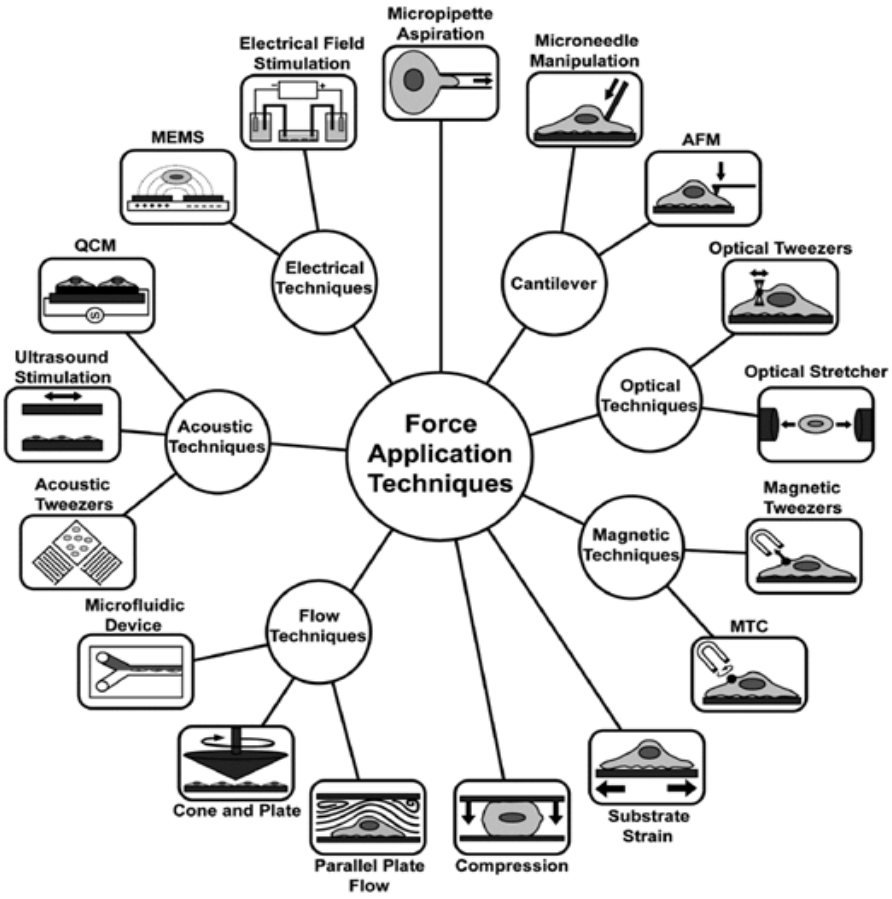

Fig. 10 Force application techniques [23]

2.1.1 Atomic force microscopy (AFM)

The basic principle of AFM, as shown in Fig. 11 relies on the detection of minute forces between a sharp probe tip attached to a flexible cantilever and the sample surface [26][27]. During the scanning process, the cantilever deflects in response to the prevailing repulsive or attractive forces between the tip and the sample, as determined by their separation distance [28]. A laser beam is reflected from the back of the cantilever onto a photodiode, which accurately measures the magnitude of this deflection [27][28]. To maintain a constant deflection, a feedback mechanism continuously adjusts the height of the cantilever, effectively ensuring that the tip closely follows the surface topography. By recording the height of the cantilever as it traverses the sample, a high resolution image of the surface topography is generated.

The force interaction between the tip and the sample can be calculated from the known stiffness of the cantilever and the measured deflection. By systematically varying the tip-sample distance, a force-distance curve can be obtained. This curve provides valuable insight into the mechanical properties and intermolecular interactions within the sample [29].

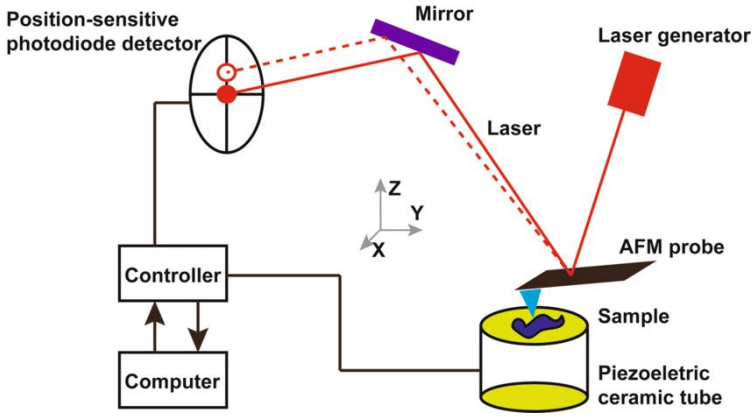

Fig. 11 A schematic representation of AFM measurement [29]

The choice of AFM tip material and geometry is dependent on the intended measurement and the sample properties [30]. Traditional AFM tips used to characterise the elastic properties of biological samples often adopt pyramidal, spherical, or cylindrical shapes, as shown in Fig. 12. Conversely, sharp silicon tips are generally preferred for high resolution topographic mapping of solid surfaces. Specialised applications may require the use of tips made from alternative materials such as epoxy resin or acrylic [30].

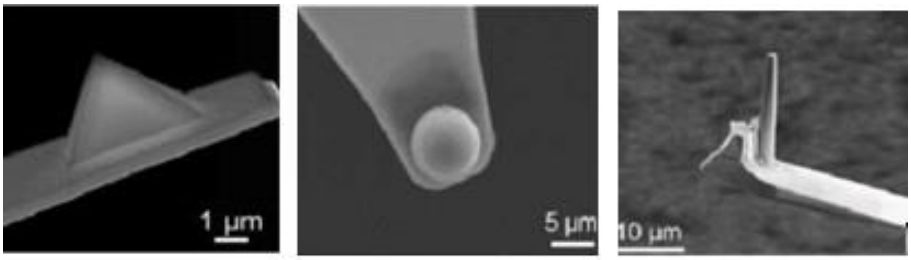

Fig. 12 Types of AFM tips [30]

Analysis by AFM microscopy can be carried out in several different modes (Fig. 13).

(a) Contact mode (static mode) – (< 0.5 nm probe-surface separation) the most common mode for AFM measurements, a soft "physical "contact is made between the AFM tip and the surface being measured. The deflection of the cantilever is proportional to the force applied, according to Hook's law [31].

(b) Tapping mode (dynamic mode, intermittent contact, alternating current mode, or vibrating mode) – (0.5–2 nm probe-surface separation) – an important mode for AFM imaging. It enables high-resolution imaging of a sample surface. The cantilever oscillates, bringing the tip into contact with the surface to achieve high resolution [31].

(c) Noncontact mode (frequency modulation mode) – (0.1–10 nm probe-surface separation) – in this mode, the cantilever is in close contact with the sample (a few nanometres). The probe vibrates and changes in frequency are used to detect the surface structure of the sample [31].

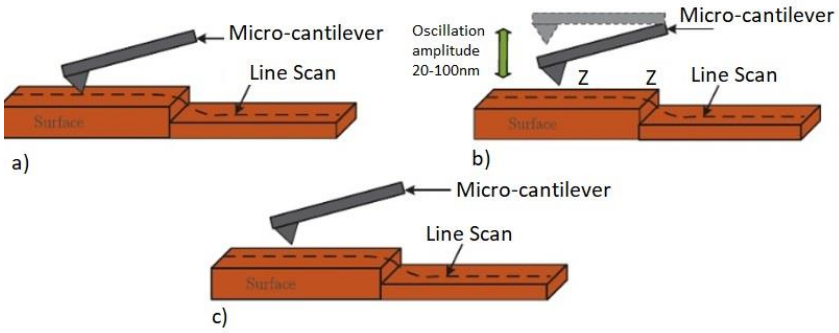

Fig. 13 Operating modes of the AFM: (a) contact mode (b) tapping mode (c) noncontact mode [31]

The result of the AFM measurement is represented by the force-distance curve, which illustrates the interaction between the sample and the surface under investigation (Fig. 14).

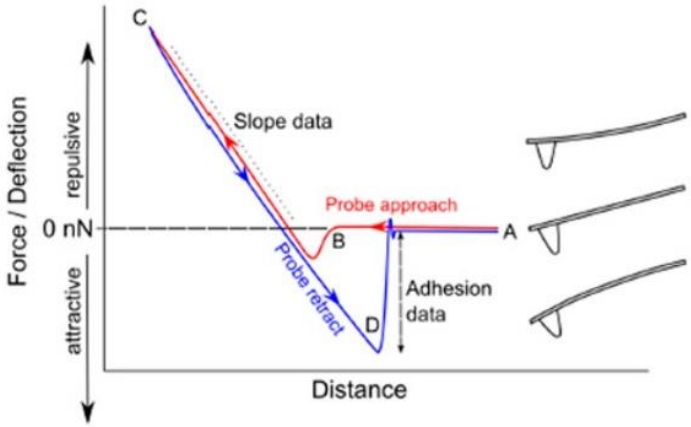

Fig. 14 AFM force-distance curve [32]

2.1.2 Nanoindentation

Nanoindentation is a technique based on technical hardness testing methods defined by Rockwell, Brinell, and Vickers (Fig. 15) [33].

Parameter	Berkovich	Cube-corner	Cone	Spherical	Vickers
Shape					
C-f angle	65.35°	35.264°	—	—	68°
Projected Contact area	$24.5600d^2$	$2.5981d^2$	πa^2	πa^2	$24.5044d^2$

Fig. 15 Indentation tips [34]

Nanoindentation has emerged as a method for characterising the mechanical properties of materials at the nano and microscale [35][36][37]. A typical nanoindentation instrument consists of a rigid frame, a motorised stage to facilitate sample handling, an optical microscope for sample visualisation and selection, and a scanning head mounted on the scanner, as shown in Fig. 16.

The basic principle of nanoindentation is to press a diamond indenter, typically pyramidal or spherical in shape, into the material of interest with a continuously increasing load until a predefined level is reached [37].

The force exerted by the tip on the sample is induced either electrostatically or via a magnetic field. The resulting relationship between the total indentation load and the corresponding displacement or contact area can then be used to determine the hardness of the material. The geometry of the tip selected is used to calculate the size of the contact area formed during the test [37].

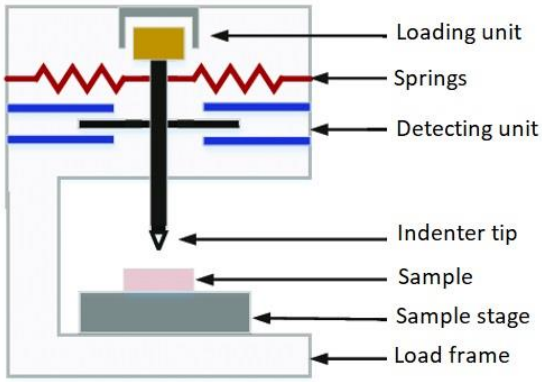

Fig. 16 Nanoindenter instrument schematic [38]

Due to the large variability of the movement of the indicator tip, measurements can be carried out in a few different modes.

a) Quasi-static nanoindentation – currently the most used method. Performed in a highly controlled manner by applying and removing a load to a specimen [35][36][39]. This highly controlled technique involves the application and subsequent removal of a load to the material of interest. The data acquired is typically presented as an indentation curve, which shows the force dependence on the displacement experienced by the material (Fig. 17). This highly controlled technique involves the application and subsequent removal of a load to the material of interest. The data obtained is typically presented as an indentation curve, which shows the force as a function of the displacement experienced by the material [40].

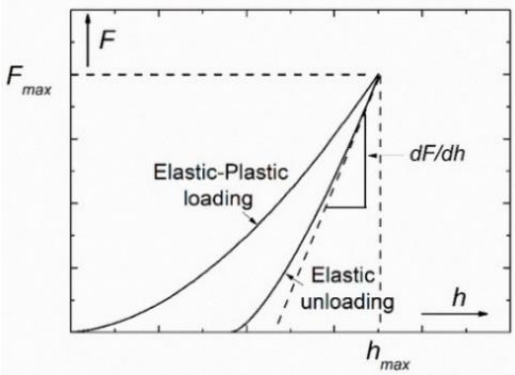

Fig. 17 Load-depht indentation curve [40]

b) nanoDMA applies oscillating force to a sample and the resultant displacement amplitude and phase shift are measured. Using this technique, the contact stiffness and damping properties of

the material can be accurately determined. Additionally, this technique could expand to include additional testing modes for characterizing creep and inducing fatigue in a wide variety of materials. Evaluation of results is based on a simple one-degree-of-freedom model of the indented specimen which includes the specimen stiffness Ks and damping Cs, and the indentation system stiffness Ki and damping Ci, shown in Fig. 18. A significant advantage of the nanoDMA mode is the possibility of conducting measurements across a larger sample area through the implementation of modulus mapping techniques. This capability represents a unique combination of dynamic testing and in-situ imaging functionalities [41].

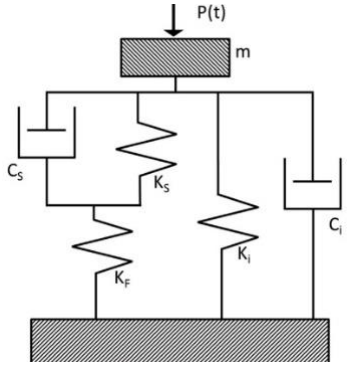

Fig. 18 Dynamic indenter model [42]

2.1.3 Cell compression testing

Compression testing using a nanoindentation device is proving to be a valuable tool for investigating the mechanical behaviour of individual cells. This technique uses a flat probe to compress a cell. In most cases, the compressive load is applied in a displacement-controlled mode over a period of a few seconds [43][44]. The resulting indentation curve, obtained by quasi-static nanoindentation, allows the forces applied, the energy dissipated and the true deformation to be determined. A schematic representation of the compression test is shown in Fig. 19 [44].

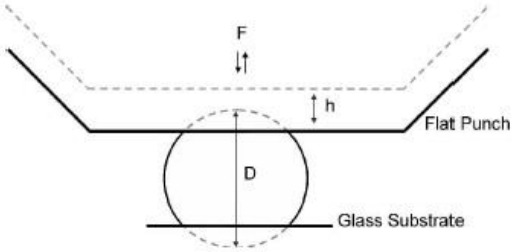

Fig. 19 Schematic diagram of the compression testing [44]

The measurement process begins with immobilization of test cells to a glass substrate, followed by their immersion in phosphate buffer solution (PBS) [46]. A light optical microscope is then used to identify a single cell for the experiment. Using a staging system, this selected cell is precisely manoeuvred into position under a flat punch. The pre-selected load function is then applied to initiate the compression test. The resulting force-displacement data acquired during the loading phase typically exhibits three distinct stages, as shown in Fig. 20 [44]. These stages are thought to correspond to different cellular deformation processes and provide valuable insight into the mechanical behaviour of cells under compressive stress. In particular, the three stages are thought to represent: cell compression, cell rupture and finally the compression of the ruptured cell [44].

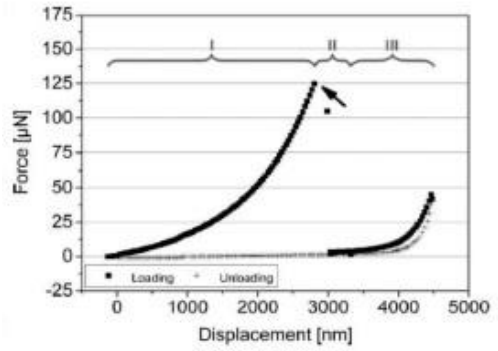

Fig. 20 Force-displacement curves of a brust cell [44]

2.1.4 Micropipette aspiration

Micropipette aspiration, Fig. 21 is a cost-effective technique that is ideally suited for investigating the mechanical properties of whole cell and vesicle membrane deformation [28][45]. During a micropipette aspiration experiment, a controlled suction is applied to the membrane, causing it to be partially or completely drawn into a micropipette - a glass tube with a precisely defined internal diameter. Notably, the diameter of the micropipette is significantly smaller than that of the vesicle under investigation [28][45]. As suction is progressively applied, the membrane slips and deforms within the confines of the micropipette.

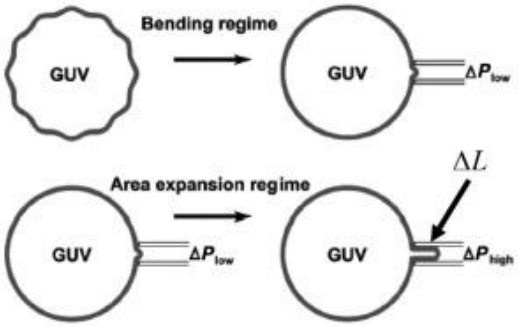

Fig. 21 Micropipette aspiration [28]

Fig. 21 shows the tension-strain measurement of a GUV in two different regimes: the bending regime (top) and the area-expanding regime (bottom). In the bending regime, the GUV is partially drawn into a glass micropipette, causing bending and deformation of its lipid bilayer membrane in response to applied suction. Conversely, in the expansion regime, the GUV is fully drawn into the glass micropipette, causing stretching and expansion of its lipid bilayer membrane as applied suction increases [28].

2.1.5 Optical tweezers

Optical tweezers leverage tightly focused laser beams to manipulate and confine microscopic particles with exceptional precision [28]. This technique relies on the creation of a light intensity gradient within the focused laser beam. This gradient exerts a force that draws minute particles, such as microscopic beads or even whole cells, towards the beam's central region, where they become trapped. By meticulously controlling the position and intensity of the laser beam, researchers can achieve three-dimensional particle manipulation and exert precisely controlled forces on the trapped objects. Notably, optical tweezers offer sub-millisecond time resolution, enabling the acquisition of three-dimensional displacement measurements with remarkable temporal resolution. Furthermore, unlike

techniques such as AFM or MA, this method eliminates the need for direct contact with the sample, minimizing potential artifacts [28][46].

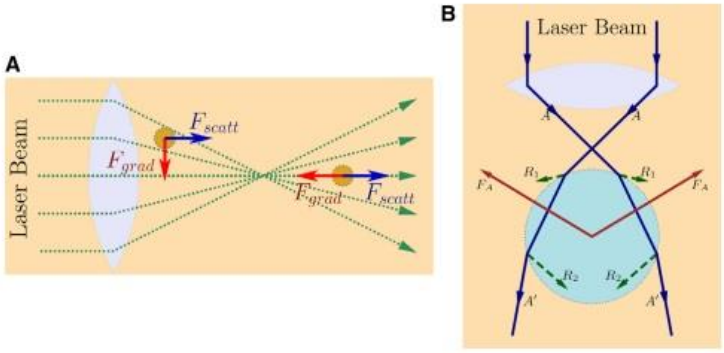

Fig. 22 Optical tweezers [28]

Fig. 22 (A) illustrates the principle of three-dimensional light gradient confinement, where a microscopic particle is drawn towards the diffraction-limited beam waist of a focused laser beam [28]. Fig. 22 (B) depicts a scenario where the vesicle dimensions exceed the incident laser wavelength. In this case, the emergent refracted rays denoted by A' contribute to the momentum balance within the system, giving rise to the emergence of backward forces acting on the vesicle [28].

2.1.6 Magnetic tweezers

Magnetic bead rheometry, also known as magnetic tweezers, uses paramagnetic microbeads and localised magnetic fields to manipulate biomolecules [28][47]. These microbeads are strategically attached to a cell or vesicle membrane, allowing them to be manipulated by precisely controlled magnetic fields. By varying the frequency and intensity of the applied magnetic field, researchers can probe different membrane behaviours, such as creep compliance [28][47]. A key advantage of this technique is its ability to establish controlled and specific binding between the beads and the cell membrane. This facilitates precise manipulation and measurement during the experiment, minimising potential artefacts [28].

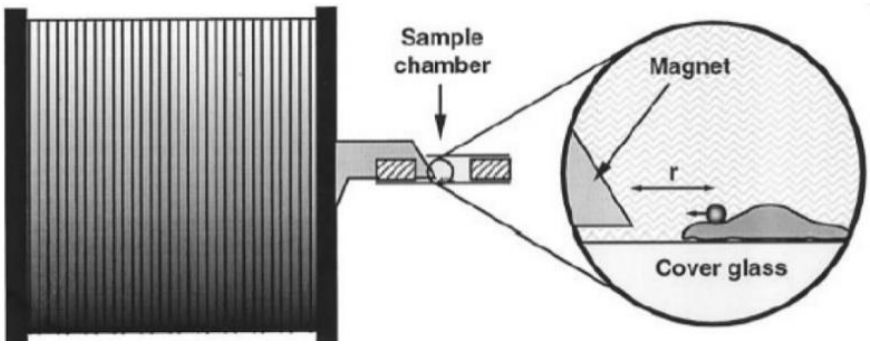

Fig. 23 Magnetic bead rheometry [47]

Fig. 23 shows a magnetic bead rheometer. The movement of the bead can be controlled by activating and deactivating the electromagnet [47].

2.2 Force sensing techniques

In contrast to force application techniques, force-sensing techniques focus on the detection of forces exerted by cells or biological molecules without necessarily applying external forces to the system under investigation [23].These techniques are commonly used to quantify the forces generated by a cell as it interacts with its environment. As shown in Fig. 24, force-sensing techniques can be used to measure cellular forces in static environments. In addition, they have the versatility to be combined with force application techniques for more comprehensive studies [23].

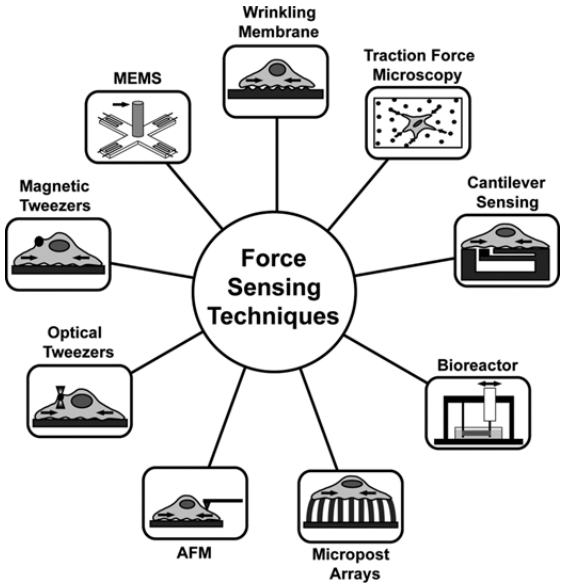

Fig. 24 Force sensing techniques [23]

2.2.1 Traction force microscopy

Traction force microscopy (TFM), also known as particle tracking microrheology, is a technique that investigates cellular forces exerted on the surrounding environment [23]. This method involves seeding the cell onto or within a polymeric gel substrate that is densely populated with microscopic beads. TFM, Fig. 25 can be further enhanced by integrating laser scanning confocal microscopy, enabling the measurement of three-dimensional tensile forces exerted by the cell. The tensile forces are estimated by tracking the displacement of these embedded beads, considering the known elastic stiffness of the substrate material. When a flexible, homogeneous, isotropic, and linear elastic material is employed for the substrate, the relationship between the applied tensile stress field and the resulting displacement field can be directly determined based on the material's inherent properties [23][48].

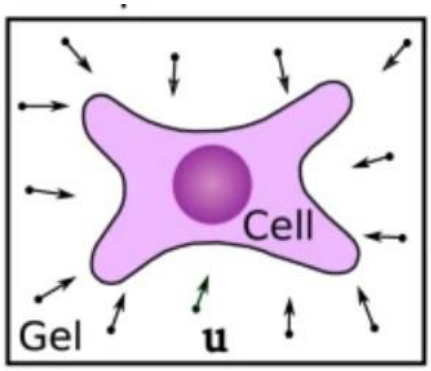

Fig. 25 Traction force microscopy [48]

3 Evaluation of measurements

3.1 Hertz contact model

A fundamental assumption underlying the Hertz model for contact mechanics analysis is that the biological cell under investigation exhibits ideal elastic behaviour, is isotropic and homogeneous [49]. In addition, the model assumes that the indentation depth remains relatively small compared to the overall dimensions of the cell [50].

3.1.1 Contact between a rigid sphere and an elastic half-space

Fig. 26 shows a schematic illustration of the contact between a solid sphere and a flexible half-space. In schema the displacement of points on the surface within the contact region is shown [51].

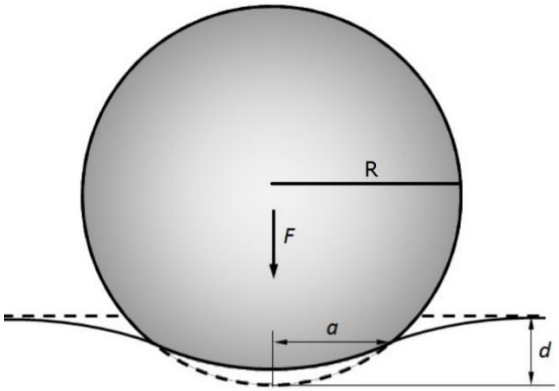

Fig. 26 A rigid sphere in contact with an elastic half-space

The displacement of the points on the surface within the contact area A_c, where an initially flat surface and a rigid sphere with radius R come into contact, is equivalent to:

$$u_z = d - \frac{r^2}{2R} \qquad (1)$$

where r is radial coordinate and d is the maximum indentation depth. Hertz suggested a quadratic distribution of pressure [51][52]:

$$p = p_0\left(1 - \frac{r^2}{a^2}\right)^{\frac{1}{2}} \qquad (2)$$

where a is the radial size of the contact and p_0 is the maximum contact presssure. It follows from theoretical analysis of point force [53], that vertical displacement u_z at the surface equals to:

$$u_z = \frac{\pi p_0}{4E^* a}(2a^2 - r^2), r \leq a \qquad (3)$$

where E^* is the reduced modulus defines as:

$$E^* = \frac{E}{1 - \nu^2} \quad (4)$$

Where E is the elasticity modulus of the sample, ν is the Poisson ratio and that indentor behaves as rigid body, i.e. its modulus of elasticity is much higher than eleasticity modulus of the sample. The total force acting on the area under pressure is related to the contact pressure distribution (2) as:

$$F = \int_O^a p(r) 2\pi r dr = \frac{2}{3} p_0 \, \pi a^2 \quad (5)$$

By using equation (1) and (3) it could be obtained:

$$\frac{1}{E^*} \frac{\pi p_0}{4a} (2a^2 - r^2) = d - \frac{r^2}{2R} \quad (6)$$

The variables a and d could be obtained from Eq. (5) and Eq. (6):

$$a = \frac{\pi p_0 R}{2E^*}, \; d = \frac{\pi a p_0}{2E^*} \quad (7)$$

This results in the contact radius:

$$a^2 = Rd \quad (8)$$

And the maximum pressure:

$$p_0 = \frac{2}{\pi} E^* (\frac{d}{R})^{\frac{1}{2}} \quad (9)$$

Equations (8) and (9) are substituted into equation (5) to calculate the force [49][51]:

$$F = \frac{4}{3} E^* (R)^{\frac{1}{2}} (d)^{\frac{3}{2}} \quad (10)$$

where the indentation displacement d is considerably smaller than the tip radius R. By having information about the dimensions of the indenter and the sample's Poisson's ratio, the Young's modulus can be readily determined as a fitting parameter [49][51][54].

Using equations (9) and (10), we can determine the pressure at the centre of the contact area and the contact radius as a function of loading force F[51]:

$$p_0 = (\frac{6FE^{*2}}{\pi^3 R^2})^{\frac{1}{3}}, \; a = (\frac{3FR}{4E^*})^{\frac{1}{3}} \quad (11)$$

We can also determine the formula for the potential energy resulting from elastic deformation, denoted by U. By applying the equation: $-F = -\frac{\partial U}{\partial d}$, we derive the following expression for U [51]:

$$U = \frac{8}{15} E^* (R)^{\frac{1}{2}} (d)^{\frac{5}{2}} \quad (12)$$

3.2 Overbeck model

In contrast to the techniques discussed previously, models based on shell theory focus on determining the mechanical properties of the cell membrane rather than the entire cell itself. These models assume that the cell is a linearly elastic membrane - a material that deforms proportionally to applied stress up to a certain limit. During compression, the model assumes that the cell behaves like a fluid-filled sac with a constant internal volume [55]:

$$\sigma_e = p\frac{D}{4t} \quad (13)$$

$$\sigma = E.\varepsilon \quad (14)$$

$$\varepsilon = \ln(\frac{D}{D_0}) \quad (15)$$

where σ represented by the membrane stress. A linear elastic behaviour of the cell is assumed, and Hooke's law is applying, E is the Young's modulus of the membrane and ε is the relative deformation. The relative strain is determined as the logarithm of the ratio of the instantaneous largest cell circumference D to the initial cell diameter D_0. A constant cell volume is also assumed throughout compression test. During the compression of the cells is not allowed any changes in the volume of cell [55].

Two simple geometries, namely the barrel-like geometry (BG) and the filled torus geometry (FTG), are known and shown in Fig. 27. When calculating the initial volume, the inner diameter of the cell is considered because the cell membrane is located on the inside of the cell wall and functions as an osmotic barrier [55].

The reaction force is calculated by the contact area a and the pressure p [55]:

$$F = \frac{\pi}{4}\, a^2 p \quad (16)$$

Where, where a is the diameter of the inner cylinder of the full toroid during the compression [55].

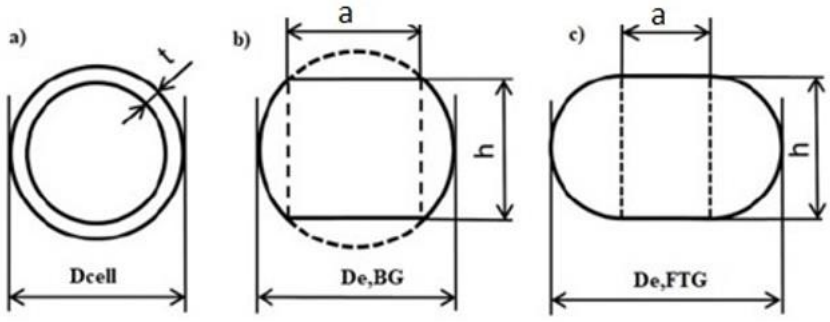

Fig. 27 (a) Initial model cell geometry, (b) BG, (c) FTG [55]

3.3 Canham-Helfrich model

In analysis of membrane mechanics Canham-Helfrich model is a cornestone comprehending the shapes of biological membranes. The principle of model is based on assumtpon that membranes achieve their equilibrium shapes by minimizing their total energy. The model assumes a membrane without lateral tension energy and the membrane is deformed in pure bending. The amount of bending energy depends on the deformation, in case of two-dimensional membrane surface in three-dimensional space described by its curvature, or more exactly by the Riemann curvature tensor. As the energy is scalar quantity, it must be invariant to the rotation, i.e. the total energy is a sum of the tensor invariants. The Helfrich, 1973 and Canham, 1970 used a first invariant to describe bending energy. The total bending energy for the membrane is hence expressed as the sum of the strain energies of the individual curvatures [56][57]:

$$G_{bend} = \frac{1}{2} K_B \int_A (C_1 + C_2)^2 d_A \qquad (17)$$

where the sum of the principal curvatures $C_1 C_2$ is the Gaussian curvature K and K_G is the Gaussian modulus of the membrane. Similarly, $C_1 + C_2$ is a measure of the mean curvature of the membrane $H = (C_1 + C_2)/H$ and can be denoted by as $2H$. From the above, we obtain a formula for expressing the bending strain energy of the membrane as:

$$G_{bend} = \frac{1}{2} K_B \int_A (2H)^2 \, dA - K_G \int_A (C_1 C_2) dA \qquad (18)$$

The advantage of this notation is the potential to application of the Gauss-Bonnet theorem for the Gaussian curvature term. This theorem states that the integral of the Gaussian curvature of a body with a given topology over a closed surface is constant. Therefore, one can neglect the Gaussian curvature term in the calculation of the minimum strain energy is possible if the topology of the membrane is unchanged.

The above relation for the membrane energy is valid only for a planar membrane that reaches minimum energy assuming $C_1 = C_2 = 0$. It is known that certain lipids can generate spontaneous curvature of the membrane by their shape or asymmetric insertion into the lipid bilayer. Lipids with a large surface area ratio of functional head group to hydrocarbon chains produce positive curvature, while lipids with the opposite ratio produce negative curvature. Negative curvature can also be induced by the insertion of a molecule with a large hydrophobic part such as cholesterol [58]. According to Helfrich, 1973 [59] this relationship can be modified by including the so-called intrinsic curvature of the membrane C_0:

$$G_{bend} = \frac{1}{2} K_B \int_A (2H - C_0)^2 \, dA - K_G \int_A (C_1 C_2) dA \qquad (19)$$

The intrinsic curvature of the membrane is equal to twice the mean intrinsic curvature $2H$ of the monolayer of the membrane, i.e. it is the curvature at which the membrane bending energy is zero [60].

4 Mechanical properties of cells and vesicles

The cell is composed of numerous components, each exhibiting distinct mechanical properties. Fig. 28 illustrates the various cellular components along with representative values of their mechanical properties. Additionally, the mechanical properties of cells are influenced by their surrounding environment and the external forces exerted upon them.

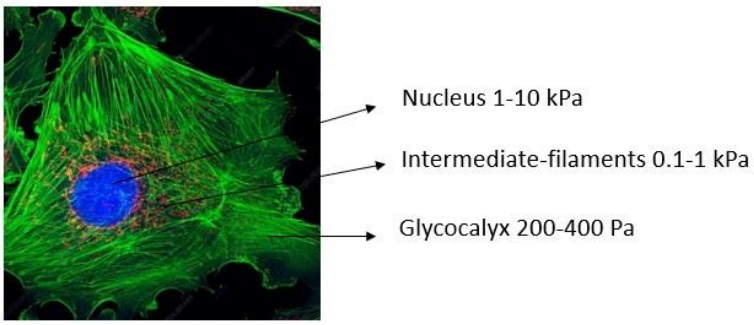

Fig. 28 Young´s modulus of the different parts of cells [61][62]

Tab. 2 Summary of the main mechanical properties of vesicles (EV_s)

Property	Symbol	Units	Definition	Features	References
stiffness	k	$N \cdot m^{-1}$	The resistance to deformation caused by an applied force.	Extrinsic property Dependent on EV geometry Obtained from linear fit on force-indentation curve.	[62][63]
Young's modus	E	Pa	A measure of the relationship of stress and strain in the linear elasticity region of deformation along a single axis	Intrinsic property Independent of EV geometry Extracted from force-distance curves using Hertz model, Thin Shell Model	[62][63][64]
Bending modulus	K_B	J	Energy required to deform bilayer from its intrinsic curvature to a different curvature.	Intrinsic property Independent of EV geometry Extracted from force-distance curves using Thin Shell Model or Canham Helfrich Theory	[63][64][65]
Area compressibility modulus	K_A	J/m^2	A measure of a material's	Mechanical properties of cells, vesicles	[66]

			resistance to compression in two dimensions. It quantifies the change in surface area of a material in response to applied pressure.	Extracted from force-distance curves.	

Tab. 3 Summary of the mechanical indentation models

Indentation Model	**Summary**	**Benefits**	**Drawbacks**	**Ref.**
Hertz model	EV assumed to be elastic, infinitely large, homogenous in composition. No interactions between tip/sample	Independent of EV size Simple	Only valid for small indentations Assumed homogeneity not valid for EVs	[63][67][68] [69][70]
Thin Shell	Bilayer membrane treated as a single mechanical layer. EV is assumed to be filled with incompressible fluid	Accounts for membrane's unique mechanical response	Only valid for small indentations EVs do not have hollow interior. Sensitive to assumed vesicle size and membrane thickness	[63][71][72]
Modified Canham Helfrich	Accounts for bending of bilayer membrane	Valid for all indentation displacements	Labour-intensive Clean tether force needed on retract curve	[63][73]

Tab. 4 The mechanical indentation models applied to extracelular vesicles (EV_s)

Indentation Model	**Vesicle**	***E* (MPa)**	***κ* (kBT)**	***K* (mNm^{-1})**	**Ref.**
Hertz model	Phosphatidylcholine	1.97 ± 0.75			[63][67][68]
	Cholinergic Synaptic Vesicles	0.2-1.5			[63][68]
	Savila EV	0.89 ± 0.07			[63][69]
	Exomere	145-816			[63][70]
	Large EV	26-73			[63][70]
	Small EV	70-420			[63][70]
Thin Shell	Human malignant metastatic bladder cell derived EVs	280			[63][71]
	Human malignant nonmetasta-tic bladder cell derived EVs	95			[63][71]
	Human nonmalignant nonmetastatic bladder cell derived EVs	1527			[63][71]
	Mouse hepatocyte EVs			49 ± 12	[63][72]
	Rat hepatocyte EVs			13 ± 9	[63][72]
Modified Canam Helfrich	Red blood cell derived EV		15 ± 1	Varied between patient samples	[63][73]
	Hereditary spherocytosis EV		9 ± 1	11 ± 2	[63][73]

5 Aims

The mechanical characteristics of cells correlate with their condition and function, making them an inherent biophysical indicator of cell states. This includes processes like cancer cell metastasis, leukocyte activation, or advancement through the cell cycle. Cytoskeletal mechanics is a field that heavily relies on mathematical models to interpret experimental data related to forces and deformations. However, in most of the studies cells are usually described as an elastic homogeneous material. Other factors such as cytoskeleton properties, cell size, and shape, as well as the effect of environment are usually neglected. In addition to the intrinsic variations in cell properties, the method of measurement and evaluation could also affect the estimated material properties. Nowadays, there is no explicit comparison between various methods in terms of repeatability and comparability. These uncertainties are driven by large variations in mechanical properties among the cell cultures or even within the same cell measured at various positions or time intervals.

Therefore, the aim of this work is to esablish a method that will provide a cell model serving as mechanical standard for evaluation of cell mechanics and use this model to verify current approaches adopted in cell mechanical testing.

The specific aim of the thesis consists of adopting microfluidic technique for liposome preparation to design and fabricate repeatable cell models with variable inner composition and tuneable size. The repeatability of mechanical measurements on created cell model will be tested using various experimental approaches. Cell mechanical standard will serve as a mean for comparing estimated mechanical properties between experimental techniques and will allow to test validity of assumptions adopted in mathematical models, for example the size effect. The experimental measurements will be coupled with the development of novel theoretical models describing cell deformations based on principles of biomembrane as two-dimensional fluid crystal wrapping cell inner environment.

6 Methods

6.1 Design of microfluidic device

All computer-aided design (CAD) models of the microfluidic devices were created using SolidWorks 3D CAD design software (Dassault Systèmes SolidWorks Corporation, Waltham, MA, USA) (Fig. 29). The models incorporated variations in channel size and interchannel angles, as detailed in Tab. 8. The selection of these angles is important for the determination of the flow rate, as they exert a direct influence on the Reynolds number [153].

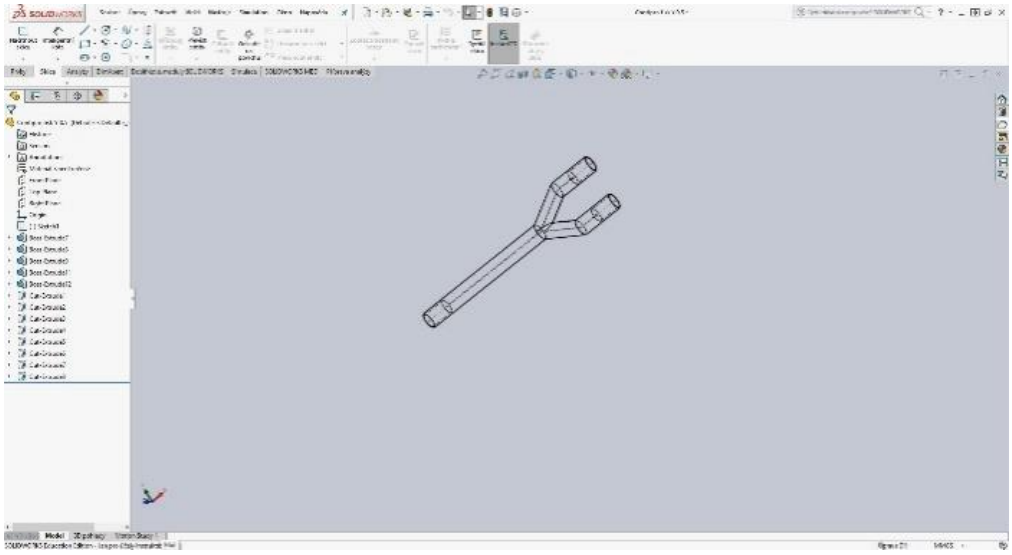

Fig. 29 CAD model of microfluidic device [153]

The first model resembled a microfluidic device made on a CNC (Computer numerical control) machine (Fig. 30). It was manufactured on a Projet® 1200 3D printer and is shown in Fig. 30. The angle range was 30° and the size of the channels: outlet channel - 0.4 mm and two input channels - 0.5 mm [153].

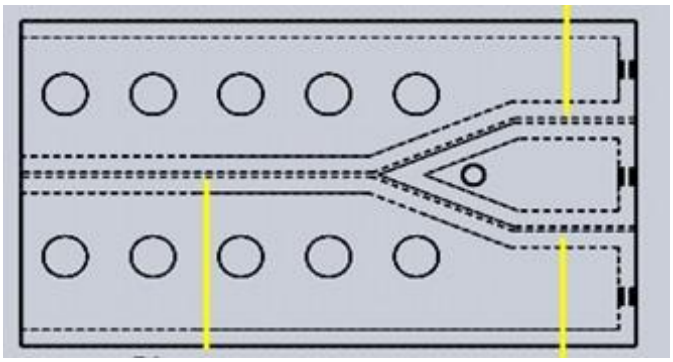

Fig. 30 CAD model of "Y" type in the block [153]

The second design sought to enhance the "T-shaped" microfluidic device, Fig. 31 by integrating additional input channels. However, this modification resulted in the accumulation of separate printed layers at the channel intersection, which in turn led to the formation of unwanted blockages. To address this issue, a variant of the "T" design was produced that lacked the blocking structure. This modification did not resolve the problem of channel clogging [153].

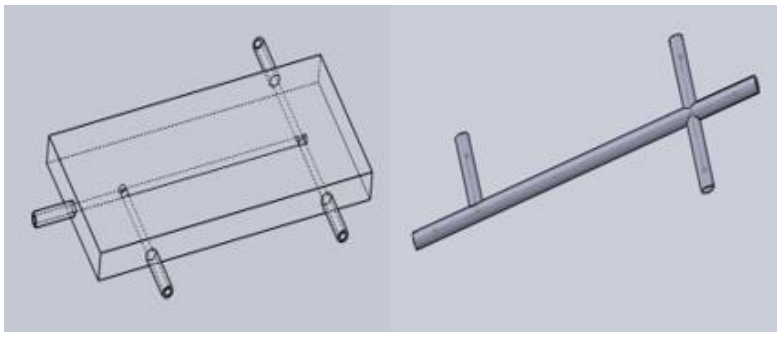

Fig. 31 (left) "T "type of microfluidic device in block (right) "T" type of microfluidic device [153]

To evaluate the accuracy of the Projet® 1200 3D printer, a set of basic microfluidic devices with varying channel widths (0.4, 0.5, 0.75, and 1.0 mm) was fabricated. The "Y-shaped" microfluidic device design Fig. 32 was chosen for this assessment due to its simplicity and the reduced requirement for support material. The aim of minimizing support material usage was to prevent potential channel blockages caused by material accumulation during printing, as observed in the previous "T" type design [153].

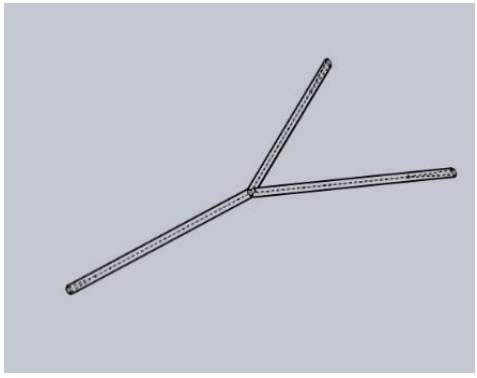

Fig. 32 Basic "Y" type of microfluidic device [153]

Liposomes serve as widely used drug delivery systems. Nevertheless, the Y-shaped microfluidic device described earlier in Fig. 32 was restricted to producing liposomes encapsulating phosphate-buffered saline (PBS) exclusively. To expand its capabilities and enable the encapsulation of a broader range of drugs, the microfluidic device design was altered to include additional inlet channels. Fig.33 (left) shows a design with three inlet channels, while Fig.33 (right) illustrates a design featuring a double cross-geometry channel [153].

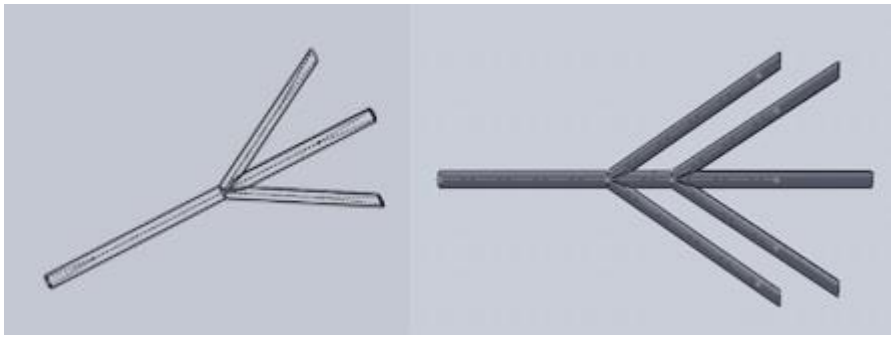

Fig.33 (left) microfluidic device with three inlet channels (right) double three inlets channels microfluidic device [153]

The selection of interchannel angles plays a critical role in determining the flow rate within the microfluidic channels. To investigate the impact of channel angle on flow rate, four microfluidic devices featuring varying interchannel angles were fabricated using PolyJet technology (Fig. 34).

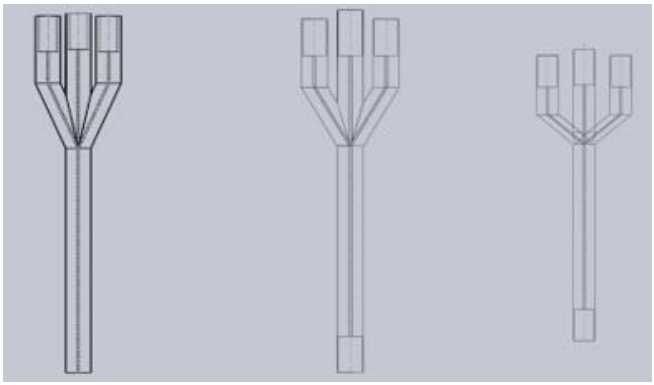

Fig. 34 A CAD model of md with 30°, 60° and 90° range of angle [153]

6.2 Development of microfluidic devices by additive manufacturing

The conventional microfluidic device fabrication methods, which are primarily reliant on soft lithography, are often complex and time-consuming. Furthermore, soft lithography is inherently constrained to the fabrication of two-dimensional channel geometries. High-precision additive manufacturing techniques offer a promising alternative to conventional microfluidic device fabrication methods, enabling the creation of intricate three-dimensional structures with variable inner channel geometries. This study proposes, evaluates, and validates the application of two additive manufacturing technologies for the development of microfluidic devices [153].

6.2.1 Additive manufacturing by Stereolithography

Microfluidic devices were fabricated using a Projet® 1200 stereolithography apparatus (SLA) based on Digital Light Processing (DLP) 3D printing technology (3D Systems, Rock Hill, SC, USA). This system utilizes a beam projector to selectively cure thin layers (30 µm) of a liquid UV-curable plastic resin (VisiJet® FTX Green, 3D Systems) onto a build platform. The fabrication process involved depositing layers of the UV-curable plastic resin (VisiJet® FTX Green, 3D Systems) until the desired 3D geometry of the microfluidic channels was achieved. After printing, any uncured resin residues were removed through a washing step using an isopropyl alcohol bath. Subsequently, the microfluidic device was dried with pressurized air and subjected to a post-curing process in a UV chamber for 10 minutes. Finally, the completed device was detached from the build platform, and any supporting structures were carefully removed by hand [153].

Tab. 5 Basic specifications of AM process using Projet® 1200

Technology	SLA, DLP
Material	VisiJet® FTX Green
Min. layer thickness	0.03 mm
Max. build size	43×27×150 mm

6.2.2 Additive manufacturing by material Jetting

An alternative method for fabricating microfluidic devices was based on the use of Stratasys PolyJet technology (Stratasys Inc., Eden Prairie, MN, USA), a form of additive manufacturing based on inkjet printing. This technique involves the deposition and UV curing of photopolymer resins in a layer-by-layer manner. In this process, a Stratasys J750 printer was employed with a printing resolution of 24 × 24 × 14 microns. The microfluidic device structure was constructed using transparent Vero Clear Model® material. To maintain the internal channel geometries throughout the printing process, a soluble support material (706 B) was employed to fill these channels. Following an initial cleaning step, the remaining support material was dissolved using a 4% sodium hydroxide and sodium silicate solution. The successful removal of the support material from the internal channels necessitated the integration of both chemical dissolution and mechanical cleaning techniques [153].

Tab. 6 Basic specifications of AM process using Stratasys 750

Technology	Polyjet
Material	Acrylate -Vero Clear®
Min. layer thickness	14 μm
Max. build size	490 × 390 × 200 mm

We have designed and manufactured several types of microfluidic devices, encompassing designs from simple geometries to those featuring intricate channel configurations. Details of these devices are provided in Tab. 7.

Tab. 7 Types of microfluidic devices

Used AM technology	Type of microfluidic device
Stereolitography	Y type in block
	T type in block
	Y type without block
	T type type without block
	Double three inlets channels microfluidic device
	Three inlets channels microfluidic device
Material Jetting (PolyJet)	Y type
	Three inlets channels microfluidic device

Tab. 8 Geometry of channels of microfluidic device

Type of manufacture	**Angle** [°]	**Size of channels Inlet / Outlet** [mm]
AM - **SLA**	30	0.4/0.5
		0.5, 0.75, 1/0.5
AM - **SLA**	60, 90	0.5/0.5
AM - **PolyJet**	30, 60, 90	0.5/0.5

6.3 Preparation of liposomes using a microfluidic device

In this study we employed a two-stage microfluidic device utilising the double emulsion drop method to generate liposomes. The microfluidic platform permitted the fabrication of two distinct liposome types, each optimised for a specific intended application. The first type of liposome encapsulated phosphate-buffered saline (PBS), while the second type incorporated hyaluronic acid (HA) [140].

6.3.1 Liposomes filled with PBS

The production of liposomes within the microfluidic device (Fig. 35) relies on the controlled mixing of two solutions introduced via syringes. One solution, phosphate buffer (PBS), is delivered through the two oblique channels, while the other solution, consisting of phospholipids dissolved in a mixture of isopropanol and chloroform (organic phase), is introduced through the central channel. The microfluidic design promotes lamellar flow, facilitating efficient solution interaction and liposome formation. The flow rates of the phosphate buffer solution (PBS) and the organic phase are maintained at 1 mL/h and 0.1 mL/h, respectively. The intersection of the channels disrupts laminar flow, initiating the formation of a mixture at the interface. This mixture reaches an equilibrium state, ultimately leading to the formation of stable liposomes [74][150].

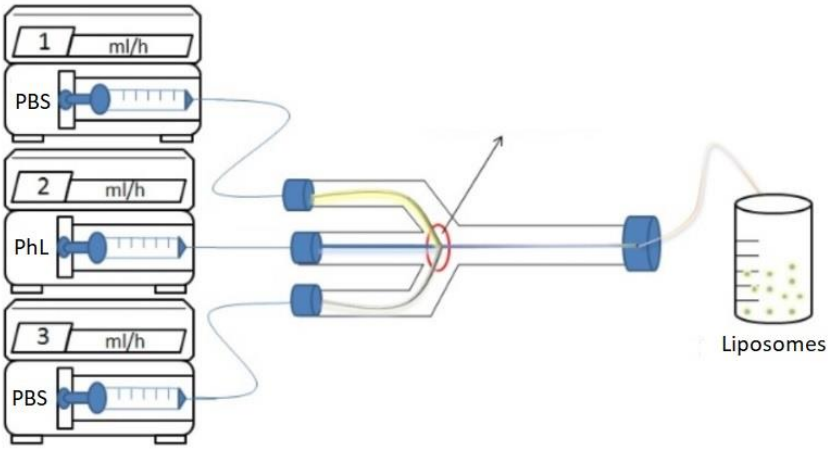

Fig. 35 Liposomes filled with PBS production

6.3.2 Liposomes filled with HA

Hyaluronic acid (HA)-loaded liposomes were produced using a custom designed double three inlets channels microfluidic device, Fig. 36. The production process mirrors that of conventional liposomes, with key modifications to the inlet channels. HA solution is introduced through the central channel, while dissolved phospholipids in a solvent mixture (organic phase) are delivered via the first pair of opposing oblique channels intersecting the central one. The second pair of opposing oblique channels is used to feed phosphate-buffered saline (PBS). This configuration facilitates the co-localisation of HA and phospholipids at the channel intersections, which enables their encapsulation within the forming liposomes. As in conventional liposome production within microfluidic devices, the formation process is governed by the diffusion of various molecules (primarily organic solvents, PBS, and lipids) at the interfaces between the solvent and non-solvent (PBS) phases [74][140].

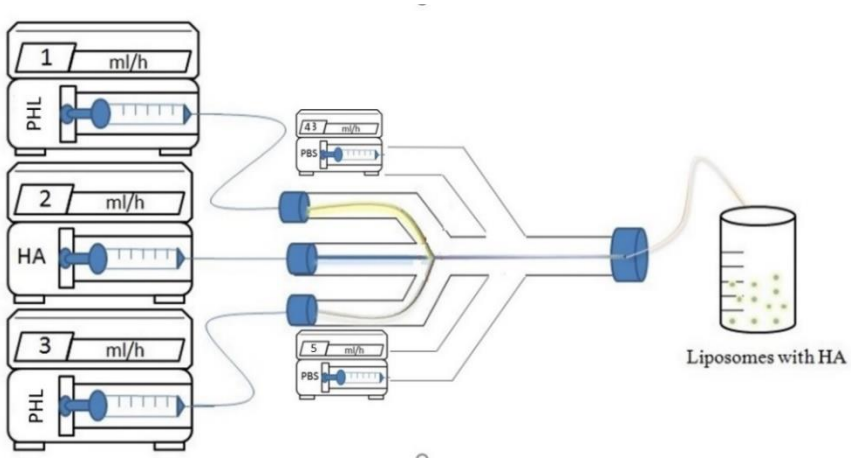

Fig. 36 Liposomes filled with HA production[140]

6.4 Liposome fixation

The binding required to measure the mechanical properties of liposomes was achieved using an avidin-biotin complex. Biotin-DOPE and DPPC lipids were used at a concentration of 1: 1000. The biotinylated surface was then incubated with avidin (0.30 mg/ml) and washed three times with PBS buffer. Finally, 1 ml of the liposomal formulation and approximately 1 ml of PBS buffer were applied to a Petri dish and incubated for 5 min at room temperature [75][141][143].

6.4.1 Chemicals

Tab. 9 Chemicals used in liposome production

DPPC	Phospholipids 11145 (Sigma-Aldrich, s.r.o.)
DOPC	Phospholipids 850375P (Sigma-Aldrich, s.r.o)
PBS	Phosphate buffered saline, pH7 (Sigma-Aldrich, s.r.o)
HA	hyaluronic acid (Sodium Hyaluronate, Tech. Grade, molecular weight 2000–2200 kDa, Contipro a.s.)
Biotin	18:1-12:0 Biotin PE (Sigma-Aldrich, s.r.o.)
Ethanol	Ethyl alcohol, EtOH (Sigma-Aldrich, s.r.o.)
Isopropanol	≥99.7%, FCC, FG (Sigma-Aldrich, s.r.o.)
Chloroform	≥99.9%, (Sigma-Aldrich, s.r.o.)

6.5 Mechanical testing of liposomes

The mechanical properties of the liposomes were evaluated utilising three distinct instruments: a NanoWizard® 3 NanoOptics Atomic Force Microscope (AFM) system (JPK Instruments, Germany), a Hysitron TI 950 TriboIndenter® nanomechanical tester (Bruker Corporation, USA), and a Bruker Hysitron BioSoft® instrument (Bruker Corporation, USA).

6.5.1 Atomic force microscopy

The experiment was performed in the Laboratory of Nanotechnology at the Faculty of Biomedical Engineering, CTU, in Kladno with NanoWizard® Sense AFM System (JPK, DE). AFM system is combined with a confocal fluorescence microscope. A colloidal probe with a diameter of 5.2 µm (APPnano, CA, USA) is located at the end of the beam (spring rigidity constant of 0.0307 N/m) which deforms during indentation [141].

A Petri dish containing liposomes filled with PBS was initially placed in the instrument. Subsequently, one liposome was located using an optical microscope and its position was recorded. The optical microscope image of the liposomes is shown in Fig. 37.

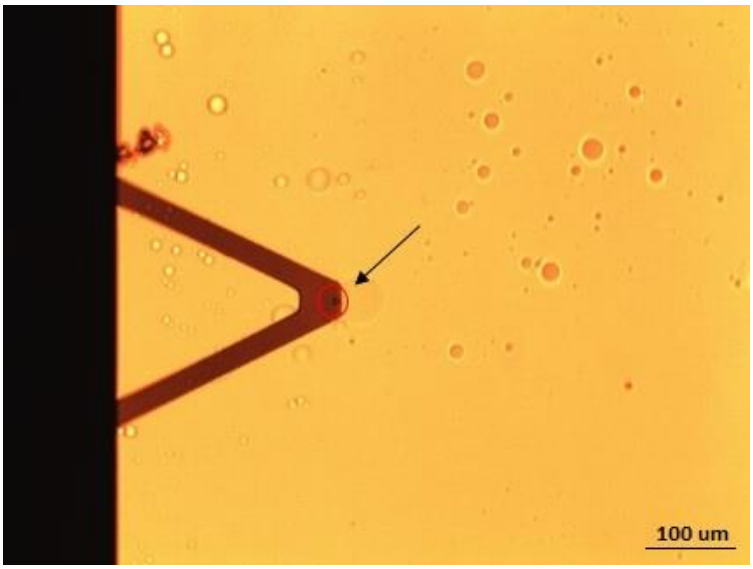

Fig. 37 AFM tip with measured liposome [148]

The cantilever was calibrated using the recommended standard procedure provided by the manufacturer. Initial sensitivity of the cantilever was established via indentation measurements conducted on the glass, followed by determination of cantilever stiffness using thermal noise. The beam's deformation was measured by a laser on the principle of optical lever. The force employed was determined through multiplication of the beam's stiffness by its deflection.

Force spectroscopy of the liposomes was performed with a z length of 15 μm, a relative set point of 20 nN, and the loading rate was 3.75 μm/s. The following inclusion criteria are applied: the isolated spherical shape of the liposome without collapse [76] or extensive adhesion to the surface [77], and at least two successful measurements in each liposome. Force-deformation curves were measured in the center of the liposome.

A schematic illustration of the AFM measurement principle is shown in the Tab. 10 below.

Tab. 10 a-e principle of AFM measurement [78]

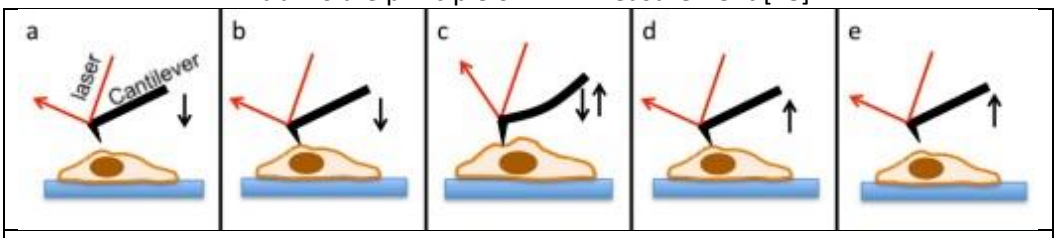
a) AFM cantilever approaches the liposome from few microns above
b) Cantilever with AFM probe contacts the liposome
c) Indents the liposome
d) The cantilever deflection reaches a pre-selected set point
e) Moves away from the liposome

6.5.2 Microcompresion testing using instrumented nanoindentation

The experiment was carried out in the Nanoindentation Laboratory at the Faculty of Mechanical Engineering CTU. A Hysitron TI950 TriboIndenter® (Bruker Corp.) A diamond conospherical tip with flat end of diameter 100 µm (Bruker Corp.) was used for compression testing of whole liposomes. The liposome was localized using a light microscope which is mounted in the nanoindentation instrument, as shown in Fig. 38. Force controlled experiment with maximum indetation force 3000 µN in 15 second (200 µN/s) was performed [148][151][154].

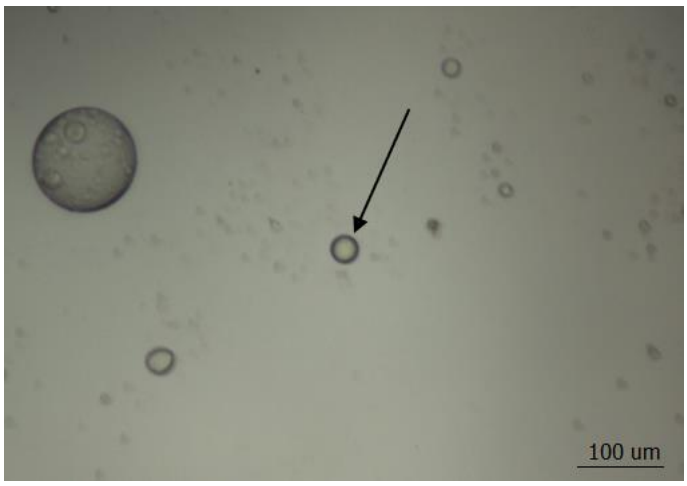

Fig. 38 Liposomes localized using a light microscope

6.5.3 Microcompression testing using miroindenter with extended movement of the tip

Bruker's Hysitron BioSoft In-Situ Indenter was used for compression testing of liposomes. with a diamond conospherical tip with flat end with diameter 50 µm (Bruker Corp.). Displacement controlled experiment with prescribed maximum movement of the tip 100 µm in 10 second was carried out to obtain mechanical properties of whole liposome. Screenshot of the microcompression testing of liposomes is shown in Fig. 39.

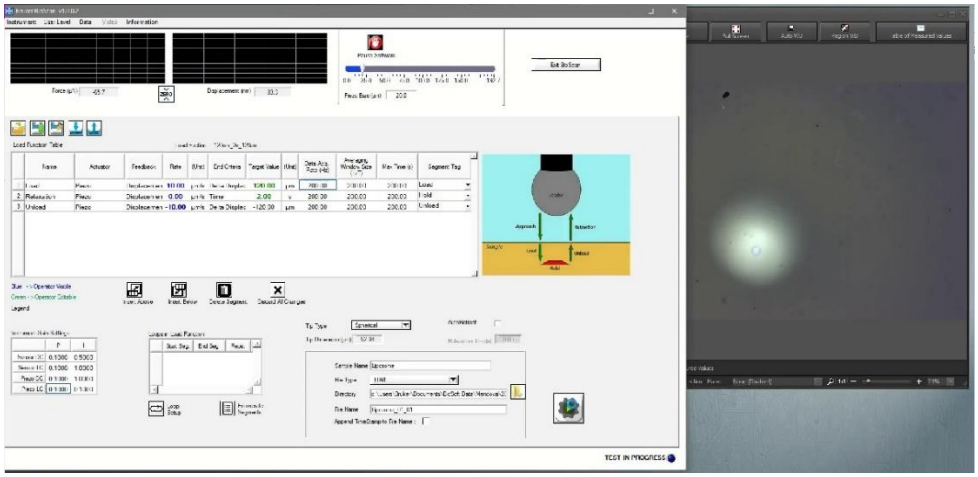

Fig. 39 Screenshot of the microcompression testing of liposomes on Bruker's corp. indenter

Subsequently, an inverted light microscope was employed to identify a single liposome, with its position being recorded. The image of the liposome captured using the optical microscope is presented in Fig. 40.

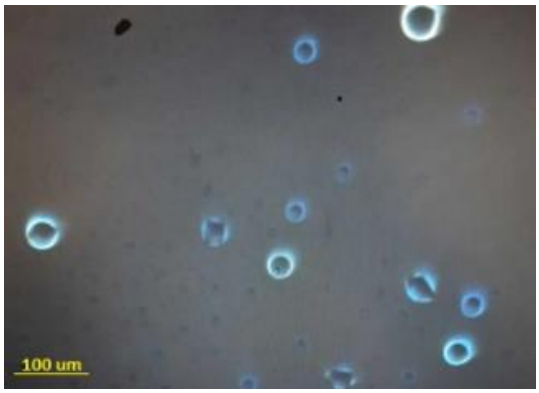

Fig. 40 Liposomes observed using an inverted light microscope

6.6 Data processing

The initial step involved the determination of the dimensions of the measured liposomes using the ImageJ software. The mechanical testing generates force-displacement curves, which illustrates the relationship between the applied force and the resulting tip displacement. Prior to the application of suitable analytical models, it is essential to perform data pre-processing steps. Firstly, any hydrostatic force acting on the tip must be subtracted from the measured force values. Secondly, the contact point, which corresponds to the beginning of the actual indentation on the liposome, must be identified.

6.6.1 Image processing

The reference value for determining the size of liposomes within a specific testing method is established based on the diameter of the AFM tip utilized. In this study, the liposomes exhibited a diameter range of 5 to 80 µm. The dimensions of the liposomes were analysed using the image processing software ImageJ (developed by Wayne Rasband, National Institutes of Health [NIH]), (Fig. 41) [140].

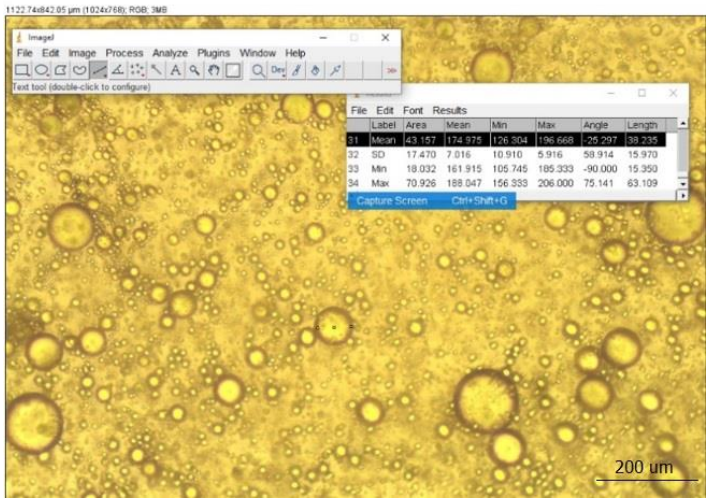

Fig. 41 Measurement of liposome size using ImageJ software

6.6.2 Contact point definition

A critical challenge in employing suitable analytical models to evaluate the mechanical properties of liposomes using Atomic Force Microscopy (AFM) is the precise determination of the measurement origin. JPK DP software (version spm-5.0.145), a common tool for calculating Young's modulus in AFM measurements, relies on manual definition of the contact point to initiate the measurement. This approach introduces subjectivity and potential inaccuracies. To address this limitation, the initial data processing steps involve the removal of baseline tilts and offsets from the force-displacement curve. Subsequently, the "find contact point" and "subtract baseline" functions are employed to identify the precise point of initial contact between the AFM tip and the liposome (Fig. 42) [79].

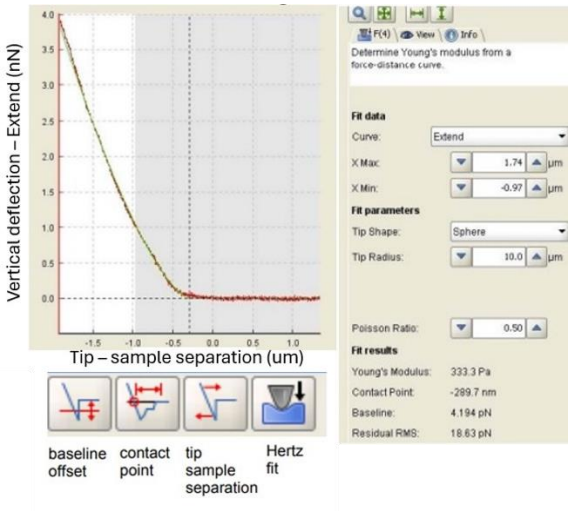

Fig. 42 Screenshot of JPK software used to determine the Young´s modulus [79]

In case of microcompression testing by microindenter the origin curves are filtered (hydrostatic force subtraction) in the TriboIQ software before analysis. The contact point is determined semi-automatically. The recorded indentation curve is shown in Fig. 43.

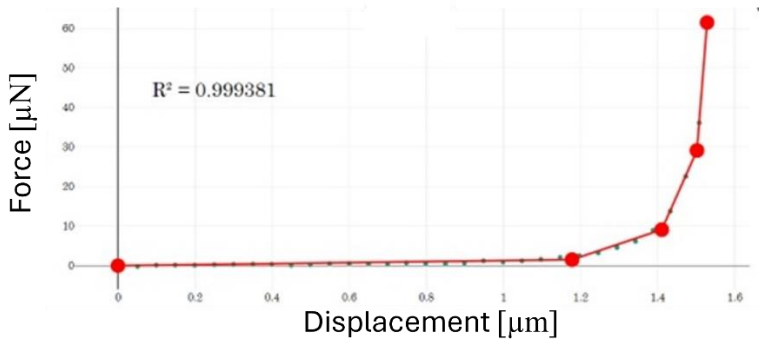

Fig. 43 Recorded indentation curve

Given the inherent limitations of manual and semi-automatic methods for determining the measurement start point, an automated model has been developed with the objective of achieving more precise contact point detection. The model identifies the contact point as the data point on the loading curve where a predefined mathematical function provides the optimal fit. In comparison to previous methods, this approach includes an additional step that considers the influence of hydrostatic pressure on the approach curve.

The model employs a two-step fitting process for each data point on the force curve. Firstly, a linear fit is applied to the data points preceding the point of interest. Secondly, a deformation model is

applied to the data points following the point of interest, utilising the selected point as the initial contact point. The relative root-mean-square error (RMS) of both fits is calculated, and the sum of these errors is determined for each data point. Finally, the data point corresponding to the minimum total fitting error is selected as the automated contact point.

6.7 Data analysis – mathematical models

The mechanics of the cytoskeleton is a field that relies heavily on mathematical models for the interpretation of experimental data related to forces and deformations. As a model system for the study of biological membranes, we present two types of novel mathematical models specifically designed to analyse the mechanical properties of liposomes. Our models consider various factors such as stretching, bending and contact adhesion during atomic force microscopy (AFM) indentation using a spherical tip and compression testing using a flattened diamond cone tip [139][144].

6.7.1 Linear material model

Force-displacement curves obtained by AFM measurement of liposomes were fitted with a straight line. The stiffness of the liposome was determined using this equation:

$$F = kx \tag{20}$$

Where F is force, k is a spring constant and x is displacement.

6.7.2 Hertz model

The selection of the most appropriate Hertz model equation is dependent upon the specific geometry of the atomic force microscope (AFM) tip employed during the measurements. In this study, a spherical tip was employed. Consequently, the Young's modulus (E) was determined using the Hertz model for a spherical indenter, where R represents the radius of the tip [141].

$$F = \frac{4}{3}E^{*}\sqrt{R}d^{\frac{3}{2}} \tag{9}$$

6.7.3 Modified Overbeck model

The mechanical properties (Young´s modulus) of liposomes measured by Bruker's Hysitron BioSoft in-situ indenter is determined by a model based on the geometric model as used by Overbeck et al. [80] but modified for a different geometry of the measured liposomes [55]. The selection of this model is motivated by its ability to account for the specific geometry of the liposome. Within this model, it is proposed that the liposome undergoes a deformation process, transitioning from a sphere shape to a fully circular toroidal shape, while maintaining a constant volume [81].

$$V_{E0} = V_{T0} \tag{21}$$

where V_{E0} is the volume of the sphere and V_{T0} is the volume of the full toroid [81]:

$$V_{E0} = \frac{4}{3}\pi {R_0}^3 \tag{22}$$

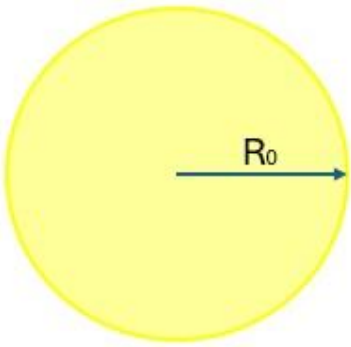

Fig. 44 The shape of the liposome in the form of sphere

where, R_0 is the radius of the liposome [81].

The initial volume of the full toroid V_{T0} is calculated as [81]:

$$V_{T0} = \frac{\pi}{4} {a_0}^2 h_0 + A_{sc0} 2\,\pi r_{C0} \qquad (23)$$

Where a_0 is the diameter of the cylinder inside the solid toroid, h_0 is the height of the solid toroid, Asc_0 is the area of the semicircular cross-section of the solid toroid before compression is shown in Fig. 45 and is calculated [81]:

$$Asc_0 = \frac{\pi \frac{{h_0}^2}{4}}{2} \qquad (24)$$

and r_{c0} is the central radius [81]:

$$r_{c0} = \frac{a_0}{2} + \frac{2h_0}{3\pi} \qquad (25)$$

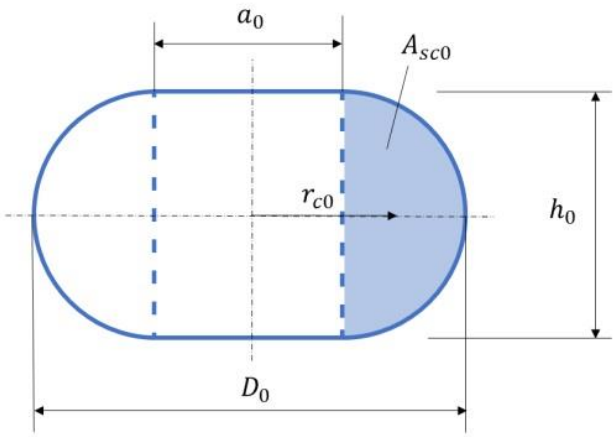

Fig. 45 A cross section of a solid toroid with the initial dimensions defining the initial shape of the cell prior to compression testing [81]

Finally, we express the single unknown a_0 from the equation (21). The instantaneous dimension a, i.e., the diameter of the inner cylinder of the full toroid during compression Fig. 46 is expressed as [81]:

$$V_{T0} = V_T \qquad (26)$$

where V_T represents the volume of the solid toroid cell during compression. The assumption is also the same as that of Overbeck et al i.e., the Laplace equation [80]. The internal pressure in a thin-walled solid toroidal vessel can be expressed as [81]:

$$p = \sigma_w \frac{(\pi th + 2at)}{ah + \pi \frac{h^2}{4}} \qquad (27)$$

where t is the wall thickness, σ_w is the wall stress, h is the instantaneous cell height and a is the instantaneous diameter of the circular area that is in contact with the indenter (Fig. 46) [81].

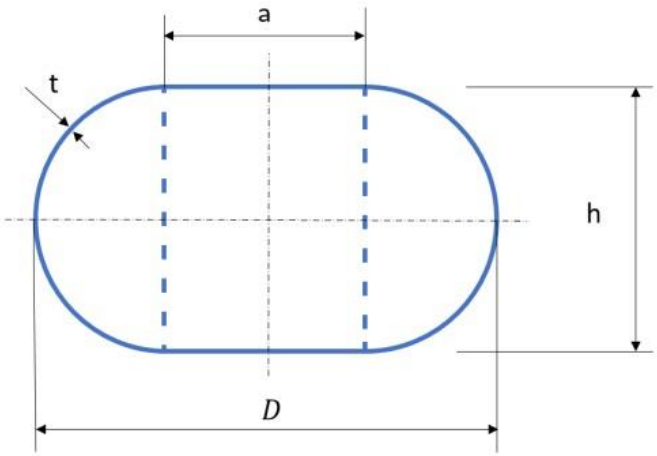

Fig. 46 A full toroidal compressed liposome. The full toroid is considered here as a thin-walled shell with characteristic dimensions marked [81]

The expression for the internal pressure is obtained from the equilibrium equation in the equatorial section by means of a full toroid, see Fig. 47 [81].

$$p\,(ah + \pi \frac{h^2}{4}) = \sigma\,(\pi th + 2at) \qquad (28)$$

The left side of the equation represents the force acting in the wall of the vessel, while the right side represents the force due to the pressure inside the vessel acting on the bottom of the vessel. Furthermore, the linear elastic behaviour described as $\sigma = E\varepsilon$ is assumed. The diameter of the liposome before deformation D_0 in the equatorial plane, see Fig. 45, is expressed by equation (29) and the instantaneous cell diameter D in the equatorial plane during deformation, see Fig. 46, by equation (30) [81].

$$D_0 = h_0 + a_0 \qquad (29)$$

$$D = h + a \qquad (30)$$

$$h = h_0 - d \quad (31)$$

The force with which a cell responds to deformation can be calculated as [81]:

$$F = \frac{\pi}{4} a^2 p \quad (32)$$

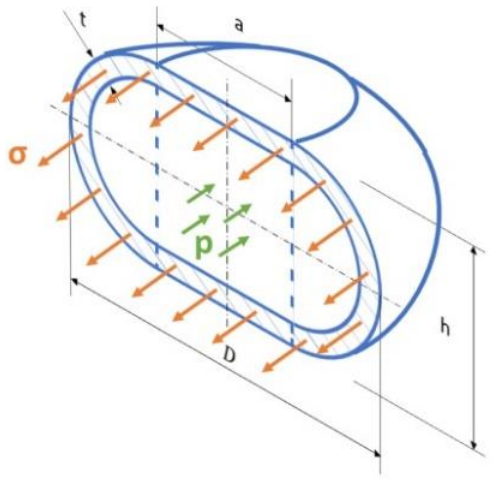

Fig. 47 Quatorial section through a thin-walled vessel in the form of a solid toroid representing a liposome. The stress in the wall of the vessel and the pressure p in the cell are given [81]

From all the previous equations, a single equation expressing the dependence of the force F on the tip displacement d, the known geometric parameters of the cell a_0, h_0, t and the unknown material parameter E. Mathematically expressed: $F = F\ (d, a_0, h_0, t, E)$ [81].

6.7.4 Prescribed shape model

In the proposed model, the liposome is divided into two segments: the fluid membrane shell and the inner compound. The inner compound of the membrane is assumed to consist of an incompressible fluid characterised by an internal pressure denoted by p. The main assumption of the model is that liposomes undergo fully reversible adiabatic deformation, like a spring. Energy conservation implies that the external force required to deform a liposome induces deformation energy within the liposome itself. Being incompressible, the inner fluid of the liposome experiences no significant change in volume under compression or expansion and therefore cannot store energy in the form of elastic potential energy. However, the liposome membrane shell is deformable and can store strain energy. The amphiphilic nature of the lipid membrane imparts fluidity in the plane of the membrane and resistance to mechanical stress [82]. Particularly strain and bending. The stretching energy (U_S) can be expressed as follows [83][139]:

$$U_{s=\frac{1}{2}\int K_A \Theta^2 d_A} \quad (33)$$

Here, K_A represents the area compressibility modulus [83], and Θ denotes the relative change in the segment dA induced by loading. Assuming membrane fluidity conditions equilibrium in Θ across the surface of the liposome [84], neglecting shear stresses, Eq. (33) can be simplified as follows [85][139]:

$$U_{s=}\frac{1}{2}K_A(\frac{\Delta A}{A})^2 A \quad (34)$$

Another contribution to the deformation energy of the membrane arises from bending. Bending energy represents the energy required to curve a membrane. A biological membrane, as a two-dimensional surface spanning a three-dimensional space, can be characterized by two principal curvatures, C_1 and C_2. The energy of biomembrane bending can be expressed using the Helfrich-Canham functional [86][139]:

$$U_B = \frac{1}{2}\int K_B\,(C_1 + C_2 - C_0)^2 d_A \quad (35)$$

In this equation, K_B represents the bending modulus, and C_0 denotes the intrinsic curvature [87]. Contact energy refers to the excess free energy due to the existence of an interface, arising from imbalanced molecular forces [88]. It can be expressed as an energy per unit area, known as the specific surface energy γ. Contact adhesion energy (U_c) can be expressed as follows [139]:

$$U_c = \gamma A_c \quad (36)$$

Here, A_c represents the contact area.

If the shape of the liposome is known, we can determine the total deformation energy [139]:

$$U_{def} = U_S + U_B + U_C \quad (37)$$

To obtain a simple approach for calculating the total elastic deformation energy, we assume that the shape of the liposome membrane possesses azimuthal symmetry. Furthermore, we assume that the membrane is deformed by a spherical indenter of radius R_0. After deformation, the membrane has a torus-like shape with the maximum deflection in the axis of symmetry. The bilayer profile is represented by three circular arcs and a line segment representing contact with the surface (Fig. 48) [139].

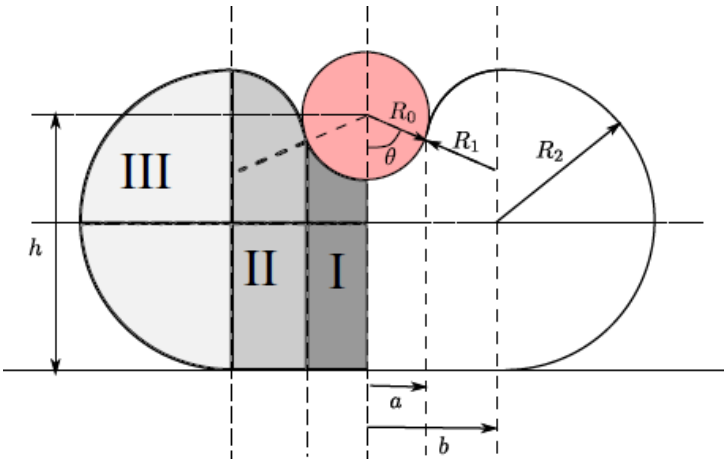

Fig. 48 Geometry of spherical AFM tip and membrane interaction [139]

The tip interacts with a liposome attached to the surface. The problem is axisymmetrical and individual segment of the cell membrane are described as elements of circle. The curve describing the outline of the sphere is smooth. The membrane could be divided into four segments that define four separate volumes [139].

Tab. 11 Segments of model

Segments of AFM tip and membrane interaction	**Description of the segment**	
Segment I	Liposome attached to AFM tip	radius equals to the radius of AFM tip, size given by angle θ
Segment II	Radius R_1	Given by angle θ
Segment III	Donut shape segment	Radius R_2
Segment IV	Liposome attached to the surface	Circle with radius b

Segment I

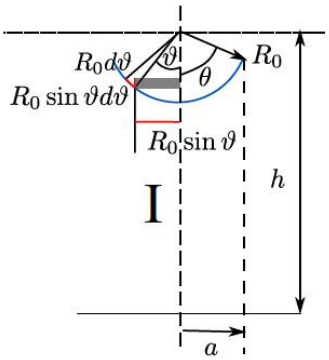

Fig. 49 Segment I

The first segment (Fig. 49) is in contact with the spherical indenter, and its radius equals R_0. The size of the segment is given by the radius distance a, defined as follows [139]:

$$a = R_0 sin\theta \qquad (38)$$

The principal curvatures of the first segment, C_1^I and C_2^I, are both equal to $1/R_0$. The curvature of the second arc is denoted as R_1. Assuming the membrane shape is smooth, the radius R_1 can be defined using the angle ϑ as follows [139]:

$$R_1 sin\theta + a = b \qquad (39)$$

Here, b represents the radial size of the fourth segment. The first principal curvature of the second segment C_1^{II} is R_1, while the second principal curvature is given by [139]:

Segment II

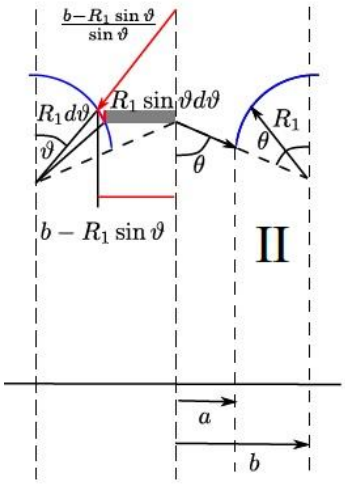

Fig. 50 Segment II, shaded element is a volume element

$$C_2^{II} = -\frac{sin_\vartheta}{b - R_1 sin_\vartheta} \quad (40)$$

Here, θ ranges from 0 to ϑ. The negative sign indicates that the membrane bends outward in the second segment (Fig. 50). The third arc segment Fig. 51 corresponds to the outer toroid shell and has a first principal curvature equal to [139]:

Segment III

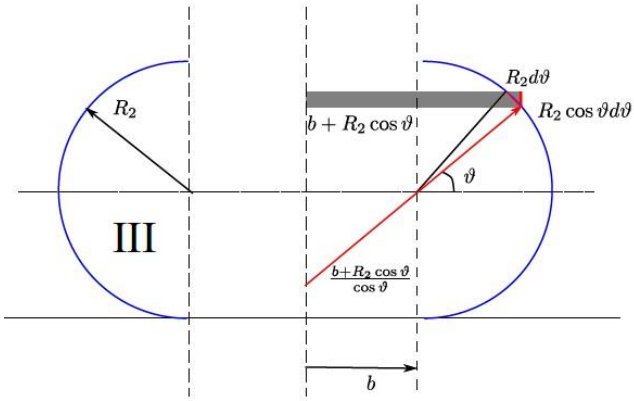

Fig. 51 Segment III, shaded element is a volume element

$$C_1^{III} = \frac{2}{h - (R_{0-}R_1)sin\theta} \quad (41)$$

$$C_2^{III} = \frac{cos_\vartheta}{b + R_2\, cos_\vartheta} \quad (42)$$

Here, ϑ lies in the interval [$-\pi/2$, $\pi/2$] [139].

Segment IV

The last segment has the shape of a spherical disc with diameter b, representing the contact of the liposome with the substrate. Both principal radii of curvature, C_1^{IV} and C_2^{IV}, are equal to zero.

The area and volume of individual segments can be expressed using surface and volume integration formulas known for solids of revolution [89]. The shape of the liposome is described by three parameters: a, b, and h. The liposome deformation is representing, while a and b describe the contact area with the indenter tip and substrate, respectively. The deformation energy corresponding to a given set of parameters can be expressed using Eq. (37).

In an experimental setup, the displacement of the spherical tip δ is measured. The force F required to induce deformation can be computed using Castigliano's first theorem [90][139].

$$F = \frac{\partial U_{def}}{\partial \delta} \qquad (43)$$

6.7.5 Fluid shell model

The model described below is restricted to shapes with rotational symmetry. Their principal curvatures are those along the meridians (c_m) and the parallels of latitude (c_p). Let the contour of a cell be given by a function $z(x)$, the z-axis being the rotational axis. By ψ we denote the angle made by the rotational axis and the surface normal of the cell surface (Fig. 52). With this notation we find [144]:

$$c_m = \frac{\sin\psi}{x} \qquad (44)$$

$$c_p = \cos\psi \frac{d\psi}{dx} \qquad (45)$$

$$-\tan\psi = \frac{dz}{dx} \qquad (46)$$

We further assume that there is an isotropic tension γ in the membrane which uniform throughout the membrane and the hydrostatic pressure difference Δp is constant. We can further assume that phospholipid bilayer behaves as liquid crystal with hydrostatic tension in the plane of the membrane. From Laplace-Young equation follows [144]:

$$\Delta p = \gamma\left(c_m + c_p\right) \qquad (47)$$

Therefore, the mean curvature over the surface must be constant [144].

$$\left(c_m + c_p\right) = const \qquad (48)$$

We rather express it using original formulation [144]:

$$\frac{\sin\psi}{x} + \cos\psi \frac{d\psi}{dx} = C \qquad (49)$$

By using substitution $u = sin\ \psi$ we may express [144]:

$$\frac{u}{x} + \frac{du}{dx} = C \qquad (50)$$

where C is a constant. To solve the differential equation, the membrane must be divided into two segments in $z=z_0$ plane. The z_0 is taken at maximum diameter $x=c$ of the cell [144].

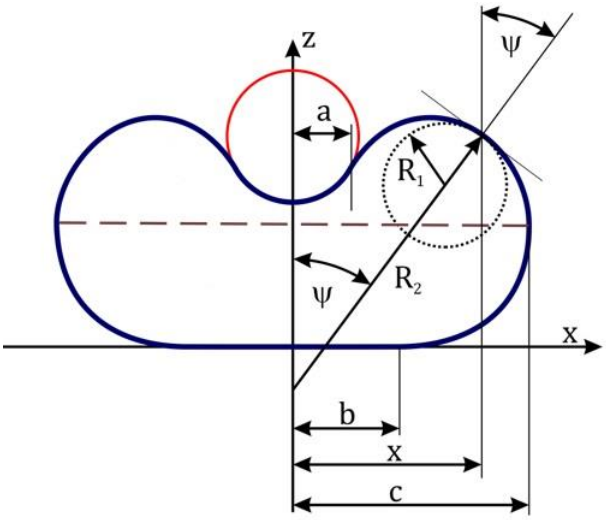

Fig. 52 Schema of the fluid shell model during indentation [144]

The solution of the differential equations can be obtained by separation of constants as [144]:

$$u = Ax + B/x \qquad (51)$$

If membrane tension is constant in the whole free membrane, it follows from Laplace equation (47) that [144]:

$$\frac{u_1(c)}{c} + \frac{du_1(c)}{dx} = \frac{u_2(c)}{c} + \frac{du_2(c)}{dx} \qquad (52)$$

Considering solution of the differential equation, we may express [144].

$$2H = \frac{u}{x} + \frac{du}{dx} = A + Bx^2 + A - Bx^2 = 2A \qquad (53)$$

and it means that a mean curvature is not a function of B. However, it should hold that at $x = c$, $\psi = \pi/2$, i.e., $\sin\psi = 1$ [144].

$$Ac + B_1/c = 1 = Ac + B_2/c \qquad (54)$$

and therefore $B_1 = B_2 = B$. From boundary conditions we obtain [144]:

$$-\sin\theta = Aa + B/a \qquad (55)$$

$$0 = Ab + B/b \qquad (56)$$

$$A = -\frac{a\sin\theta}{a^2 - b^2}, B = \frac{ab^2\sin\theta}{a^2 - b^2} \quad (57)$$

The general shape equation sounds [144]:

$$\sin\psi = -\frac{a^2}{(a^2 - b^2)}\frac{x}{R_0} + \frac{a^2b^2}{(a^2 - b^2)}\frac{1}{R_0 x} \quad (58)$$

The equation above is valid for segment I, $xI \in [a, c]$, where c is defined as the point, where $\psi = \pi/2$. Symmetrical solution is valid for segment II (Fig. 52) [144].

The energy of stretching (U_S) could be expressed as [144]:

$$U_S = \int \frac{1}{2}\kappa_A \Theta^2 dA \quad (59)$$

where K_A is the area compressibility modulus and Θ is the relative change in segment dA induced by loading. Membrane fluidity conditions equilibrium in Θ over the surface of liposome if the shear stresses are neglected. The total area of the membrane consists of free membrane, membrane in contact with AFM tip, and the flat membrane in contact with surface. Therefore, Eq. (59) can be simplified into [144]:

$$U_S = \frac{1}{2}\kappa_A \left(\frac{\Delta A}{A}\right)^2 A \quad (60)$$

In experimental setup, the displacement of spherical tip δ is measured. The force required to induce deformation Q can be computed using the Castigliano's first theorem [144].

$$Q = \frac{\partial U_{def}}{\partial \delta} \quad (61)$$

6.8 Statistical analysis

Statistical analyses were performed with the R software (version 4.1.2, R Core Team, 2021). A p-value less than 0.05 was considered statistically significant. The normality of the data was tested using the Shapiro-Wilk test. The differences in materials properties between different liposome types or treatments were analyzed using one-way analysis of variance (ANOVA) followed by Tukey's post hoc test for normally distributed data and by Kruskal-Wallis test otherwise. Difference between the groups was estimated using t-test for normally distributed data and by Wilcoxon rank sum test otherwise. The linear correlation variables were assessed using linear regression (package lme4) considering repeated measurements and characterized by Pearson correlation coefficient [91].

Itra-class correlations (ICC) and repeatabilities (R) were computed to quantify the reproducibility of measurements and for understanding the structure of experimental variation by parametric bootstrapping and while the significance testing was implemented by likelihood ratio tests and through permutation of residuals implementd in package rptR, version 0.9.22. F-test was utilized to compare variances in materials parameters.

7 Results

7.1 Additive manufacturing of microfluidic device

The production of liposomes utilized a microfluidic device that was specifically designed to mimic the basic cellular structures. This device was fabricated using additive manufacturing techniques, specifically stereolithography and PolyJet technology [152].Following a thorough evaluation of both 3D printing methods, stereolithography was chosen due to its superior ability to generate smoother surface features, which are critical for optimal microfluidic device performance. Fig. 53 presents the final 3D-printed microfluidic devices employed for liposome production [152].

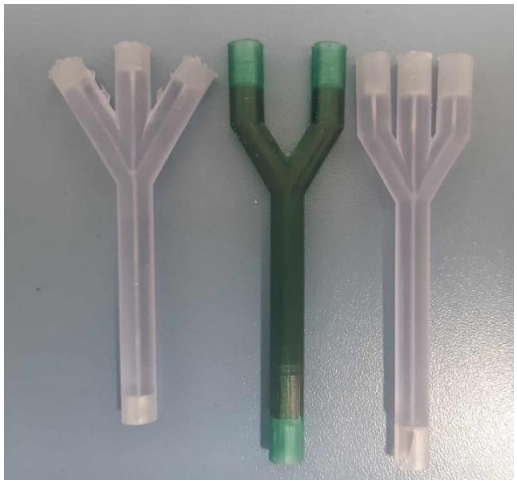

Fig. 53 The final 3D printed microfluidic devices

Tab. 12 Microfluidic devices used to prepare liposomes [152]

Type of manufacture	**Type of microfluidic device**	**Angle** [°]	**Size of channels Input / Outlet** [mm]	**Used microfluidic device**	**Why?**
AM - **SLA**	Y type in block	30	0.4/0.5	X	clogged channels - liposomes not formed
AM - **SLA**	T type in block	90	0.4/0.5	X	clogged channels - liposomes not formed
AM - **SLA**	T type without block	90	0.5/0.5	X	clogged channels - liposomes not formed

AM - **SLA**	Y type without block	30	0.4 /0.5	✓	used in the beginning, the bigger angle was better for formation of liposomes
			0.75/0.5	X	too large channels - liposomes not formed
			1/0.5	X	too large channels – liposomes not formed
AM - **SLA**	Y type without block	60	0.5/0.5	✓	were used
AM - **SLA**	Three inlets channels microfluidic device	60	0.5/0.5	✓	
	Double three inlets channels microfluidic device		0.5/0.5	✓	
AM - **PolyJet**	Three inlets channels microfluidic device	60	0.5/0.5	✓	were used, but SLA technology is better - smoother surface
	Double three inlets channels microfluidic device	60	0.5/0.5	✓	
AM - **SLA**	Three inlets channels microfluidic device	90	0.5/0.5	X	Liposomes not formed

7.2 Liposomes prepared by microfluidic device

This study employed a microfluidic device comprising three inlet channels to generate liposomes encapsulating phosphate-buffered saline (PBS). The flow rate within these channels is of critical importance in determining the final size of the liposomes. Higher flow velocities facilitate the formation of larger liposomes, whereas lower velocities result in smaller ones. The range of liposome diameters achieved spanned from 5 to 80 µm. Fig. 54 presents representative examples of liposomes filled with PBS [140].

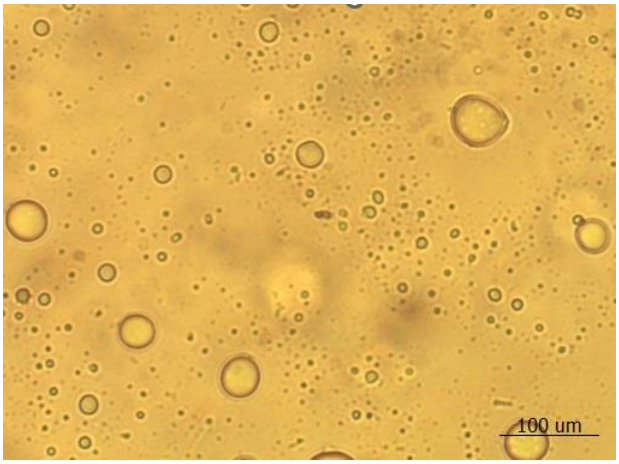

Fig. 54 Liposomes filled with PBS

Liposomes filled with hyaluronic acid (HA) were produced using a microfluidic device with a double-cross channel geometry, Fig. 55 [140].

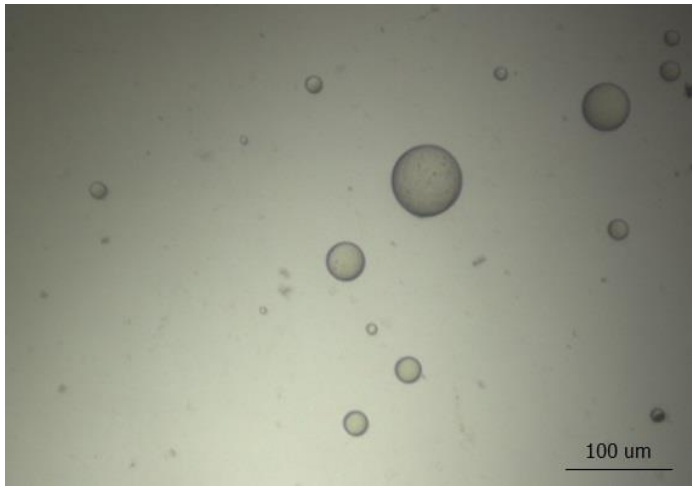

Fig. 55 Liposomes filled with HA

7.3 Prescribed shape model

The predicted shape of liposomes based on the developed mathematical model is visualized in Fig. 56 and Fig. 57. As the displacement of the spherical indenter increases, the deformation of the liposomes also increases. At larger deformations, the liposomes become more bulged, resulting in increased contact with both the indenter and the substrate. For displacements lower than 2 µm, the entire liposome deforms uniformly, while at higher displacements, the indenter significantly recesses into the liposome [139].

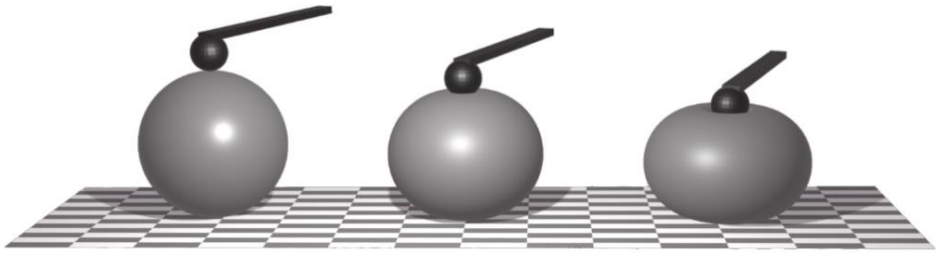

Fig. 56 Shape of liposome during mechanical testing. the displacement of the spherical indenter increases from left to right (0 µm on the left, 7.5 µm in the middle, and 15 µm on the right). The AFM spherical indenter and cantilever are schematically represented in black [139]

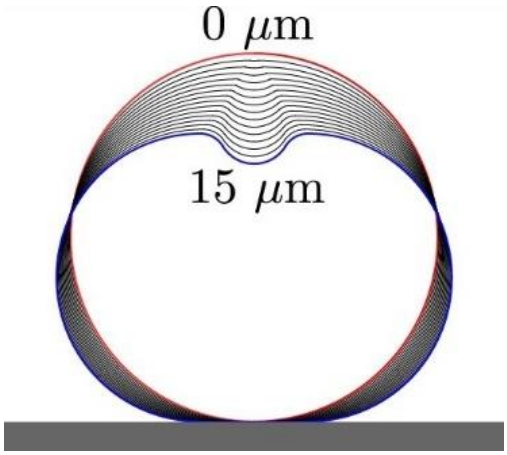

Fig. 57 Contours of liposomal shape during mechanical testing. each contour corresponds to a 1 µm increment in displacement, ranging from 0 to 15 µm [139]

Larger deformations generally correspond to higher energy levels in the liposomes. The stretching mode of the biomembrane.

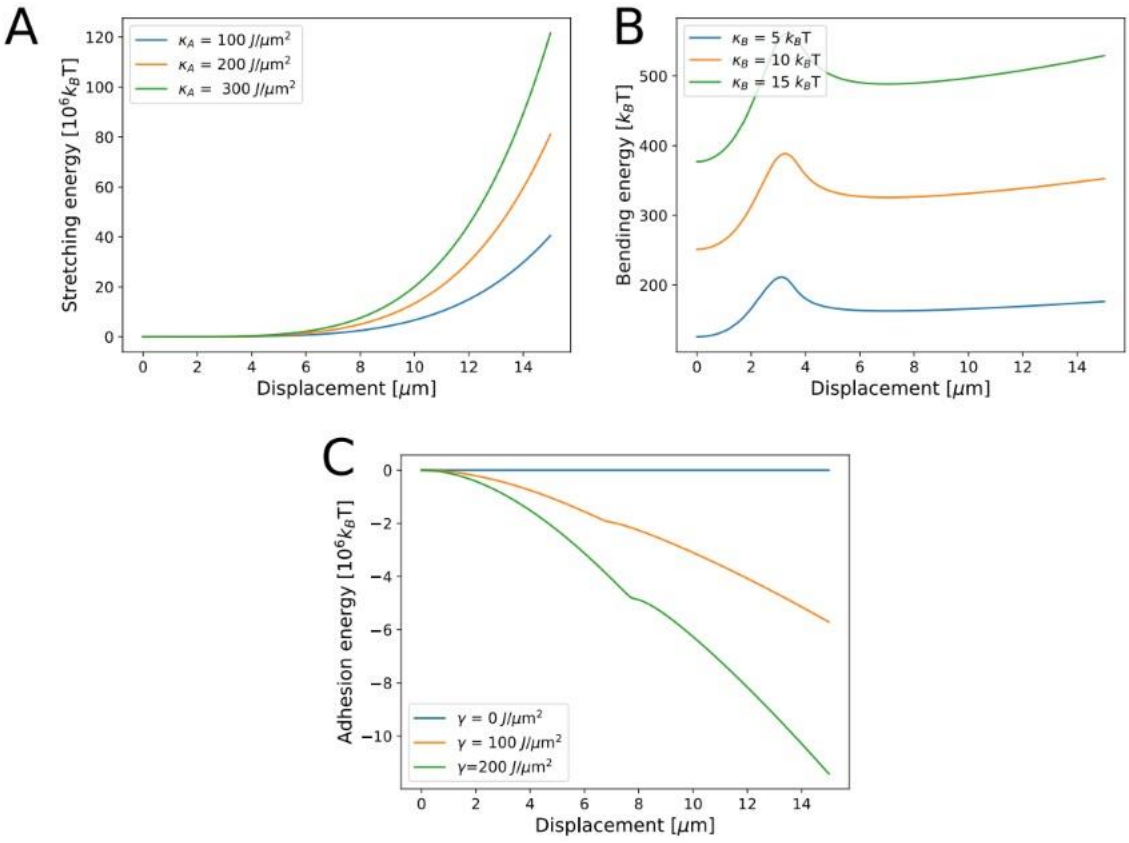

Fig. 58 (a) stretching energy, (b) bending energy, and (c) adhesion energy during deformation for various parameters: area compressibility modulus, bending modulus, and specific surface energy, respectively. The diameter of the liposome, r_{ves} is 25 μm [139]

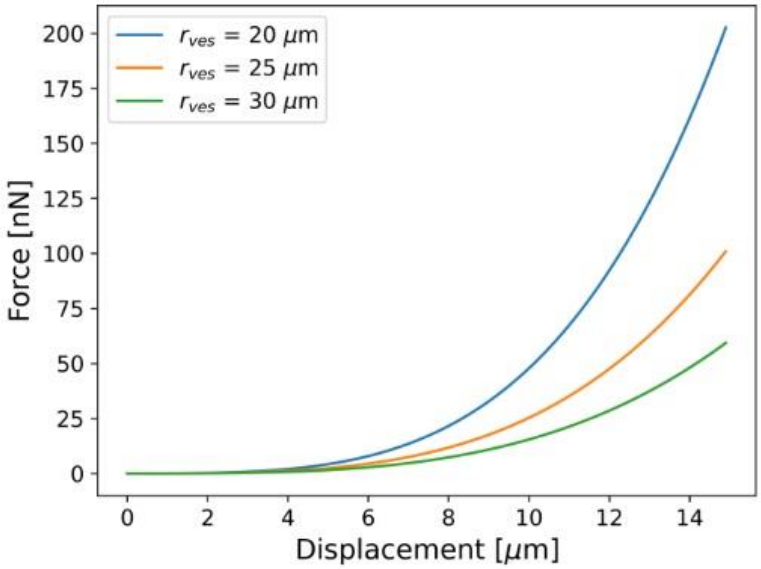

Fig. 59 Effect of liposome size on indentation force [139]

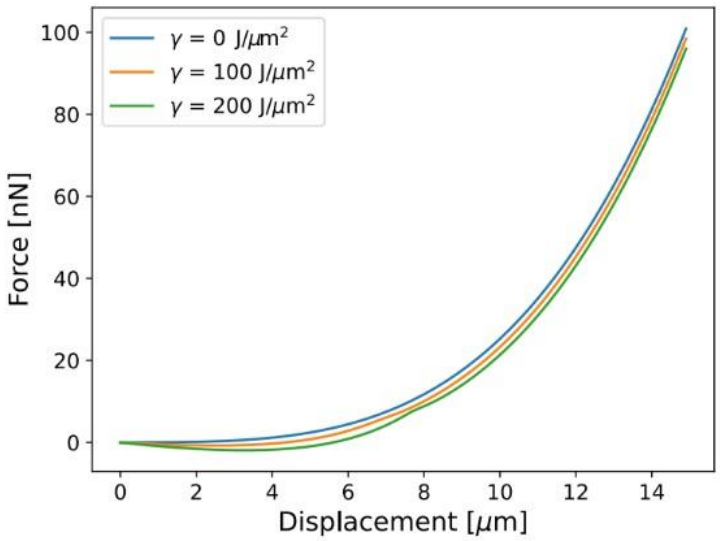

Fig. 60 Effect of specific adhesion energy on indentation force [139]

7.4 Fluid shell model

Fluid shell model is based on the Laplace equation, specifically designed for the analysis of fluid membranes. In this section, we conduct a fundamental analysis of the model's parameters and compare them to experimental data. Fig. 61 shows the change of shape in dependency on the parameter *α* which is dependent on the displacement of indentation [144].

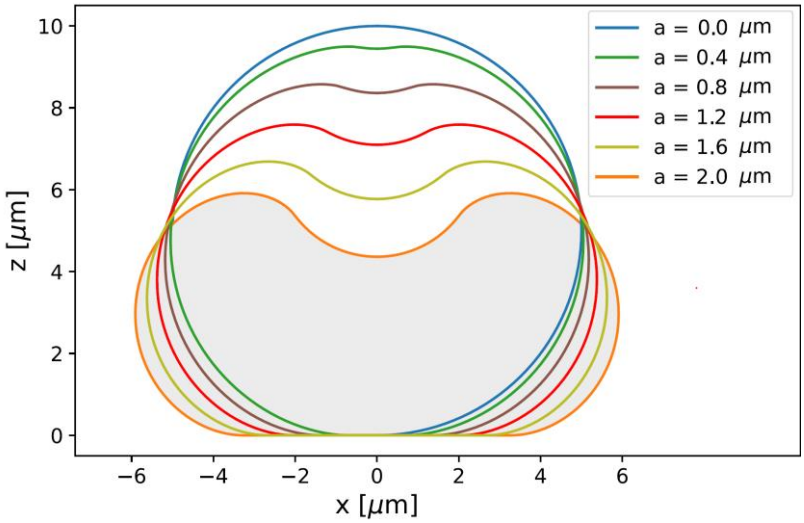

Fig. 61 Cell change shape during the indentation [144]

Fig. 62 illustrates the predicted deformation of the cell during an indentation experiment. It is evident from our findings that the cell undergoes an increase in both its lateral dimensions and the area of contact with the substrate [144].

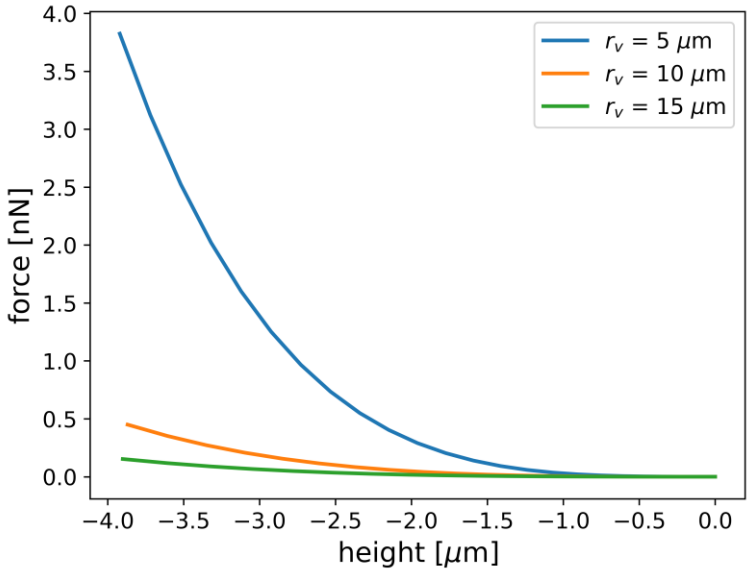

Fig. 62 Force-deformation curves of different liposome sizes, based on model with probe radius 10 μM [144]

In addition, Hertz's theory assumes that the size of the contact area is negligible compared to the cell's overall size. These measurements corroborate our model's predictions, which clearly demonstrate an increase in cell stiffness as liposome size decreases, Fig. 63 [144].

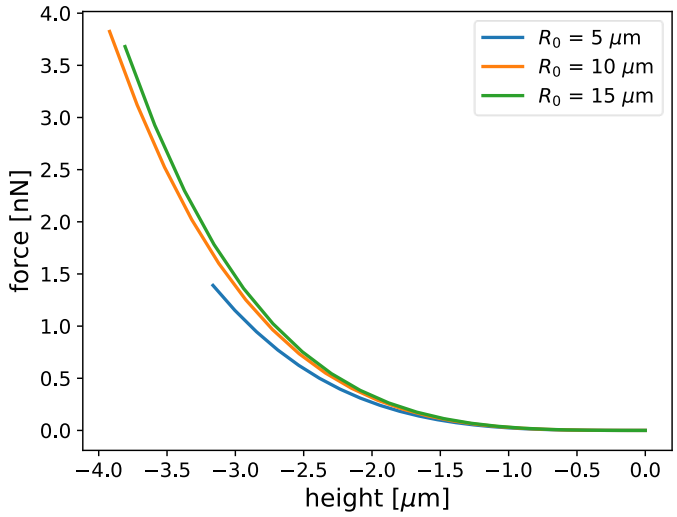

Fig. 63 Force-deformation curves of different probe sizes, based on model of liposome size 10 μm [144]

7.5 Experimental measurements - stiffness of liposomes

We have measured in total 633 liposomes. From the experimental data we have excluded data with excessive noise (74 measurements) and noncontinous loading curve (40 measurements) based on visual inspection of loading and unloading curve. For the rest of data, the stiffness in loading part was evaluated by fitting a linear function. The linear stiffness approximates the loading curve well (Pearson correlation coefficient 0.95, range 0.39–0.99). The analysis of data showed three distinct shapes of loading curve (Fig. 64). We have denoted them as nonlinear, linear and background.

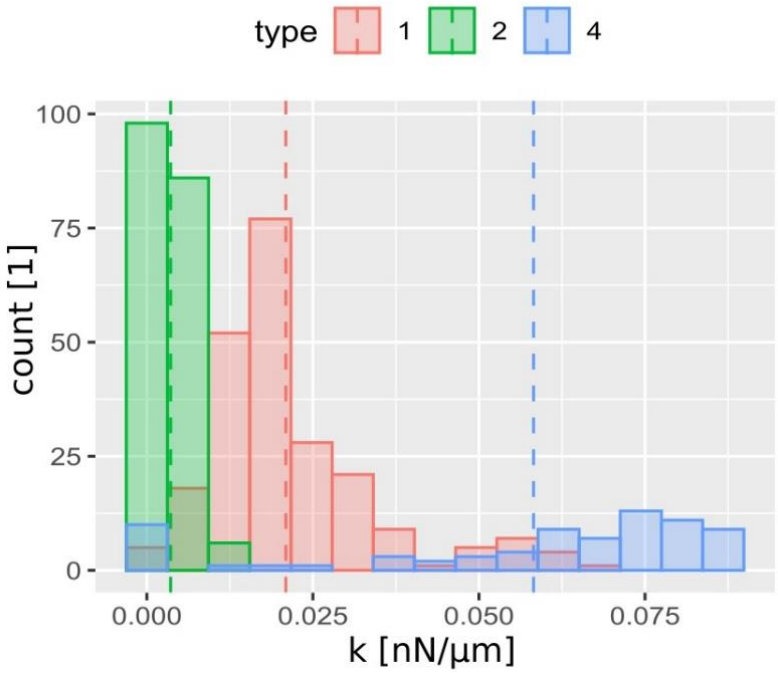

Fig. 64 Histogram by measured stiffness of liposomes (1 linear, 2 nonlinear, 4 background)

Tab. 13 Mean and standard deviations of measured stiffness for various force response

Type	Mean	Sd
Linear	0.021	0.013
Nonlinear	0.004	0.003
Background	0.058	0.028

The nonlinear curve is characterized by gradual increase in stiffness during measurement and larger deformations. Corresponds to data on liposomes reported in literature. The linear curve exhibits a sharp transition between approach phase and measured stiffness, where the measured curve has linear characteristics and lower deformation. The background curve has the steepest stiffness and corresponds to control measurements on glass substrate and was used to verify the method and calibrate the AFM tip. In general, the higher force is related to higher deformation (Fig. 65). However, despite of large number of observations we did not confirm normal distribution of measured indentation depth at any of evaluated depths and type of liposomes (Shapiro-Wilk normality test $p < 0.001$). This indicates additional factors influencing the measured stiffness in some of measured samples.

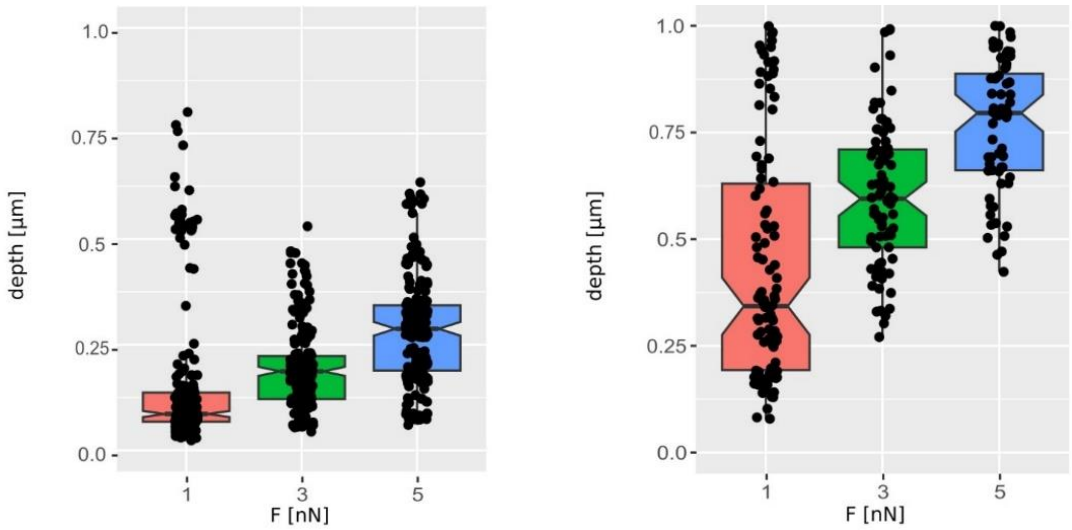

Fig. 65 Dependence between the applied force and measured deformation for (left) linear group and (right) nonlinear group

Fig. 66 (left) shows distribution of measured stifness of liposome in the linear group in dependence on the indentation force. The higher the applied force, the higher the average stiffness. However, stiffness at given force does not comply with normal distribution (Shapiro-Wilk normality test $p < 0.001$ for indentation force of 1 nN, 3 nN, and 5 nN). Pairwise comparisons using Wilcoxon rank sum test with continuity correction indicate that the stifness at applied force of 1 nN is considerably lower that the stiffness at applied force of both 3 and 5 nN ($p < 0.001$ for both forces) while there is no significant difference in stiffness at loading force 3 and 5 nN ($p = 0.095$).

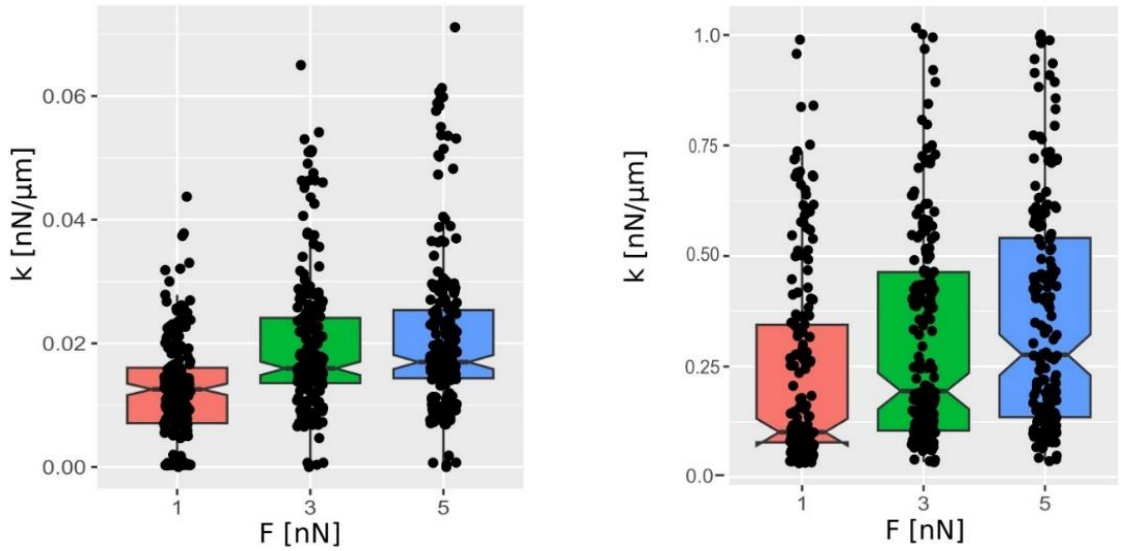

Fig. 66 Boxplot of measured stiffness at various levels of loading force for (left) linear loading curves and (right) nonlinear loading curves

Fig. 66 (right) shows distribution of measured stiffness of liposome in the nonlinear group in dependence on the indentation force. There is an obvious trend of stiffening with increased force, typical for biological materials. Similarly, to the linear group, the stiffness at given force does not comply with normal distribution (Shapiro-Wilk normality test $p < 0.001$ for indentation force of 1 nN, 3 nN, and 5 nN). Pairwise comparisons using Wilcoxon rank sum test with continuity correction indicate that the stifness between applied force of 1 nN, 3 nN a 5nN raises significantly ($p < 0.001$ for pairwise comparison between loading force 1 nN and 3 nN and $p = 0.018$ for pairwise comparison between loading force 1 nN and 5 nN).

We assume, that linear characteristics correspond to strong adhesion to the surface mediated by applied avidin-biotin complex. As most of the studies reported in Section 2 shows a nonlinear dependence with stiffness in the range of measured values, we have further analysed these nonlinear data in detail.

7.6 Continuum mechanics analysis

7.6.1 JPK software – Hertz contact model

Hertz model was chosen as gold standard to evaluate force curves for all liposomes of nonlinear characteristics. The Hertz contact model describing elastic contact between rigid spherical indentor and an elastic half-space was fitted to three indentation forces and corresponding depths using a custom fitting procedure based on iterative estimation of contact point. Custom algorithm for Hertz model fit was compared to method included in JPK SPM Data Processing (version SPM – 5.0.145, Bruker Nano, Germany). We fitted a linear model to compare Young´s modulus estimated by JPK to the same values estimated by custom algorithm (Fig. 67). Both models predict almost the same values with high correlation (R^2 = 0.89, F (1, 160) = 1340.58, p < 0.001). However, the Young´s modulus estimated by JPK is slightly higher for liposomes with higher stiffness (slope of linear fit 1.09).

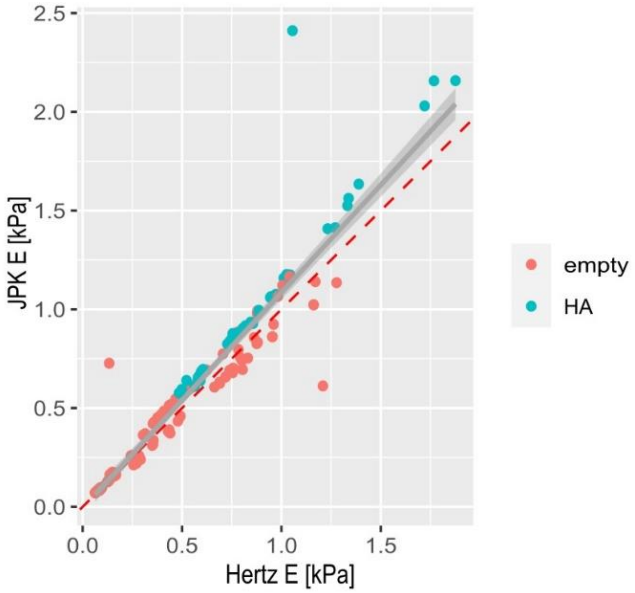

Fig. 67 Comparison of Young´s modulus evaluated by Hertz contact model at 5 nN estimated by JPK software and custom fitting algorithm. The read dashed line represents line of equality, the gray line represent linear fit with 95 % confidence intervals.

7.6.2 Custom fitting algorithm - Hertz contact model

The Hertz model provides a good fit to the AFM data, as evidenced by the high correlation coefficient between the measured and predicted values (Pearson correlation coefficient mean 0.998 for all measurements, range 0.9881–0.999). Representative loading curves are presented in Young's modulus in HA-filled liposomes (mean 1.11 kPa, range 0.30–1.85 kPa) is significantly higher than in PBS-filled liposomes (mean 0.37 kPa, range 0.62–1.28 kPa) (Wilcoxon rank sum test, $W = 423$, $p < 0.001$). The higher stiffness in HA-filled liposomes corresponds to steeper force-deformation curves Fig. 72. The results showed a high degree of agreement between repeated measurements, as indicated by the low variation between the measured curves and in the estimated Young's modulus (Fig. 72) [141].

To test repeability of estimates, each liposome was measured several times. Point estimates, confidence intervals and significance tests for the repeatability (intra-class correlation coefficient) of measurements was evaluated on the base of generalised linear mixed models. We have found excellent repeatability of measurements ($R = 0.992$, $SE = 0.0002$, $CI = [0.987, 0.995]$, $p < 0.001$). The repeatability estimates are shown in Fig. 68. Young´s modulus for individual measurement along with the range of measured values is shown in Fig. 69.

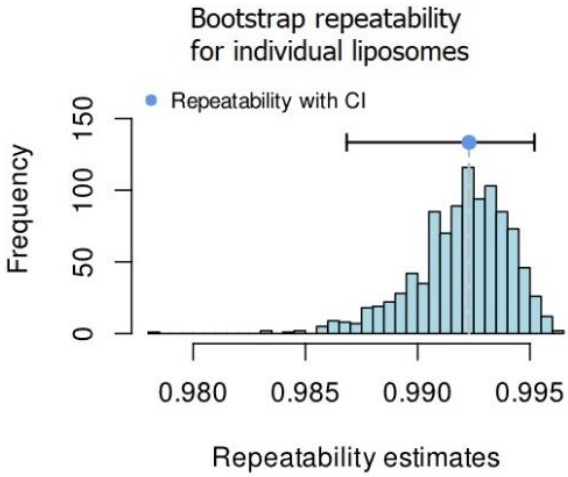

Fig. 68 Bootstrap repeatability of Young´s modulus estimated by Hertz contact model for individual liposomes at indentation force of 5 nN

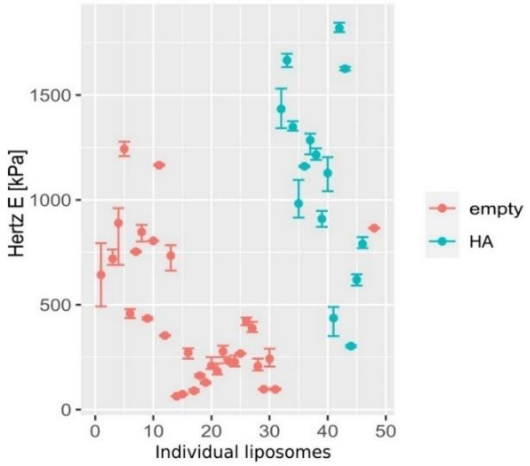

Fig. 69 Error bars shows range of estimated values of Young´s modulus estimated by Hertz contact model (minimum and maximum values) at indentation force of 5nN

Liposomes filled with HA have significantly higher Young´s modulus estimated at 5 nN than liposome filled with PBS (Wilcoxon rank sum test, $W = 69$, $p < 0.001$), Fig. 70.

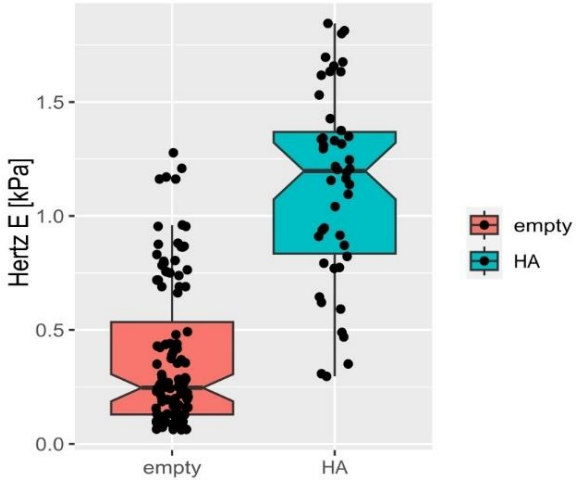

Fig. 70 Comparison of Young's modulus of liposomes filled with PBS and liposomes filled with HA

For liposome filled with PBS (Fig. 71 left), the estimated Young´s modulus is not a function of indentation force or depth (Kruskal-Wallis rank sum test $p = 0.175$, chi-squared = 3.486, $df = 2$). The Young´s modulus evaluated at indentation force 1 nN exhibits similar variance to the one evaluated at 3 nN and 5 nN (F variance test $F = 1.026$, num $df = 115$, $p = 0.892$ and $F = 1.262$, num $df = 115$, p=0.214, respectively). The difference in variance in Young´s modulus evaluated at 3 nN and 5 nN does not significantly differs (F variance test $F = 1.230$, num $df = 115$, p = 0.269).

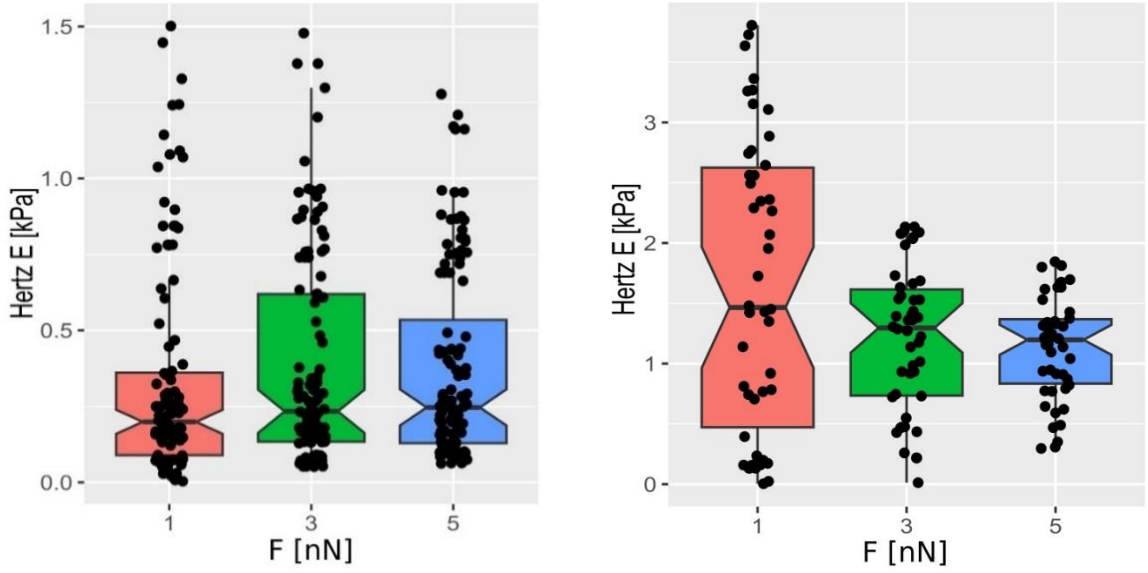

Fig. 71 Boxplot of measured Young´s modulus estimated by Hertz contact model for (left) liposomes filled with PBS and (right) liposomes filled with HA at the indentation forces 1 nN, 3 nN, 5 nN

For liposome filled with HA (Fig. 71 right), we observe decrease of estimated Young´s modulus with depth, although the observed trend is not significant (Kruskal-Wallis rank sum test $p = 0.169$, chi-squared = 3.552, $df = 2$). The Young´s modulus evaluated at indentation force 1 nN does exhibit significantly higher variance than the one evaluated at 3 nN and 5 nN (F variance test $F = 4.119$, num $df = 45$, p < 0.001 and $F = 8.313$, num $df = 45$, $p < 0.001$, respectively). The difference in variance in Young´s modulus evaluated at 3 nN and 5 nN is at border of statistical significance (F variance test $F = 2.018$, num $df = 45$, $p = 0.020$).

7.6.3 Effect of cell's size on elasticity

Linear regression (Fig. 73) was used to test whether liposome size significantly predicts Young's modulus. For both liposomes filled with PBS and HA, the effect of liposome diameter d is statistically significant and negative (β = -23.44, 95% *CI* [-28.33, - 18.56], $p < 0.001$ for the liposome filled with PBS and β = -36.53, 95% *CI* [-45.58, -27.48], $p < 0.001$ for liposomes filled with HA). The effect of liposome diameter on Young's modulus is significantly higher for HA-filled liposomes (ANOVA $p = 0.008$) [141].

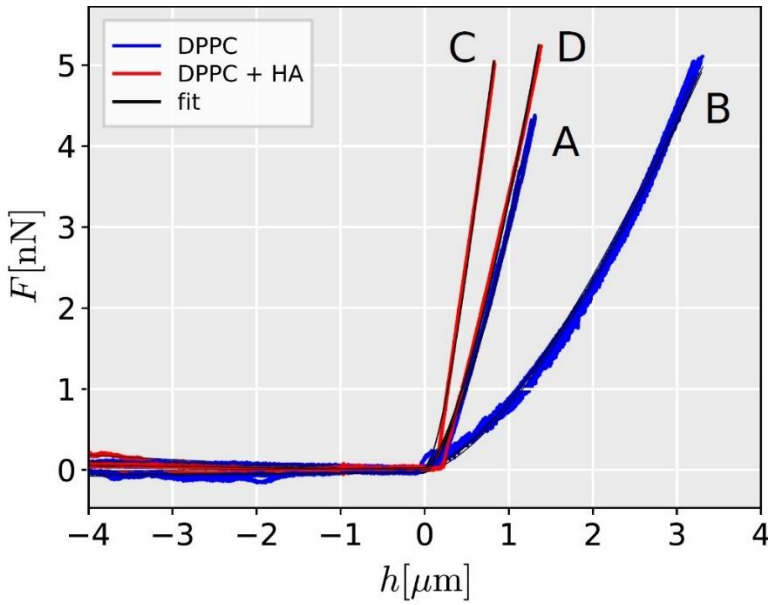

Fig. 72 Measured indentation curve for DPPC liposomes in PBS filled with (DPPC) PBS and (DPPC+HA) HA solution. Fit of indentation by Hertz contact model for hemispherical AFM tip is shown [141]

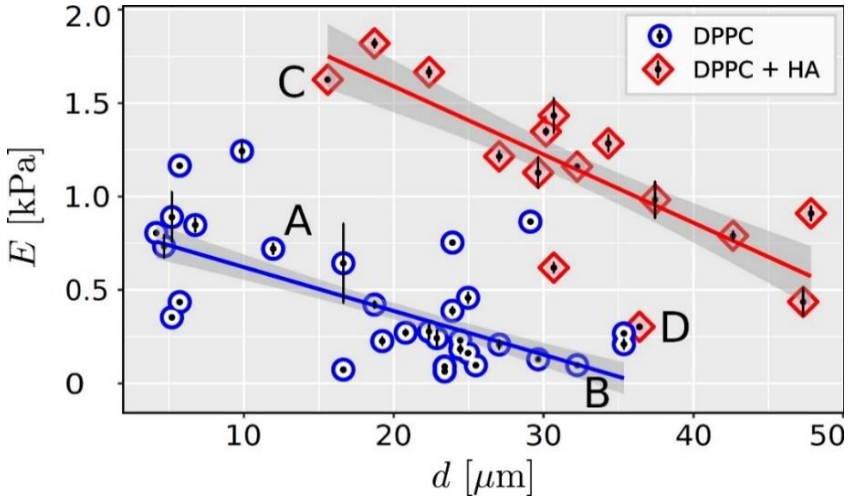

Fig. 73 Linear regression plot with 95 % confidence intervals (shaded areas) showing measured dependence between the size of DPPC liposomes and Young's modulus estimated from Hertz model measured data along with the range of measured values are shown for liposomes filled with PBS and HA solution, denoted as DPPC and DPPC+HA, respectively [141]

7.6.4 Experimental evaluation of force distribution between cytoplasm and biomembrane

Cell models with viscou cytoplasm exhibit on average higher stiffness than liquid-filled liposomes (Fig. 74 A, B), indicating an important role of cytoplasm in load transfer (Hertz model elasticity modulus 1360±271 Pa and 270±104 Pa for HA-filled and fluid-filled liposomes respectively, the difference is statistically significant t (109) = 32.47, $p <$ 0.001). In initial contact, the load bearing capacity of both membrane and cytoplasm cell is comparable (Fig. 74 B, C). However, for deformations larger than 0.2 μm, the effect of cytosplasm prevails and cytoplasm bears more than 80% of the overall load [142].

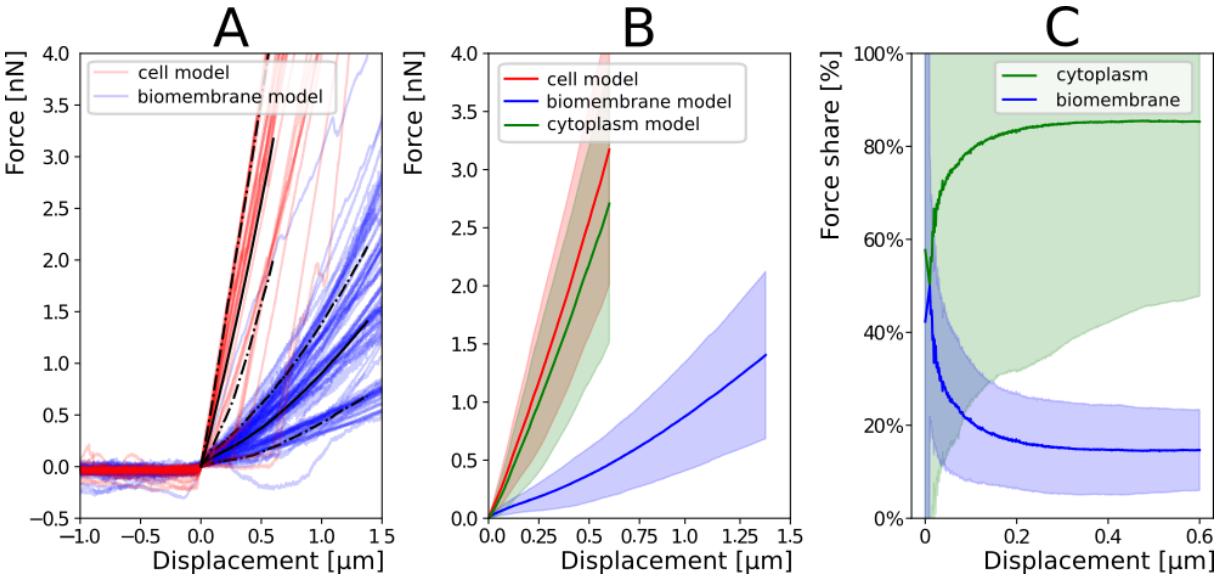

Fig. 74 (a) Force deformation curves of whole cell model (biomembrane + viscous cytoplasm) and empty liposome (biomembrane model); (b) average force curves and estimation of load transmitted through cytoplasm; (c) relative contribution of cytoplasm and biomembrane to the load bearing capacity [142]

7.7 Prescribed shape model

Measured curves were fitted with newly defined liposome deformation model. The model is based on prescribed axisymmetrical geometry and dependence between the deformation and force is estimated from the deformation energy of membrane. As the bending energy is negligible, only the stretching energy was considered within this analysis. The stiffness of the membrane in stretching is defined by the area compressibility modulus K_A.

Repeated measurement of K_A on various liposomes shows excellent repeatability by tests for the repeatability (Fig. 75), intra-class correlation coefficient R = 0.90, SE = 0.025, 95 % CI [0.84, 0.936], $p <$ 0.001). The range of measured values of K_A along with the mean values for individual liposomes is shown in Fig. 76.

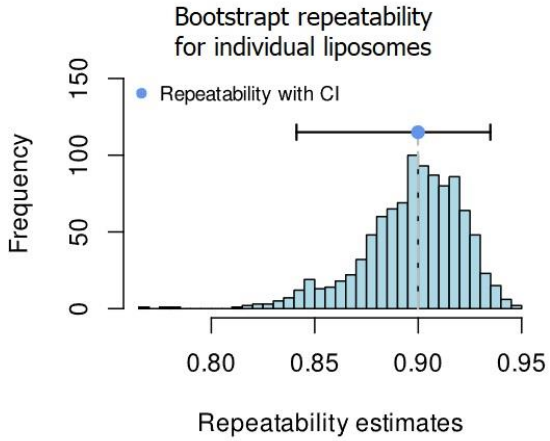

Fig. 75 Bootstrap repeatability of area compressibility modulus estimated by prescribed shape model for individual liposomes at indentation force of 5 nN

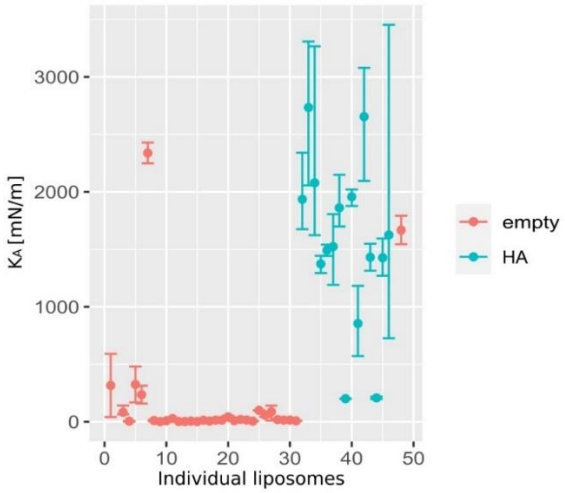

Fig. 76 Mean values of compressibility modulus estimated by prescribed shape model for individual liposomes. Error bars show range of estimated values of area compressibility modulus (minimum and maximum values) at indentation force of 5 nN

Wilcoxon rank sum test shows that the area compressibility modulus estimated for PBS filled liposomes is significantly lower that the area compressibility modulus estimates for HA filled liposomes ($W = 517$, $p < 0.001$). This difference is likely to be caused by force transmission through viscous core of HA – filled liposomes and does not necessarily correspond to biomembrane stiffening.

Distribution of area compressibility modulus measured at three indentation depths does not comply with normal distribution (Shapiro-Wilk normality test $W = 0.626$, $p < 0.001$; $W = 0.779$, $p < 0.001$; $W = 0.299$, $p < 0.001$ for indentation load 1 nN, 3 nN, and 5 nN, respectively). Area compressibility modulus measured in liposomes filled with PBS has significantly decreases with indentation load (Kruskal-Wallis chi-squared = 68.83, $df = 2$, $p < 0.001$). Values of means and quartiles are shown in Tab. 14 and differs significantly from each other based on post-hoc analysis (pairwise comparisons using Wilcoxon rank sum test $p < 0.001$ for all mutual comparison at indentation load of 1 nN, 3 nN, and 5 nN). The difference is not only in the value of area compressibility modulus, but also in the variance of data, Tab. 14 (F test $p < 0.001$, $df = 115$, $F = 23.42$, $F = 4.16$, and $F = 0.17$ to compare variances indentation load of 1–3 nN, 1–5 nN and 3–5 nN, respectively).

Tab. 14 Median and interquartile ranges for area compressibility modulus estimated from measurements of PBS-filled liposomes at three indentation loads using prescribed shape model

Indentation load	**1 nN**	**3 nN**	**5 nN**
Median [mN/m]	257.25	52.74	13.12
1st quartile [mN/m]	41.71	14.12	6.22
3rd quartile [mN/m]	643.37	200.00	31.49

Liposomes filled with HA have significantly higher area compressibility modulus estimated at 5 nN than liposome filled with PBS (Wilcoxon rank sum test, $W = 517$, $p < 0.001$) (Fig. 77).

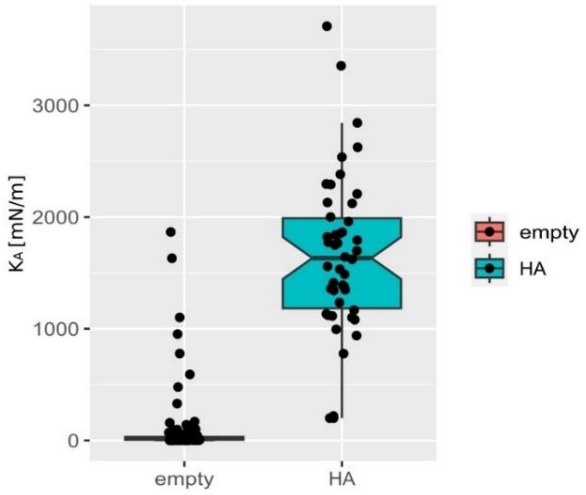

Fig. 77 Comparison of area compressibility modulus of liposomes filled with PBS and liposomes filled with HA

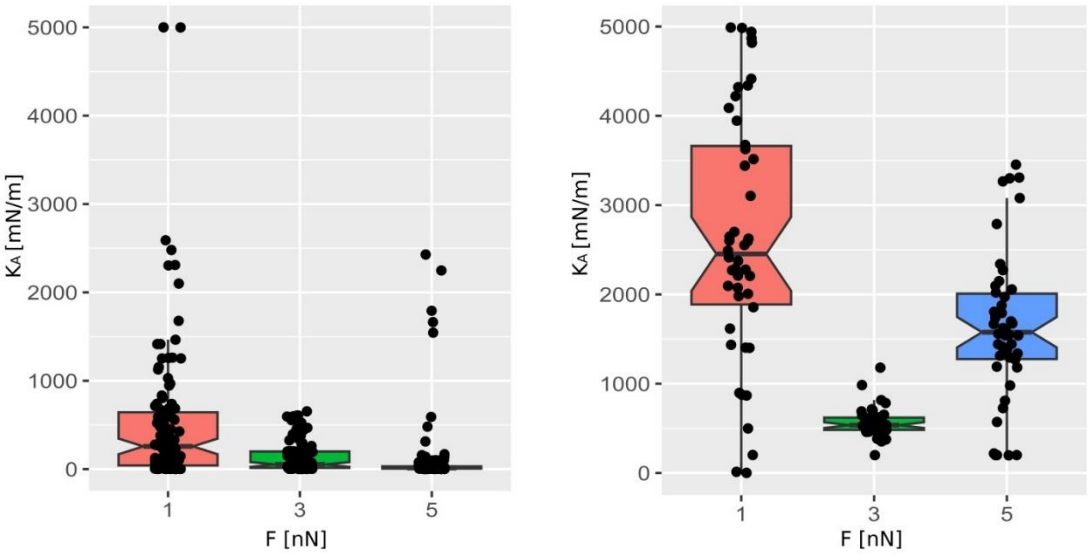

Fig. 78 Boxplot of measured area compressibility modulus estimated by prescribed shape model for (left) liposomes filled with PBS and (right) liposomes with HA at indentation forces of 1 nN, 3 nN and 5 nN

7.8 Fluid shell model

The dataset for nonlinear force-deformation curves was fitted with the fluid shell model. The material parameter of the model is the biomembrane area compression modulus K_A. The model proved excellent repeatability (Fig. 79), intra-class correlation coefficient R = 0.992, 95 % CI [0.978, 0.995], p < 0.001). The range of estimated values of area compression modulus at indentation force 5 nN is shown in Fig. 80.

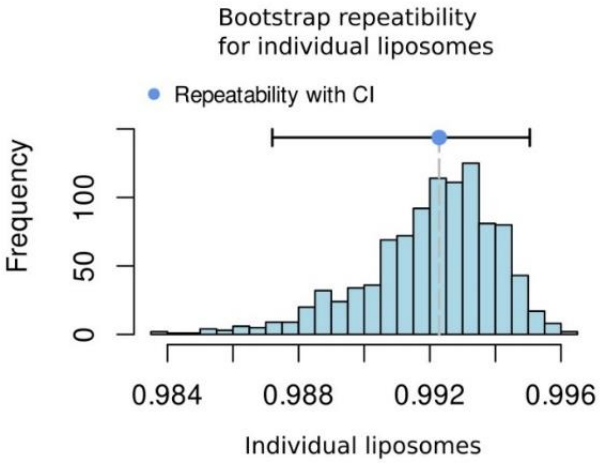

Fig. 79 Bootstrap repeatability of area compressibility modulus estimated by fluid shell model for individual liposomes at indentation force of 5 nN

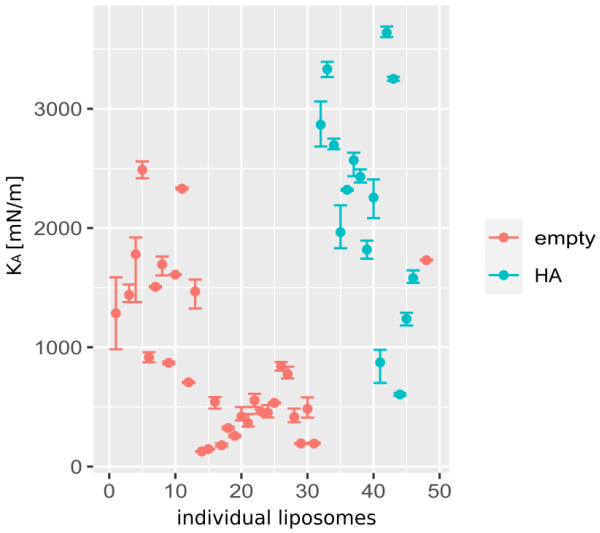

Fig. 80 Mean values of area compressibility modulus estimated by fluid shell model for individual liposomes. Error bars show range of estimated values of area compressibility modulus (minimum and maximum values) at indentation force of 5 nN

Similarly, to the previous models, the area compression modulus does not exhibit normal distribution (Shapiro-Wilk normality test 0.951, p < 0.001 and W = 0.816, p < 0.001 for HA and PBS-filled liposome, respectively) and the model is suitable for detecting HA-filled liposomes by their higher stiffness (Wilcoxon rank sum test W = 4913, p < 0.001).

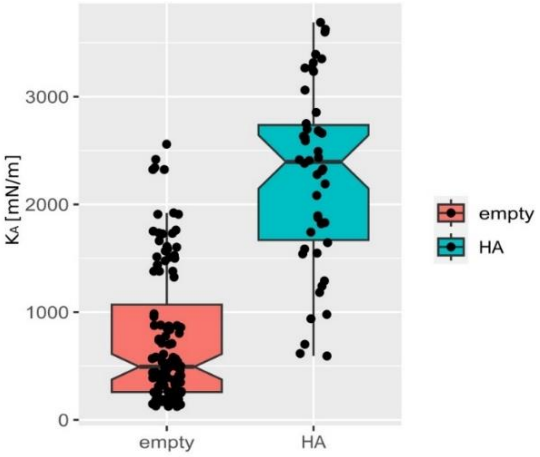

Fig. 81 Comparison of area compressibility modulus of liposomes filled with PBS and liposomes filled with HA

Area compressibility modulus measured in liposomes filled with PBS does not significantly differs at various indentation loads in means (Kruskal-Wallis rank sum test chi-squared = 3.088, *df* = 2, *p*-value = 0.214) and in variances (F test, *p* = 0.652, *df* = 115, *F* = 1.088; *p* = 0.253 *F* = 1.238; and *F* = 1.183 to compare variances indentation load of 1–3 nN, 1–5 nN, and 3–5 nN, respectively).

Tab. 15 Median and interquartile ranges for area compressibility modulus estimated from measurements of PBS-filled liposomes at three indentation loads using fluid shell model

Indentation load	**1 nN**	**3 nN**	**5 nN**
Median [mN/m]	398.2	459.98	493.0
1st quartile [mN/m]	178.6	266.38	258.1
3rd quartile [mN/m]	721.6	731.90	1069.4

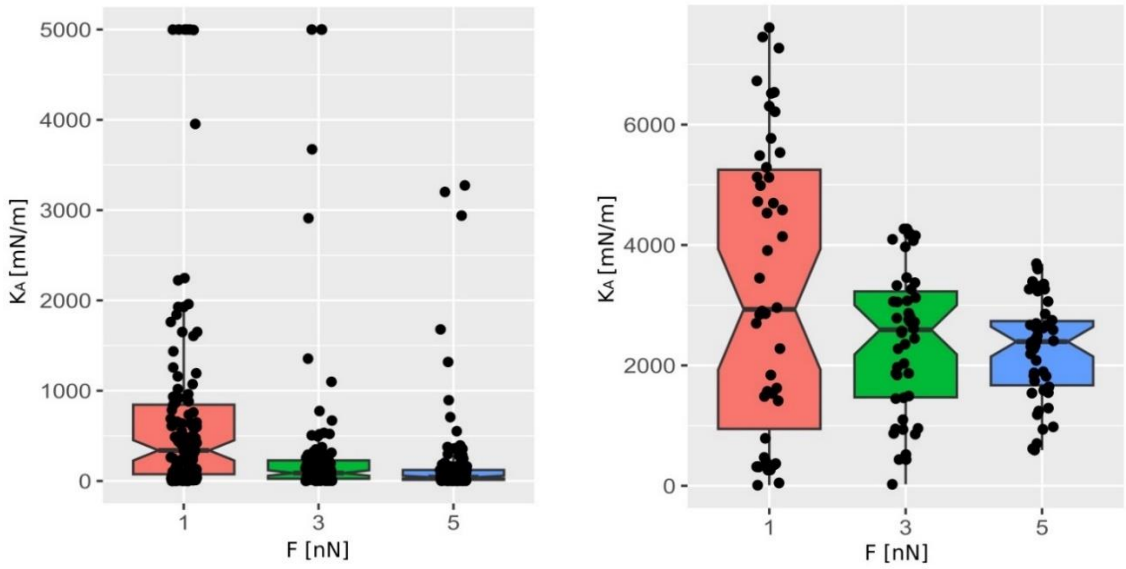

Fig. 82 Boxplot of measured area compressibility modulus estimated by fluid shell model for (left) liposomes filled with pbs and (right) liposomes filled with ha at indentation forces of 1 nN, 3 nN, and 5 nN

For HA-filled liposomes we observed slight nonsignificant decrease in area compression modulus with indentation force (Kruskal-Wallis chi-squared = 3.552, *df* = 2, *p* =0.1693). With increasing deformation, the estimated values of Ka are more homogenous with less variance (F test, *df* = 45, *F* = 4.1188 *p* < *0.001*; *F* = 8.314 *p* < 0.001; and *F* = 2.0184 *p* = 0.0238 to compare variances indentation load of 1–3 nN, 1–5nN and 3–5nN, respectively).

7.9 Nanoindentation – microcompresion testing

The nanoindentation measurements presented significant challenges that hindered data analysis and evaluation. Primarily, the attachment of liposomes to the Petri dish bottom proved inadequate, as they slipped during indentation due to weak fixation. Secondly, the absence of an inverted microscope for visualization and the limited tip displacement range of the nanoindenter (maximum 10 µm) restricted the characterization process. Fig. 83 depicts a representative force-displacement curve obtained during these measurements. The considerable data scatter and noise within the curve serve to illustrate the limitations of this technique for this specific application. Consequently, microcompression testing utilising Bruker's Hysitron BioSoft (Bruker, Corp.) was employed as an alternative approach [146].

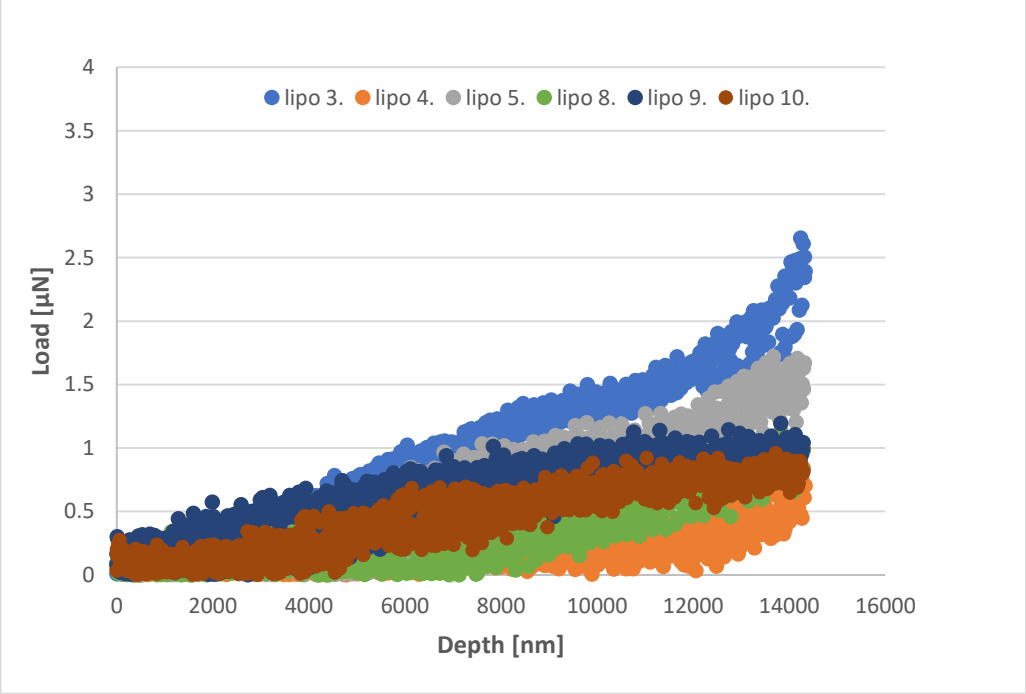

Fig. 83 Force-displacement curves obtained by microcompresion testing using instrumented nanoindentation

7.10 Modified Overbeck model

The Young´s modulus modulus of membrane was determined by compression testing and analysis using a modified Overbeck [55]. The limited number of measured liposomes was caused by technical problems with experimental device. Therefore, this measurement is not evaluated statistically and serves as pilot data.

Tab. 16 Young´s modulus modulus of measured liposomes

Measured liposome	***E* modulus** [MPa]
1	5.526
2	1.411
3	2.478
4	6.813
5	10.544

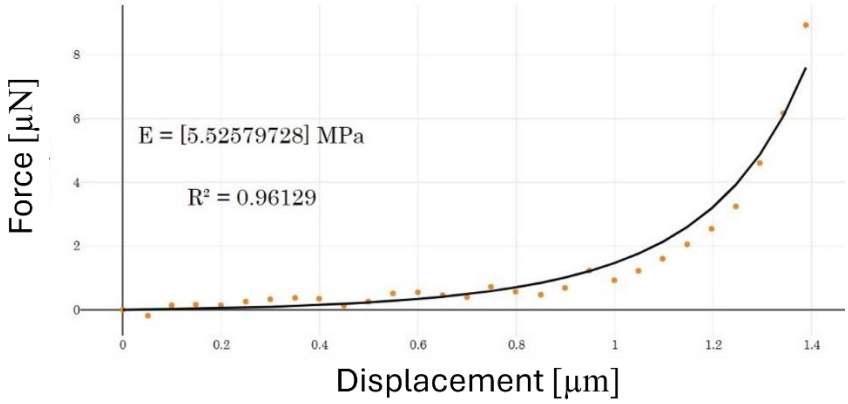

Fig. 84 Fitted modified Overbeck to estimate the Young´s modulus of liposome

8 Discussion

Mechanical testing of cells is crucial for understanding their structural integrity, response to external forces and overall biomechanical properties. As has been shown [63], there is considerable variability in the mechanical properties of living cells. Cells in their dynamic environment are exposed to external forces that can cause structural degradation. The measured stiffness of a cell can be affected by various factors, such as viral infection or malignancy or by differences between experimental setups. To verify the latter, we developed a method to produce artificial cells to be used as a reference in mechanical testing. In this work, we used liposomes produced by a microfluidic device as standards for testing. Lipid vesicles and liposomes have been used for a long time as important models for the study of the mechanical properties of cells. The composition of the liposome is like the structure of a cell [7][9]. Liposome is a small artificial spherical vesicle consisting mainly of a lipid bilayer and an internal compartment isolated from the external environment. The lipid bilayer represents the cytoplasmic membrane and the internal compartment of liposome the cell cytoplasm [8].

Firstly, we rewieved the method of liposome production. The most used methods of liposome production [13] are gentle hydration method, electroformation, droplet emulsion transfer method, pulsed-jet flow method and finally microfluidics. Commonly used methods are time-consuming and require preparation. In our research we proceeded a complex laboratory to the production of liposomes using a microfluidic device [17][140]. Microfluidics production compared to the traditional methods enables the creation of liposomes with uniform sizes, high encapsulation efficiencies and symmetrical lipid distributions. Furthermore, microfluidic platforms enable the generation of single or multi-compartment liposomes, creating opportunities for intracellular studies. It has been proposed that liposomes ranging from 10 to 100 μm can be produced using a microfluidic device, i.e. the giant unilamellar liposomes GUVs [11]. In our study we have observed similar range of liposome size, Fig. 41. The size of the liposomes was crucial for our study due to the potential application of suitable mechanical testing [23][151][154]. To investigate their mechanical properties, we prepared two types of liposomes: those filled with PBS and those filled with HA. The liposomes filled with HA were larger in size compared to the PBS-filled ones [140][145][147]. Although microfluidics is a new method for manufacturing liposomes, the characteristics of laminar flow and tuneable mixing in microfluidics channels have a lot of advantages in comparison to conventional methods, such as sonification, lipid film preparation or bulk method [17]. Just by changing the flow rates, liposomes with smaller size could easily be formed [17][18]. MHF method provides a new platform to optimization and development of liposomes in biomedical fields. The results obtained by MHF method demonstrate that, liposomes created by MHF method have smaller size and uniform size distribution than liposomes created by bulk method [18].

The purpose of its use, it is necessary to select the appropriate type of microfluidic device used for production themselves [140]. 3D printing offers several advantages over traditional microfabrication tools for creating microfluidic devices, including accessibility, low cost, efficiency, versatility, and rapid prototyping. However, challenges such as material selection and limitations on channel dimensions must be addressed. While 3D printing offers numerous benefits for microfluidics, it is crucial to carefully evaluate various factors and limitations before switching from traditional fabrication methods. The selection of resin material and printing resolution are critical considerations as they can impact device performance [122]. Therefore, we have proposed, tested, and verified a specific technology for the manufacturing of microfluidic device using stereolitography and polyjet technology. We have produced several types of microfluidic devices: from simple one to devices with complex geometry [152][153]. A variety of models were designed with different channel sizes and angles between them. To test the feasibility of utilising the department's 3D printers, we produced a microfluidic device based on the dimensions of a CNC production. Firstly, we produced the microfluidic devices using stereolithography on a Projet1200 3D printer. The model, also known as a Y-junction, has junction angle of 30 degrees and two input channels with a diameter of 0.5 mm, as well as an

output channel with a diameter of 0.4 mm. The second type of microfluidic device was also printed in the block. It was a 'T'-shaped microfluidic device that we intended to expand with more input channels. The crossing channels were clogged due to an accumulation of individual layers of material. To address the printing issue with the 'T' type microfluidic device, a version without the block was created. The printer was tested for its ability to print microfluidic devices with channels of varying sizes. Specifically, we tested the printing of the Y-junction type, which is a basic type of microfluidic device. Microfluidic devices with channels of 0.4, 0.5, 0.75, 1 mm were printed. Since liposomes are often used as drug delivery system, we printed microfluidic devices with multiple channels for drug encapsulation [140][145][147]. Microfluidic device fabrication without a block has been shown to be more successful than printing devices in a block. Microfluidic devices with multiple channels for drug encapsulation were printed, in addition to two- and three-channel microfluidic devices. This type of microfluidic device is shown in Fig. 36 [140].

It is crucial to note that the flow rate in the channels significantly affects the formation of liposomes. Therefore, selecting the appropriate angle is essential to control the flow rate, and the Reynolds number should be calculated based on the liquid's viscosity.

Microfluidic devices with varying angles between channels were also manufactured using polyjet technology on a Stratasys J750 3D printer [152]. This technology was used to fabricate microfluidic devices with channels at angles of 30, 60, and 90 degrees. In article [122], the autors compared the basic "Y" junction microfluidic device fabricated by three types of additive manufacturing technologies: FDM, polyjet, and DLP-SLA, the design of which was optimised for each printer. Each technology printed the microfluidicdevice with different size of channels. FDM was suitable for microfabrication with a minimum feature size of 321 ± 5 μm, polyjet produced channels with a minimum size of 205 ± 13 μm and DLP-SLA with size of 154 ± 10 μm [122]. It should be noted that in our case the size of channels agrees with the previously reported values for polyjet technology. The size chosen was based on the printing capabilities of our 3D printers and the purpose of producing GUV vesicles, which are typically in the micrometre range. The fabrication of our microfluidic devices, from their design in the CAD system to the finish prototype (microfluidic device), lasted in case of stereolitography about 8 hours and polyjet only 1 hour. Postprocessing of 3D printer Projet 1200 in comparison with 3D printer Stratasys J750 takes also more time [152].

The mechanical properties of cells refer to their physical characteristics and behaviour under mechanical forces, including stiffness, elasticity, adhesion, and deformation [96][141][142]. In the presented study, we have use liposome as a mechanical model of a cell. It has been shown that the type of used lipid a crucial factor in the formation, testing of liposomes and plays a fundamental role in evaluating the stiffness of liposomes [102]. Hence, we produced liposomes using DPPC lipids only as the common lipid with relatively hight transition temperature to avoid raft formation. AFM measurements were evaluated using a Hertz contact model, which is the mainly used model to determine the mechanical properties of cell [96][102]. The force-displacement curves are in case of AFM measurements usually evaluated by a proprietary software e.g. JPK DP software [78]. Manual setting of the initial contact point required in commercial software might introduce an operator bias. Therefore, we developed custom fitting algorithm [103]. We have further evaluated the effect developed of cell size on the estimated Young's modulus. We have shown that there is a considerable dependence between the size of the measured liposome and its stiffness. Our findings agree with the previous studies of [104], who observed higher stiffness in smaller liposomes. The observed effect of liposome size is consistent with the shell theory of cell deformation [76][77]. Real-time deformability cytometry also indicates higher deformation for larger cells of the same phenotype as shown in our study [141]. The scattering of data indicates the presence of other factors influencing the measured mechanical response. A parameter that has not been fully evaluated is liposome adhesion. In a theoretical and experimental study was shown that extensive cell adhesion increases cell membrane tension and stiffness [105]. AFM measurements also indicate that the stiffness of adherent epithelial cells increases with increasing the projected area of apical cells [105].Therefore, liposomes adhered to

the surface considerably were excluded from the analysis. Overbeck et al., 2017 [55] showed that, in addition to cell size, osmotic pressure could affect cell response, where higher osmolarity of the culture contributes to a decrease in cell stiffness.

The presented results were measured in liposomes as cell models. This approach allows for reducing variability in input parameters as experimental samples with fully controlled composition and geometry are prepared. Liposomes mimic basic cell structure but may not fully describe the active behavior of living cells. The cell is a heterogeneous structure with a high level of internal organization. For example, it was shown that anisotropy of the cytoskeleton induces non-axisymmetric deformation and stiffness of subcellular structures affect the local mechanical response [106]. Prolonged or repeated indentation of single cells can result in remodeling of the cytoskeleton [29] that could further influence cell stiffness. To provide a more realistic artificial cell model, HA-filled liposomes were tested[141][142]. The high molecular weight and the semi-flexible chain of HA induce viscous and elastic properties as we may observe in the cytoplasm [107][108]. The viscosity of the HA solution used (100 Pa s) corresponds to the viscosity of the cell cytoplasm [106][109][110]. The artificial cytoplasm (HA) makes cells stiffer and improves their potential to transmit a load, like that of living cells. It could be assumed that the filled liposome would be closer to the continuum and therefore satisfy the assumptions of the Hertz model. However, the addition of HA that mimics the cytoplasm increases the effect of cell size on the estimated Young's modulus. Our results therefore indicate that the inner environment should be considered in the modeling of cell mechanics. Further research is warranted to quantify the dependence between cell size and stiffness in confluent and highly adhered living cells with complex internal organization [141].

Within the present study, we have developed a mathematical model to describe the relationship between the intrinsic properties of a cell membrane and its deformation by a spherical indenter[139]. The model considers the deformation energy due to hydrostatic tension, bending, and adhesion to the substrate and indenter. Specifically, we have employed a cortical shell–liquid core model, where the liquid core is surrounded by an elastic cortical membrane [110]. Our analysis demonstrates that the bending energy is approximately 10^6 times smaller than the energy induced by biomembrane stretching [139]. This small bending energy is attributed to the low bending modulus, which is related to the thinness of the membrane in the range of tenths of nanometers [111]. Therefore, if the primary mode of deformation is stretching, the bending energy can be neglected, simplifying the model. Similar assumptions have been adopted in the model by Overbeck et al. and are common in liquid drop models [55][110]. Experimental measurements of DPPC liposomes by Delorme et al. indicate that the liposome stiffness increases with the liposome radius [104]. This finding agrees with the predictions of our model, as shown in Delorme et al. reported an average liposome stiffness of 25 pN/nm for liposomes with a radius of 0.15 μm [104]. In our simulations, we analysed GUVs with a radius of 25 μm and a stiffness of 15 pN/nm. However, it should be noted that the study by Delorme et al. and our results differ considerably in terms of liposome size, indentation depth, and the applied AFM tip [104]. Our model predicts a nonlinear force/displacement curve, which is typical for biological materials [112]. In contrast to the Hertz model, the proposed model exhibits a relatively large region of low stiffness, often referred to as the toe-off region in tissue mechanics [139]. Consequently, fitting the displacement curve with the Hertz model may bias the contact point and underestimate the cell height. Theoretical analysis of adhesion indicates that cell adhesion could influence the measured force-displacement curve and give rise to negative tip forces. This behaviour, known as the jump-to-contact point [28], has been observed experimentally. Adhesion force is typically characterized by pull-off AFM measurements, in which the AFM probe is attached to the cell surface and then retracted [113].

Taking into the cell size and different adhesion between the cell and the AFM tip or substrate, which can further improve adhesion analysis. Although force sensing techniques employ various shapes of indenters, such as flat planes, Berkovich pyramidal tips, or spherical tips the geometry in our model is limited to a spherical indenter of diameter R_0 and a spherical cell [114]. However, the model can be easily modified for a flat tip by assuming a considerably larger radius R_0 than the cell. The model is also

valid for a Berkovich tip if the angle ϑ represents the angle of the pyramidal tip and the area of the first segment is changed from a spherical cup to a pyramid. Our simulation assumes that the cell is deformed from an ideal sphere, meaning that the reduced volume of the initial shape equals one [115]. Therefore, the cell membrane is predominantly deformed by tension during the initial stages of displacement. In most cells, the cell area is larger than the area corresponding to a hypothetical cell of the same volume, resulting in a reduced volume smaller than one [116]. In such cases, the cell can assume various shapes with the same reduced volume, and during the initial deformation, the membrane is primarily deformed by tension to a lesser extent, with the cell shape primarily determined by a minimum in bending energy [117]. In the proposed model, the reduced volume decreases due to membrane extension from 1 to 0.97 for tip displacements ranging from 0 to 15 μm, respectively. The model is also applicable to cells with reduced volumes within the stated range, but should be modified to consider only positive values of the relative area deformation Θ. If the reduced volume is lower than the values predicted for a spherical cell, bending deformation should be considered. In our model, the inner volume of the cell is assumed to be filled with an ideal incompressible liquid that does not share deformation energy. However, cells are much more complex in their internal structure, with various types of filaments, a nucleus, and other organelles [118], which may affect the applicability of the liquid model. Cell volume compressibility could be incorporated by assuming volumetric strain energy directly or by replacing the internal structure with a spring representing the stiffness of the cell's inner environment [124][139].

Within this work we also presented a model based on the Laplace equation, specifically designed for the analysis of fluid membranes. Despite its simplicity in formulation, this model holds the potential to yield predictive insights. Experimental measurements have revealed that smaller liposomes generally exhibit greater stiffness than their larger counterparts [9][119]. These measurements corroborate our model's predictions, which clearly demonstrate an increase in cell stiffness as liposome size decreases, Fig. 63. The presented model is based on single material parameter: the area compressibility modulus K_A. The area compressibility modulus might be estimated by alternative methods, e.g. micropippete aspiration or flicker noise spectroscopy analysis. The area compressibility modulus of DPPC was found to be 0.23 N/m with micropipette measurements and 0.56 N/m with neutron spin echo spectroscopy [120]. For the simulation, the value of 0.2 N/m was adopted. The values estimated from experimental curve range from 0.40 to 0.49 N/m, Tab. 15.

These data are close to the previously reported values. The model is founded upon the adaptation of Laplace's law for a spherical cell enveloped by a fluid membrane. The development of a differential shape equation assumes of membrane fluidity, which implies a constant mean curvature in the membrane. This uniformity in curvature is achieved in the free membrane. However, it is noteworthy that the mean curvature varies within the regions of contact between the spherical tip and the flat substrate. One could argue that lipid mobility is reduced in these contact areas, and as a result, these regions fall outside the applicability range of Laplace's law. The model is primarily suited for structures where the cell membrane plays a pivotal role in bearing external loads, such as liposomes or red blood cells. Its suitability for cells with intricate internal environments requires further validation. For such complex structures, the model can be enhanced by incorporating additional energy terms. This expansion could involve considering the influence of factors like the cytoskeleton or deformation of the inner cell environment. Similarly, the model could incorporate adhesion energy considerations in contact with the AFM tip and the substrate [121]. The model could also be easily modified for a pyramidal shape of indentor by modification of boundary conditions in shape equation derivation [144].

As the previous studies clearly indicated higher stiffness in HA filled liposomes, we further studied the contribution of biomembrane and cytoplasm to the cell mechanical stiffness. We experimentally determined the stiffness difference between DPPC liposomes filled with hyaluronic acid (HA) that mimic the cellular cytoplasm and PBS-filled liposomes [142]. The modulus of elasticity of HA-filled liposomes (421 Pa to 2600 Pa) aligns with the range reported for cancer cells (421 Pa for melanoma to 2600 Pa for dysplastice sophagus) [123]. This value is lower than that of healthy cells, whose elasticity modulus can be as high as 40 kPa for skin cells [123]. The lower stiffness of cancer cells is likely due

to cytoskeletal disorganization and a reduction in actin filaments [124]. Our simplified cell model, lacking a cytoskeletal component, supports this notion, suggesting the cytoskeleton destruction in enhancing cancer cell compliance.

Studies have shown the feasibility of reconstructing actin mesh within giant unilamellar vesicles [125]. Schäfer et al., 2015 employed AFM to study the force response of liposomes with and without assembled actin shells. By analysing force-deformation curves in their publication and using the same method as in our study, we found that liposomes with actin shells bear roughly twice the load compared to pure liposomes. This indicates that approximately 50% of the load is transmitted through tension in the actin shell. The actin mesh strengthens the lipid membrane by increasing its rigidity to bend and shear [125]. Assuming a linear superposition effect, we can speculate, based on our data and Schäfer et al.'s work [102], that a biomembrane with an actin cytoskeleton transmits 40% of the load, while the cytoplasm transmits 60% at higher deformations. However, this conclusion requires further investigation due to the limited amount of published data. Furthermore, this assumption neglects the role of other cytoskeletal elements such as internal actin mesh or microtubules, which are crucial for cell movement [126].

The observed difference in the modulus of elasticity between our model and the reported value for cells suggests that the internal cytoskeleton plays an important role in contributing to the high stiffness of normal cells. To study the influence of internal organization on cell stiffness, a nanostructuretural approach is necessary describing individual cell components [127]. As our cell model does not contain inner organization, it could be treated as continuum materials with heterogeneous constitutive properties. In the simplest approach, the cell model is considered as a uniform elastic continuum. Its mechanical properties can then be directly estimated from AFM force-deformation curves using the Hertz contact model [128][129]. Alternatively, the cell can be modeled as a ball with an incompressible fluid center surrounded by a tougher elastic shell, known as the cortical shell-liquid model [130]. The basic cortical shell model is based on the Young-Laplace equation, which relates tension, pressure, and cell radius [131]. However, no relationship between mechanical properties and cell size was reported in an experimental study of HeLa cells [132]. Our results, indicating a prominent role for the cytoplasm in load transfer, Fig. 74 can explain this discrepancy. The cell filled with viscous cytoplasm behaves more like an elastic object than a fluid-filled balloon. The mechanical stiffness of a cell depends on the depth of the indentation, a well-known factor when evaluating the modulus of cell elasticity with Hertz/Sneddon models [133]. According to our measurements in Fig. 74, the membrane plays a more critical role in load transfer in small deformations. At these low strains, membrane bending dominates, and the contribution of the cytoplasm is minor. This is due to the difference in biomembrane elastic moduli. The biomembrane bending modulus, on the order of a few k_BT, is much lower compared to the area compressibility modulus, which is around 0.1 N/m [83]. At larger deformations, stretching of the bilayer and deformation of the elastic core become more significant. Therefore, an appropriate description of cell mechanics should depend on the magnitude of the deformation. For small deformations, the contribution of the biomembrane should not be neglected. However, in larger cell deformations, the cell can be described as an elastic continuum. The observed variations in the measured data suggest that factors beyond pure deformation influence the behavior of the model cell. Cell adhesion generates membrane prestrain and alters cell geometry [134]. Other factors include variations in the cytosolic elastic modulus or indentation position relative to the cell [135]. We further assumed both PBS and HA solutions to be incompressible (Poisson's ratio = 0.5). Therefore, the cell shape, which determines the biomembrane stretch, is identical at a given indentation depth. If the HA Poisson ratio was lower, the deformation of the PBS and HA-filled liposomes would not be the same. The loading rate can also influence the elastic modulus, a known behavior for viscoelastic materials [136]. Therefore, our conclusions are valid only for the small indentation rate used in this study. When measuring live cells, the active response due to cytoskeletal remodeling should also be considered [127]. Additionally, our results were obtained using a colloidal force probe. The shape of the tip can influence the measured values, as previously shown [137]. Finally, all measurements were performed on large unilamellar

liposomes like the size of living cells. In smaller liposomes, the relative stretch at a given indentation depth is larger, resulting in higher stiffness [138][142].

One of our primary objectives was to compare the mechanical properties of liposomes using various techniques, including AFM, nanoindentation, and compression testing [28] . While nanoindentation is commonly employed to assess the mechanical properties of cells [43], its application to liposomes has not been verified in our experimental setup. Additionally, we conducted mechanical testing of liposomes using the microindenter compression test with extended tip movement. However, due to the limited number of liposome samples tested (only 5 liposomes), statistical analysis could not be performed.

In this study, we investigated the mechanical properties of liposomes using four analytical models. Straight line fitting, the Hertzian model, and two origined models – the prescribed shape model and the fluid shell model – were employed to analyze the force-displacement curves obtained through indentation. We specifically determined the stiffness of the liposomes using linear regression, Young's modulus using the Hertz model, and the area compressibility modulus (K_A) using our models [141][146][156]. All measurements were subjected to static analysis to ensure the accuracy and reproducibility of the results.

The measured force-displacement curves were categorized into three groups: linear, nonlinear, and background (Fig. 64). Liposomes exhibiting linear behavior displayed a significantly higher stiffness compared to those with a nonlinear force curve. This observation could be attributed to adhesion and pre-existing tension in the membrane, as suggested by Schaffer et al. [102]. Since the evaluated models were developed for spherical liposomes without adhesion, liposomes with a linear stiffness response were excluded from further analysis.

We estimated the constitutive parameters for liposomes filled with phosphate-buffered saline (PBS) and hyaluronic acid (HA) at indentation forces of 1 nN, 3 nN, and 5 nN. The repeatability of the measurements was assessed at 5 nN. An ideal constitutive parameter should be independent of the liposome's geometrical features or indentation depth. However, the measured stiffness increased with indentation depth, indicating a nonlinear response (Fig. 72). Similar behaviour has been reported in previous studies using atomic force microscopy (AFM) on both live cells [62] and cell models [156].

Interestingly, the parameter that remained independent of indentation depth was the Young's modulus estimated using the Hertz model (Fig. 71). The prescribed shape model predicted a strong correlation between indentation depth and the area compressibility modulus, but also exhibited the lowest repeatability among the models. At higher deformations, the prescribed shape model predicted unrealistically low area compressibility moduli (Tab. 14). Therefore, this model appears to be inconsistent with the experimental observations. In contrast, the fluid shell model, employing the same constitutive parameter, demonstrated no depth dependence and excellent repeatability. Consequently, this model warrants further investigation.

Our research demonstrates the potential of filled liposomes as a standard for mechanical testing, opening new avenues for future studies. The results suggest that generating liposomes with uniform size using a portable microfluidic device would be beneficial for establishing a reliable reference standard. A promising upgrade to our experimental setup could involve the utilization of a reaction-in-a-centrifuge (RIAC) device, which leverages centrifugal force to induce controlled flow within microfluidic channels. This production method offers advantages in both affordability and time efficiency.

Our preliminary studies indicate that HA-incorporated liposomes could serve as an effective drug delivery system for treating osteoarthritis. To create a more intricate cell model, incorporating the cytoskeleton and cell nucleus, represented by an actin cortical mesh or a stiff element fabricated using a multi-level microfluidic device, could be valuable.

9 Conclusion

This study presents a two-stage microfluidic device utilizing the double emulsion drop method for the efficient and controlled production of liposomes with varying compositions. This microfluidic approach offers a cost-effective and time-saving method compared to traditional techniques. We demonstrate the versatility of this approach by generating two types of liposomes: one encapsulating phosphate-buffered saline (PBS) and another mimicking the viscous cytoplasm by incorporating hyaluronic acid (HA). These liposomes serve as artificial cell models for the investigation of their mechanical properties [119][142].

Atomic force microscopy (AFM) was employed to acquire force-deformation curves of individual liposomes. Statistical analysis confirmed the high reproducibility of measurements obtained using these cell models. To further enhance the reliability of single-cell mechanics methods, identifying potential sources of variability between individual cells is crucial. Aside from inherent physiological variations, the testing methodology and subsequent data processing can introduce technical variability. Based on the acquired measurements, it becomes evident that cell size, a factor neglected in the Hertz model's fundamental assumptions, significantly impacts the measured stiffness and estimated Young's modulus. Therefore, comparisons between individual cells should involve cells with comparable sizes.

We further investigated the load-bearing ratio between the cytoplasm and the biomembrane. Our observations revealed a near 1:1 ratio at minimal indentation depths (less than 0.2 µm). However, this ratio progressively increases to a steady 4:1 at greater indentation depths (> 0.2 µm). These findings support the applicability of the continuum approach for analyzing cell mechanics at larger deformations. Conversely, at minimal deformations, the contribution of the cell membrane becomes significant and necessitates its inclusion in the analysis.

To emphasize the importance of the biomembrane, we introduce two novel models: the prescribed shape model, based on the geometrical deformation of the liposome, and the fluid shell model, which incorporates the Laplace equation for a fluid membrane. These models acknowledge stretching as the primary deformation mode. Deviating from conventional continuum mechanics models, this innovative approach considers the entirety of the cell deformation and offers predictions regarding the contact area between the AFM tip and the substrate. Both models accurately reflect the size-dependent relationship between liposome indentation force. However, the prescribed shape model exhibits a dependence of the constitutive parameter on indentation depth and lower repeatability. We may conclude that the fluid shell model is better suited for DDPC liposomes, and the resulting material properties align with established literature values.

Our research demonstrates the potential of utilizing experimental models to examine key characteristics of cell mechanics. Further research is warranted to develop an experimental model that accurately represents specific living cells with intricate internal structures.

Bibliography

[1] FLETCHER, Daniel A.; MULLINS, R. Dyche. Cell mechanics and the cytoskeleton [online]. Nature, 2010, 463.7280: 485-492. [Accessed. 13.12.2023]. Available at: https://doi.org/10.1038/nature08908

[2] Bose, D. Six main cell functions [online]. Sciencing, 2019, [Accessed. 13.12.2023]. Available at: https://sciencing.com/six-main-cell-functions-6891800.html

[3] QUAN, Fu-Shi; KIM, Kyung Sook. Medical applications of the intrinsic mechanical properties of single cells [online]. Acta biochimica et biophysica Sinica, 2016, 48.10: 865-871. [Accessed. 13.12.2023]. Available at: https://doi.org/10.1093/abbs/gmw081

[4] DE PASCALIS, Chiara; ETIENNE-MANNEVILLE, Sandrine. Single and collective cell migration: the mechanics of adhesions [online]. Molecular biology of the cell, 2017, 28.14: 1833-1846. [Accessed. 13.12.2023]. Available at :https://doi.org/10.1091/mbc.e17-03-0134

[5] BOLSOVER, Stephen R., et al. Cell biology: a short course [online]. John Wiley & Sons, 2011, [Accessed. 13.12.2023]. Available at: http://www.bio-nica.info/Biblioteca/Bolsover2004CellBiology.pdf

[6] ALBERTS, Bruce. Molecular biology of the cell. Garland science, 2017,

[7] Cell structure [online]. BrainKart. [Accessed. 13.12.2023]. Available at: https://www.brainkart.com/article/Cell-Structure_21751/

[8] Bailey, R. Function, structure, and composition of the cell membrane [online]. ThoughtCo, 2019, [Accessed. 13.12.2023]. Available at: https://www.thoughtco.com/cell-membrane-373364

[9] PANDEY, Himanshu; RANI, Radha; AGARWAL, Vishnu. Liposome and their applications in cancer therapy [online]. Brazilian archives of biology and technology, 2016, 59. [Accessed. 13.12.2023]. Available at: https://doi.org/10.1590/1678-4324-2016150477

[10] SHASHI, Kant, et al. A complete review on: Liposomes. International research journal of pharmacy, 2012, 3.7: 10-16.

[11] LOWE, Lauren A.; LOO, Daniel WK; WANG, Anna. Methods for forming Giant Unilamellar fatty acid vesicles. Membrane Lipids: Methods and Protocols, 2022, 1-12.

[12] BioExplorer. Phospholipid bilayer: Lipid bilayer: Structures & functions [online]. Bio Explorer, 2018, [Accessed. 13.12.2023]. Available at: https://www.bioexplorer.net/phospholipid-bilayer.html/

[13] TOSAKA, Toshiyuki; KAMIYA, Koki. Function Investigations and Applications of Membrane Proteins on Artificial Lipid Membranes [online]. International Journal of Molecular Sciences, 2023, 24.8: 7231. [Accessed. 13.12.2023]. Available at: https://doi.org/10.3390/ijms24087231

[14] KOTOUČEK, Jan, et al. Preparation of nanoliposomes by microfluidic mixing in herring-bone channel and the role of membrane fluidity in liposomes formation [online]. Scientific reports, 2020, 10.1: 5595. [Accessed. 13.12.2023]. Available at: https://www.nature.com/articles/s41598-020-62500-2

[15] DUA, J. S.; RANA, A. C.; BHANDARI, A. K. Liposome: methods of preparation and applications [online]. International Journal of Pharmaceutical Studies and Research, 2012, 3.2: 14-20. [Accessed. 13.12.2023]. Available at: https://romanpub.com/resources/ijpsr%20v11-2020-6.pdf

[16] KURIBAYASHI, K., et al. Electroformation of giant liposomes in microfluidic channels [online]. Measurement science and technology, 2006, 17.12: 3121. [Accessed. 13.12.2023]. Available at: https://iopscience.iop.org/article/10.1088/0957-0233/17/12/S01/pdf

[17] CARUGO, Dario, et al. Liposome production by microfluidics: potential and limiting factors [online]. Scientific reports, 2016, 6.1: 25876. [Accessed. 13.12.2023]. Available at: https://doi.org/10.1038/srep25876

[18] YU, Bo; LEE, Robert J.; LEE, L. James. Microfluidic methods for production of liposomes [online]. Methods in enzymology, 2009, 465: 129-141. [Accessed. 13.12.2023]. Available at: https://doi.org/10.1016/S0076-6879(09)65007-2

[19] YANG, Yong, et al. Engineering of a microfluidic cell culture platform embedded with nanoscale features [online]. Lab on a Chip, 2011, 11.9: 1638-1646. . [Accessed. 13.12.2023]. Available at: https://doi.org/10.1039/C0LC00736F

[20] UGOLINI, Giovanni Stefano, et al. Generating multicompartmental 3D biological constructs interfaced through sequential injections in microfluidic devices [online]. Advanced Healthcare Materials, 2017, 6.10: 1601170. [Accessed. 13.12.2023]. Available at: https://doi.org/10.1002/adhm.201601170

[21] JAHN, Andreas, et al. Microfluidic mixing and the formation of nanoscale lipid vesicles [online]. ACS nano, 2010, 4.4: 2077-2087. [Accessed. 13.12.2023]. Available at: https://doi.org/10.1021/nn901676x

[22] KAMIYA, Koki, et al. Cell-sized asymmetric lipid vesicles facilitate the investigation of asymmetric membranes [online]. Nature chemistry, 2016, 8.9: 881-889. [Accessed. 13.12.2023]. Available at: https://doi.org/10.1038/nchem.2537

[23] RODRIGUEZ, Marita L.; MCGARRY, Patrick J.; SNIADECKI, Nathan J. Review on cell mechanics: experimental and modeling approaches [online]. Applied Mechanics Reviews, 2013, 65.6: 060801. [Accessed. 13.12.2023]. Available at: https://doi.org/10.1115/1.4025355

[24] BACKHOLM, Matilda; BÄUMCHEN, Oliver. Micropipette force sensors for in vivo force measurements on single cells and multicellular microorganisms [online]. Nature protocols, 2019, 14.2: 594-615. [Accessed. 13.12.2023]. Available at: https://doi.org/10.1038/s41596-018-0110-x

[25] WANG, Haoqing, et al. Micropipette-based biomechanical nanotools on living cells [online]. European Biophysics Journal, 2022, 51.2: 119-133. [Accessed. 13.12.2023]. Available at: https://doi.org/10.1007/s00249-021-01587-5

[26] BINNIG, Gerd, et al. Energy-dependent state-density corrugation of a graphite surface as seen by scanning tunneling microscopy [online]. Europhysics letters, 1986, 1.1: 31. [Accessed. 13.12.2023]. Available at: https://iopscience.iop.org/article/10.1209/0295-5075/1/1/005/pdf

[27] DUFRÊNE, Yves F.; PELLING, Andrew E. Force nanoscopy of cell mechanics and cell adhesion [online]. Nanoscale, 2013, 5.10: 4094-4104. [Accessed. 13.12.2023]. Available at: https://doi.org/10.1039/C3NR00340J

[28] MORSHED, Adnan, et al. Mechanical characterization of vesicles and cells: A review [online]. Electrophoresis, 2020, 41.7-8: 449-470. [Accessed. 13.12.2023]. Available at: https://doi.org/10.1002/elps.201900362

[29] DENG, Xiangying, et al. Application of atomic force microscopy in cancer research [online]. Journal of nanobiotechnology, 2018, 16: 1-15. [Accessed. 13.12.2023]. Available at: https://doi.org/10.1186/s12951-018-0428-0

[30] GIMÉNEZ, Alícia, et al. Elastic properties of hydrogels and decellularized tissue sections used in mechanobiology studies probed by atomic force microscopy [online]. Microscopy research and technique, 2017, 80.1: 85-96. [Accessed. 14.12.2023]. Available at: https://doi.org/10.1002/jemt.22740

[31] RANA, Md Sohel; POTA, Hemanshu Roy; PETERSEN, Ian R. Improvement in the imaging performance of atomic force microscopy: A survey [online]. IEEE Transactions on Automation Science and Engineering, 2016, 14.2: 1265-1285. [Accessed. 14.12.2023]. Available at: https://ieeexplore.ieee.org/stamp/stamp.jsp?tp=&arnumber=7442178

[32] Advanced force distance curves [online]. AFM Workshop, [Accessed. 14.12.2023]. Available at: https://www.afmworkshop.com/afm-products/modes/afm-advanced-force-distance-curves

[33] Dwivedi, K. Types of hardness testing methods and impact testing [online]. Mechical, 2021, [Accessed. 14.12.2023]. Available at: https://www.mechical.com/2021/06/hardness-testing-methods.html

[34] Microindentation Testing [online]. MechAction, Inc. Expertise in Nanomechanical Testing, [Accessed. 14.12.2023]. Available at: https://www.mechaction.com/microindentation

[35] W. Su, D. Wei, Y. Qian, H. Huang and H. Zhao, A nanoindentation instrument for characterizing mechanical properties of materials under high-frequency vibration [online]. IEEE Transactions on Instrumentation and Measurement, 2023, [Accessed. 14.12.2023]. Available at: https://ieeexplore.ieee.org/stamp/stamp.jsp?tp=&arnumber=10313324

[36] MANN, Adrian B. Nanoindentation. In: Surfaces and interfaces for biomaterials. Woodhead Publishing, 2005, p. 225-247.

[37] FISCHER-CRIPPS, Anthony C.; NICHOLSON, D. W. Nanoindentation. Mechanical engineering series. Appl. Mech. Rev., 2004, 57.2: B12-B12.

[38] TSUI, Ting; VOLINSKY, Alex A. Small scale deformation using advanced nanoindentation techniques [online]. MDPI-Multidisciplinary Digital Publishing Institute, 2019, [Accessed. 14.12.2023]. Available at: https://mdpi-res.com/books/book/1333/Small_Scale_Deformation_using_Advanced_Nanoindentation_Techniques.pdf?filename=Small_Scale_Deformation_using_Advanced_Nanoindentation_Techniques.pdf

[39] WANG, Kaiqiang, et al. Quasi-static and dynamic nanoindentation of particle-reinforced soft composites [online]. Journal of Applied Polymer Science, 2017, 134.10. [Accessed. 14.12.2023]. Available at: https://doi.org/10.1002/app.44559

[40] OLASZ, Dániel, et al. Extended applications of the displacement-sensing indentation method [online]. Micromachines, 2020, 11.11: 1023. [Accessed. 14.12.2023]. Available at: https://doi.org/10.3390/mi11111023

[41] LIU, Kouqi, et al. Nano-dynamic mechanical analysis (nano-DMA) of creep behavior of shales: Bakken case study [online]. Journal of materials science, 2018, 53: 4417-4432. [Accessed. 14.12.2023]. Available at: https://doi.org/10.1007/s10853-017-1821-z

[42] KRÁLÍK, Vlastimil; NĚMEČEK, Jiří. Comparison of nanoindentation techniques for local mechanical quantification of aluminium alloy [online]. Materials Science and Engineering: A, 2014, 618: 118-128. [Accessed. 14.12.2023]. Available at: https://doi.org/10.1016/j.msea.2014.08.036

[43] SEPITKA, J., et al. Compression tests of a living cell: a contact detection problem [online]. Computer Methods in Biomechanics and Biomedical Engineering, 2014, 17.sup1: 40-41. [Accessed. 14.12.2023]. Available at: https://doi.org/10.1080/10255842.2014.931093

[44] ARFSTEN, J., et al. Compressive testing of single yeast cells in liquid environment using a nanoindentation system [online]. Journal of Materials Research, 2008, 23.12: 3153-3160. [Accessed. 14.12.2023]. Available at: https://doi.org/10.1557/JMR.2008.0383

[45] GUEVORKIAN, K.; MAÎTRE, J.-L. Micropipette aspiration: A unique tool for exploring cell and tissue mechanics in vivo [online]. In: Methods in cell biology. Academic Press, 2017, p. 187-201. [Accessed. 14.12.2023]. Available at: https://doi.org/10.1016/bs.mcb.2016.11.012

[46] NEUMAN, Keir C.; BLOCK, Steven M. Optical trapping [online]. Review of scientific instruments, 2004, 75.9: 2787-2809. [Accessed. 14.12.2023]. Available at: https://doi.org/10.1063/1.1785844

[47] BAUSCH, Andreas R., et al. Local measurements of viscoelastic parameters of adherent cell surfaces by magnetic bead microrheometry [online]. Biophysical journal, 1998, 75.4: 2038-2049. [Accessed. 14.12.2023]. Available at: https://doi.org/10.1016/S0006-3495(98)77646-5

[48] HUANG, Yunfei, et al. Traction force microscopy with optimized regularization and automated Bayesian parameter selection for comparing cells [online]. Scientific reports, 2019, 9.1: 539. [Accessed. 14.12.2023]. Available at: https://doi.org/10.1038/s41598-018-36896-x

[49] KONTOMARIS, S. V.; MALAMOU, A. Hertz model or Oliver & Pharr analysis? Tutorial regarding AFM nanoindentation experiments on biological samples [online]. Materials Research Express, 2020, 7.3: 033001. [Accessed. 14.12.2023]. Available at: https://iopscience.iop.org/article/10.1088/2053-1591/ab79ce/meta

[50] TIMOSHENKO, S.; GOODIER, J. N. Theory of Elasticity, McGraw Hill Inc. 1951

[51] POPOV, Valentin L., et al. Contact mechanics and friction [online]. Berlin: Springer Berlin Heidelberg, 2010, [Accessed. 14.12.2023]. Available at: https://link.springer.com/content/pdf/10.1007/978-3-662-53081-8.pdf

[52] HERTZ, Heinrich. Ueber die Berührung fester elastischer Körper. 1882.

[53] JOHNSON, K. L. Contact mechanics cambridge univ. *Press, Cambridge*, 1985, 95.365: 922.

[54] KONTOMARIS, Stylianos-Vasileios, et al. A discussion regarding the approximation of cylindrical and spherical shaped samples as half spaces in AFM nanoindentation experiments [online]. Materials Research Express, 2018, 5.8: 085402. [Accessed. 14.12.2023]. Available at: https://iopscience.iop.org/article/10.1088/2053-1591/aad2c9/meta

[55] OVERBECK, Achim, et al. Compression Testing and Modeling of Spherical Cells–Comparison of Yeast and Algae [online]. Chemical Engineering & Technology, 2017, 40.6: 1158-1164. [Accessed. 14.12.2023]. Available at: https://doi.org/10.1002/ceat.201600145

[56] MARTÍNEZ-BALBUENA, L., et al. Application of the Helfrich elasticity theory to the morphology of red blood cells [online]. American Journal of Physics, 2021, 89.5: 465-476. [Accessed. 14.12.2023]. Available at: https://doi.org/10.1119/10.0003452

[57] CANHAM, Peter B. The minimum energy of bending as a possible explanation of the biconcave shape of the human red blood cell [online]. Journal of theoretical biology, 1970, 26.1: 61-81. [Accessed. 14.12.2023]. Available at: https://doi.org/10.1016/S0022-5193(70)80032-7

[58] KIRCHHAUSEN, Tom. Bending membranes. Nature Cell Biology. 2012, 14(9), 906- 908. ISSN 1476-4679.

[59] CAMPELO, Felix, MALHOTRA, Vivek. Membrane Fission: the Biogenesis of Transport Carriers. Annual Review of Carriers [online]. Annual Review of Biochemistry, 2012, 81(1), 407–427. ISSN 0066-4154. [Accessed. 14.12.2023]. Available at: https://doi.org/10.1146/annurev-biochem-051710-094912

[60] BIAN, Xin, LITVINOV, Sergey, KOUMOUTSAKOS, Petros. Bending models of lipid bilayer membranes: Spontaneous curvature and area-difference elasticity [online]. Computer Methods in Applied Mechanics and Engineering, 2020, 359, 112758. ISSN 0045-7825. [Accessed. 14.12.2023]. Available at: https://doi.org/10.1016/j.cma.2019.112758

[61] YUSIFLI, Elmar, et al. Embedded Cell Count Algorithm for Cultured Tissue Characterization [online]. IFAC-PapersOnLine, 2018, 51.30: 683-687. [Accessed. 14.12.2023]. Available at: https://doi.org/10.1016/j.ifacol.2018.11.221

[62] KRIEG, Michael, et al. Atomic force microscopy-based mechanobiology [online]. Nature Reviews Physics, 2019, 1.1: 41-57. [Accessed. 14.12.2023]. Available at: https://doi.org/10.1038/s42254-018-0001-7

[63] LECLAIRE, Michael; GIMZEWSKI, James; SHARMA, Shivani. A review of the biomechanical properties of single extracellular vesicles [online]. Nano select, 2021, 2.1: 1-15. [Accessed. 14.12.2023]. Available at: https://www.proquest.com/openview/8737a146a784382b456c8e4ed4a4f0f9/1?pq-origsite=gscholar&cbl=18750&diss=y

[64] ROOS, W. H.; BRUINSMA, R.; WUITE, G. J. L. Physical virology [online]. Nature physics, 2010, 6.10: 733-743. [Accessed. 14.12.2023]. Available at: https://doi.org/10.1002/wnan.1613

[65] VORSELEN, Daan, et al. Competition between bending and internal pressure governs the mechanics of fluid nanovesicles [online]. ACS nano, 2017, 11.3: 2628-2636. [Accessed. 14.12.2023]. Available at: https://doi.org/10.1021/acsnano.6b07302

[66] DOKTOROVA, Milka, et al. A new computational method for membrane compressibility: Bilayer mechanical thickness revisited. *Biophysical journal*, 2019, 116.3: 487-502.

[67] LIANG, Xuemei; MAO, Guangzhao; NG, KY Simon. Probing small unilamellar EggPC vesicles on mica surface by atomic force microscopy [online]. Colloids and Surfaces B: Biointerfaces, 2004, 34.1: 41-51. [Accessed. 14.12.2023]. Available at: https://doi.org/10.1016/j.colsurfb.2003.10.017

[68] LANEY, Daniel E., et al. Changes in the elastic properties of cholinergic synaptic vesicles as measured by atomic force microscopy [online]. Biophysical Journal, 1997, 72.2: 806-813. [Accessed. 14.12.2023]. Available at: https://www.cell.com/biophysj/pdf/S0006-3495(97)78714-9.pdf

[69] S. Sharma, V. Palanisamy, C. Mathisen, M. Schmidt, J. K. Gimzewski, Global J Phys Chem, 2011, 2, 4.

[70] ZHANG, Haiying, et al. Identification of distinct nanoparticles and subsets of extracellular vesicles by asymmetric flow field-flow fractionation [online]. Nature cell biology, 2018, 20.3: 332-343. [Accessed. 14.12.2023]. Available at: https://doi.org/10.1038/s41556-018-0040-4

[71] WHITEHEAD, Bradley, et al. Tumour exosomes display differential mechanical and complement activation properties dependent on malignant state: implications in endothelial leakiness [online]. Journal of extracellular vesicles, 2015, 4.1: 29685. [Accessed. 14.12.2023]. Available at: https://doi.org/10.3402/jev.v4.29685

[72] ROYO, Felix, et al. Differences in the meTabolite composition and mechanical properties of extracellular vesicles secreted by hepatic cellular models [online]. Journal of extracellular vesicles, 2019, 8.1: 1575678. [Accessed. 14.12.2023]. Available at: https://doi.org/10.1080/20013078.2019.1575678

[73] VORSELEN, Daan, et al. The fluid membrane determines mechanics of erythrocyte extracellular vesicles and is softened in hereditary spherocytosis [online]. Nature communications, 2018, 9.1: 4960. [Accessed. 14.12.2023]. Available at: https://doi.org/10.1038/s41467-018-07445-x

[74] JAHN, Andreas, et al. Microfluidic mixing and the formation of nanoscale lipid vesicles [online]. ACS nano, 2010, 4.4: 2077-2087. [Accessed. 14.12.2023]. Available at: https://doi.org/10.1021/nn901676x

[75] UNGAI-SALÁNKI, Rita, et al. Nanonewton scale adhesion force measurements on biotinylated microbeads with a robotic micropipette [online]. Journal of Colloid and Interface Science, 2021, 602: 291-299. [Accessed. 14.12.2023]. Available at: https://doi.org/10.1016/j.jcis.2021.05.180

[76] RUOZI, Barbara, et al. Application of atomic force microscopy to characterize liposomes as drug and gene carriers [online]. Talanta, 2007, 73.1: 12-22. [Accessed. 14.12.2023]. Available at: https://doi.org/10.1016/j.talanta.2007.03.031

[77] VORSELEN, Daan, et al. Mechanical characterization of liposomes and extracellular vesicles, a protocol [online]. Frontiers in molecular biosciences, 2020, 7: 139. [Accessed. 14.12.2023]. Available at: https://doi.org/10.3389/fmolb.2020.00139

[78] THOMAS, Gawain, et al. Measuring the mechanical properties of living cells using atomic force microscopy [online]. JoVE (Journal of Visualized Experiments), 2013, 76: e50497. [Accessed. 14.12.2023]. Available at: https://www.jove.com/t/50497/measuring-mechanical-properties-living-cells-using-atomic-force

[79] Determining the elastic modulus of biological sample using atomic force microscopy – AFM JPK [online]. [Accessed. 14.12.2023]. Available at: https://www.bruker.com/en/products-and-solutions/microscopes/bioafm/resource-library/determining-the-elastic-modulus-of-biological-samples-using-the-atomic-force-microscope.html

[80] OVERBECK, A.; KAMPEN, I.; KWADE, A. Mechanical characterization of yeast cells: effects of growth conditions [online]. Letters in Applied Microbiology, 2015, 61.4: 333-338. [Accessed. 14.12.2023]. Available at: https://doi.org/10.1111/lam.12468

[81] HERDA, Martin: Analýza mechanických vlastností živých buněk: Diplomová práce. Praha. FS CVUT, 2019. 35 s.

[82] Israelachvili JN. Intermolecular and Surface Forces. Book. Elsevier, 2021, Pages 635-660. ISBN: 978-0-12-375182-9. doi.org/10.1016/C009-0-21560-1

[83] Boal, D. Mechanics of the Cell. In: Africa (Lond). Cambridge: Cambridge University Press. 1-19. 2002. ISBN: 0 521 79681 4

[84] EVANS, E. As; WAUGH, R.; MELNIK, L. Elastic area compressibility modulus of red cell membrane [online]. Biophys J. Vol. 16. 585-95. 1972. [Accessed. 14.12.2023]. Available at: https://www.cell.com/biophysj/pdf/S0006-3495(76)85713-X.pdf

[85] Evans EA, Skalak R. Mechanics and Thermodynamics of Biomembranes. CRC Press; 1978. DOI: 10.1201/9781351074339.

[86] DANIEL, Matej, et al. Clustering and separation of hydrophobic nanoparticles in lipid bilayer explained by membrane mechanics [online]. Scientific Reports, 2018, 8.1: 10810. [Accessed. 14.12.2023]. Available at: https://doi.org/10.1038/s41598-018-28965-y

[87] MARTÍNEZ-BALBUENA, L., et al. Application of the Helfrich elasticity theory to the morphology of red blood cells [online]. American Journal of Physics, 2021, 89.5: 465-476. [Accessed. 14.12.2023]. Available at: https://doi.org/10.1119/10.0003452

[88] DANIEL, Matej, et al. Modelling the role of membrane mechanics in cell adhesion on titanium oxide nanotubes [online]. Computer Methods in Biomechanics and Biomedical Engineering, 2023, 26.3: 281-290. [Accessed. 14.12.2023]. Available at: https://doi.org/10.1080/10255842.2022.2058875

[89] Barton. AFM Cohesion Parameters. In: Meyers RA, editor. Encyclopedia of Physical Science and Technology (Third Edition). New York: Academic Press. 233-51. 2003. ISBN-13: 9780122274107

[90] Madahar KV. Calculus and geometry [online]. SpringerLink, 2013, [Accessed. 14.12.2023]. Available at: https://doi.org/10.1007/s12045-013-0084-5

[91] Bates, D., M¨achler, M., Bolker, B., & Walker, S. 2015, Fitting Linear Mixed-Effects Models Using lme4. J. Stat. Softw., 67, 1–48.

[92] Beer FP, Johnston ER, DeWolf JT, Mazurek DF. Mechanics of Materials. Eighth edition ed. New York, NY: McGraw-Hill Education; 57-123. 2020, ISBN 978-0-07-338028-5

[93] Al- JAMAL, Wafa'T.; KOSTARELOS, Kostas. Liposomes: from a clinically established drug delivery system to a nanoparticle platform for theranostic nanomedicine [online]. Accounts of chemical research, 2011, 44.10: 1094-1104. [Accessed. 14.12.2023]. Available at: https://doi.org/10.1021/ar200105p

[94] LIM, C. T.; ZHOU, E. H.; QUEK, S. T. Mechanical models for living cells—a review [online]. Journal of biomechanics, 2006, 39.2: 195-216. [Accessed. 14.12.2023]. Available at: https://doi.org/10.1016/j.jbiomech.2004.12.008

[95] NARASIMHAN, Badri Narayanan, et al. Mechanical characterization for cellular mechanobiology: current trends and future prospects [online]. Frontiers in Bioengineering and Biotechnology, 2020, 8: 595978. [Accessed. 14.12.2023]. Available at: https://doi.org/10.3389/fbioe.2020.595978

[96] KUZNETSOVA, Tatyana G., et al. Atomic force microscopy probing of cell elasticity [online]. Micron, 2007, 38.8: 824-833. [Accessed. 14.12.2023]. Available at: https://doi.org/10.1016/j.micron.2007.06.011

[97] PÉREZ-DOMÍNGUEZ, Sandra, et al. Atomic force microscopy for cell mechanics and diseases [online]. Neuroforum, 2020, 26.2: 101-109. [Accessed. 14.12.2023]. Available at: https://doi.org/10.1515/nf-2020-0001

[98] BOTET-CARRERAS, Adria, et al. Engineering and development of model lipid membranes mimicking the HeLa cell membrane [online]. Colloids and Surfaces A: Physicochemical and Engineering Aspects, 2021, 630: 127663. [Accessed. 14.12.2023]. Available at: https://doi.org/10.1016/j.colsurfa.2021.127663

[99] MOZAFARI, M. Reza. Liposomes: an overview of manufacturing techniques. Cellular and molecular biology letters, 2005, 10.4: 711.

[100] YU, Bo; LEE, Robert J.; LEE, L. James. Microfluidic methods for production of liposomes [online]. Methods in enzymology, 2009, 465: 129-141. [Accessed. 14.12.2023]. Available at: https://doi.org/10.1016/S0076-6879(09)65007-2

[101] ALAPAN, Yunus, et al. Three-dimensional printing based hybrid manufacturing of microfluidic devices [online]. Journal of Nanotechnology in Engineering and Medicine, 2015, 6.2: 021007. [Accessed. 14.12.2023]. Available at: https://doi.org/10.1115/1.4031231

[102] SCHÄFER, Edith, et al. Mechanical response of adherent giant liposomes to indentation with a conical AFM-tip [online]. Soft Matter, 2015, 11.22: 4487-4495. [Accessed. 14.12.2023]. Available at: https://pubs.rsc.org/en/content/articlehtml/2015/sm/c5sm00191a

[103] TERZI, M. Mert; DESERNO, Markus; NAGLE, John F. Mechanical properties of lipid bilayers: A note on the Poisson ratio [online]. Soft matter, 2019, 15.44: 9085-9092. [Accessed. 14.12.2023]. Available at: https://pubs.rsc.org/en/content/articlelanding/2019/sm/c9sm01290g/unauth

[104] DELORME, Nicolas; FERY, Andreas. Direct method to study membrane rigidity of small vesicles based on atomic force microscope force spectroscopy [online]. Physical Review E, 2006, 74.3: 030901. [Accessed. 14.12.2023]. Available at: https://doi.org/10.1103/PhysRevE.74.030901

[105] DELORME, Nicolas, et al. Surface immobilization and mechanical properties of catanionic hollow faceted polyhedrons [online]. The Journal of Physical Chemistry B, 2006, 110.4: 1752-1758. [Accessed. 14.12.2023]. Available at: https://doi.org/10.1021/jp054473

[106] EFREMOV, Yuri M., et al. 3D nanomechanical mapping of subcellular and sub-nuclear structures of living cells by multi-harmonic AFM with long-tip microcantilevers [online]. Scientific Reports, 2022, 12.1: 529. [Accessed. 14.12.2023]. Available at: https://doi.org/10.1038/s41598-021-04443-w

[107] REN, Keli; GAO, Jingwei; HAN, Dong. AFM force relaxation curve reveals that the decrease of membrane tension is the essential reason for the softening of cancer cells [online]. Frontiers in Cell and Developmental Biology, 2021, 9: 663021. [Accessed. 14.12.2023]. Available at: https://doi.org/10.3389/fcell.2021.663021

[108] XIE, Kenan; YANG, Yuehua; JIANG, Hongyuan. Controlling cellular volume via mechanical and physical properties of substrate [online]. Biophysical journal, 2018, 114.3: 675-687. [Accessed. 14.12.2023]. Available at: https://www.cell.com/biophysj/pdf/S0006-3495(17)35047-6.pdf

[109] NEHLS, Stefan, et al. Stiffness of MDCK II cells depends on confluency and cell size [online]. Biophysical journal, 2019, 116.11: 2204-2211. [Accessed. 14.12.2023]. Available at: https://pubmed.ncbi.nlm.nih.gov/31126583/

[110] LIM, C. T.; ZHOU, E. H.; QUEK, S. T. Mechanical models for living cells—a review [online]. Journal of biomechanics, 2006, 39.2: 195-216. [Accessed. 14.12.2023]. Available at: https://doi.org/10.1016/j.jbiomech.2004.12.008

[111] EVANS, Arthur A., et al. Geometric localization of thermal fluctuations in red blood cells [online]. Proceedings of the National Academy of Sciences, 2017, 114.11: 2865-2870. [Accessed. 14.12.2023]. Available at: https://doi.org/10.1073/pnas.1613204114

[112] VESELÝ, Jan, et al. Constitutive modeling of human saphenous veins at overloading pressures [online]. Journal of the mechanical behavior of biomedical materials, 2015, 45: 101-108 [Accessed. 14.12.2023]. Available at: https://doi.org/10.1016/j.jmbbm.2015.01.023

[113] SANCHO, Ana, et al. A new strategy to measure intercellular adhesion forces in mature cell-cell contacts [online]. Scientific reports, 2017, 7.1: 46152. [Accessed. 14.12.2023]. Available at: https://doi.org/10.1038/srep46152

[114] RODRIGUEZ, Marita L.; MCGARRY, Patrick J.; SNIADECKI, Nathan J. Review on cell mechanics: experimental and modeling approaches [online]. Applied Mechanics Reviews, 2013, 65.6: 060801. [Accessed. 14.12.2023]. Available at: https://doi.org/10.1115/1.4025355

[115] MESAREC, Luka, et al. On the role of curved membrane nanodomains and passive and active skeleton forces in the determination of cell shape and membrane budding [online]. International journal of molecular sciences, 2021, 22.5: 2348. [Accessed. 14.12.2023]. Available at: https://doi.org/10.3390/ijms22052348

[116] SVETINA, Saša. Theoretical bases for the role of red blood cell shape in the regulation of its volume [online]. Frontiers in physiology, 2020, 11: 544. [Accessed. 14.12.2023]. Available at: https://doi.org/10.3389/fphys.2020.00544

[117] DEULING, Heinz J.; HELFRICH, Wolfgang. Red blood cell shapes as explained on the basis of curvature elasticity [online]. Biophysical journal, 1976, 16.8: 861-868. [Accessed. 14.12.2023]. Available at: https://www.cell.com/biophysj/pdf/S0006-3495(76)85736-0.pdf

[118] TIAN, Jie; LI, Yinghui; ZHAO, Dingsheng. Basics of Molecular Biology [online]. Molecular Imaging: Fundamentals and Applications, 2013, 541-601. [Accessed. 14.12.2023]. Available at: https://doi.org/10.1007/978-3-642-34303-2_16

[119] MARCOTTI, Stefania; REILLY, Gwendolen C.; LACROIX, Damien. Effect of cell sample size in atomic force microscopy nanoindentation [online]. Journal of the Mechanical Behavior of Biomedical Materials, 2019, 94: 259-266. [Accessed. 14.12.2023]. Available at: https://doi.org/10.1016/j.jmbbm.2019.03.018.

[120] DRABIK, Dominik, et al. Mechanical properties determination of DMPC, DPPC, DSPC, and HSPC solid-ordered bilayers [online]. Langmuir, 2020, 36.14: 3826-3835. [Accessed. 14.12.2023]. Available at: https://doi.org/10.1021/acs.langmuir.0c00475

[121] ZHANG, Xiaofei, et al. Rapid characterization of the biomechanical properties of drug-treated cells in a microfluidic device. Journal of Micromechanics and Microengineering, 2015, 25.10: 105004.

[122] MACDONALD, Niall P., et al. Comparing microfluidic performance of three-dimensional (3D) printing platforms. Analytical chemistry, 2017, 89.7: 3858-3866.

[123] J. Wang, M. Liu, Y. Shen, J. Sun, Z. Shao, D. Czajkowsky, Compressive Force Spectroscopy: From Living Cells to Single Proteins, International Journal of Molecular Sciences 19 (2018) 960. doi:10.3390/ijms19040960.

[124] S. Kwon, W. Yang, D. Moon, K. S. Kim, Comparison of Cancer Cell Elasticity by Cell Type, Journal of Cancer 11 (18) (2020) 5403. doi:10.7150/jca.45897.

[125] R. Lopes dos Santos, C. Campillo, Studying actin-induced cell shape changes using Giant Unilamellar Vesicles and reconstituted actin net- works, Biochemical Society Transactions 50 (5) (2022) 1527–1539. doi:10.1042/BST20220900.

[126] A. Singh, S. Thale, T. Leibner, L. Lamparter, A. Ricker, H. Nüse, J. Klin- gauf, M. Galic, M. Ohlberger, M. Matis, Dynamic interplay of micro- tubule and actomyosin forces drive tissue extension, Nature Communica- tions 15 (1) (2024) 3198. doi:10.1038/s41467-024-47596-8.

[127] V. Rajagopal, W. R. Holmes, P. V. S. Lee, Computational modeling of single-cell mechanics and cytoskeletal mechanobiology, WIREs Systems Bi- ology and Medicine 10 (2) (2018) e1407. doi:10.1002/wsbm.1407.

[128] N. Makarova, I. Sokolov, Cell mechanics can be robustly derived from AFM indentation data using the brush model: Error analysis, Nanoscale 14 (11) (2022) 4334–4347. doi:10.1039/D2NR00041E.

[129] C. T. Lim, E. H. Zhou, S. T. Quek, Mechanical models for liv- ing cells—a review, Journal of Biomechanics 39 (2) (2006) 195–216. doi:10.1016/j.jbiomech.2004.12.008.

[130] S. Sen, S. Subramanian, D. E. Discher, Indentation and Adhesive Probing of a Cell Membrane with AFM: Theoretical Model and Experiments, Biophysical Journal 89 (5) (2005) 3203-3213. doi:10.1529/biophysj.105.063826.

[131] L. M. Siqveland, S. M. Skjaeveland, Derivations of the Young-Laplace equa- tion, Capillarity 4 (2) (2021) 23–30. doi:10.46690/capi.2021.02.01.

[132] FLÄSCHNER, Gotthold, et al. Rheology of rounded mammalian cells over continuous high-frequencies. Nature Communications, 2021, 12.1: 2922.

[133] N. Guz, M. Dokukin, V. Kalaparthi, I. Sokolov, If Cell Mechanics Can Be Described by Elastic Modulus: Study of Different Models and Probes Used in Indentation Experiments, Biophysical Journal 107 (3) (2014) 564–575. doi:10.1016/j.bpj.2014.06.033.

[134] E. Sackmann, A. S. Smith, Physics of cell adhesion: Some lessons from cell-mimetic systems, Soft Matter 10 (11) (2014) 1644–1659. doi:10.1039/c3sm51910d.

[135] Q. S. Li, G. Y. H. Lee, C. N. Ong, C. T. Lim, AFM indentation study of breast cancer cells, Biochemical and Biophysical Research Communications 374 (4) (2008) 609–613. doi:10.1016/j.bbrc.2008.07.078.

[136] S. V. Kontomaris, A. Malamou, A. Stylianou, The Hertzian the- ory in AFM nanoindentation experiments regarding biological samples: Overcoming limitations in data processing, Micron 155 (2022) 103228. doi:10.1016/j.micron.2022.103228.

[137] S. G. Kulkarni, S. Pérez-Domínguez, M. Radmacher, Influence of can- tilever tip geometry and contact model on AFM elasticity measure- ment of cells, Journal of Molecular Recognition 36 (7) (2023) e3018. doi:10.1002/jmr.3018.

[138] H. Brochu, P. Vermette, Young's Moduli of Surface-Bound Liposomes by Atomic Force Microscopy Force Measurements, Langmuir 24 (5) (2008) 2009–2014. doi:10.1021/la702382d.

List of publications related to the dissertation thesis

Articles

[139] MENDOVÁ, K., M. DANIEL, and M. OTÁHAL. Nonlinear cell deformation model. Journal of Mechanical Engineering. 2023 ISSN 2450-5471. DOI 10.2478/scjme-2023-0026

[140] HILŠER, P., MENDOVÁ, K., et al. A new insight into more effective viscosupplementation based on the synergy of hyaluronic acid and phospholipids for cartilage friction reduction. Biotribology. 2021, 25(2352-5738), ISSN 2352-5738. DOI 10.1016/j.biotri.2021.100166

[141] MENDOVÁ, K., et al. Rethinking Hertz Model Interpretation for Cell Mechanics Using AFM. International Journal of Molecular Sciences. Manucsript number: ijms-3036525, Under Review., doi:10.20944/preprints202405.1183.v1

[142] MENDOVÁ, K., et al. Experimental evaluation of force distribution between cytoplasm and biomembrane. Journal of the Mechanical Behavior of Biomedical Materials. Manucsript number: JMBBM-D-24-00956, Under Review.

Book chapters

[143] MENDOVÁ, K., M. DANIEL, and J. ŘEZNÍČKOVÁ. Interactions between biomembrane embedded nanoparticles mediated by lipid bilayer [online]. In: Kordogiannis, G., ed. Advances in Biomembranes and Lipid Self-Assembly. Elsevier Inc, 2021. p. 1-16. ISSN 2451-9634. [Accessed. 14.12.2023]. Available at: https://doi.org/10.1016/bs.abl.2023.09.001

Conference proceedings

[144] M. OTÁHAL., MENDOVÁ, K, and M. DANIEL. AFM cell indentation: fluid shell model. In: Proceedings of 2023 EHealth and Bioengineering Conference (EHB). IEEE International Conference on e-Health and Bioengineering EHB 2023 - 11-th edition, Bucuresti, 2023-11-09/2023-11-10. Iasi: Gr. T. Popa University of Medicine and Pharmacy, 2023. ISBN 979-8-3503-2887-5

[145] MENDOVÁ, K., et al. 2v1: Lipozóm ako model bunky/nosič liečiv? In: KUBÁŠOVÁ, K., et al., eds. Human Biomechanics 2023 – Sborník. Human Biomechanics 2023, Doksy, Máchovo jezero, 2023-06-26/2023-06-28. Praha: České vysoké učení technické v Praze, Fakulta strojní, 2023. p. 7. ISBN 978-80-01-07179-3.

[146] MENDOVÁ, K., et al. Experimental and analytical evaluation of the biomechanics of liposomes. In: 24th International Scientific Conference Applied mechanics 2023 Book of abstracts. 24th International conference applied mechanics, Piešťany, 2023-04-19/2023-04-21. Bratislava: Strojnícka fakulta STU v Bratislave, 2023. p. 79-80. ISBN 978-80-227-5294-7.

[147] MENDOVÁ, K., et al. Znižujú lipozómy súčiniteľ trenia v chrupavke? In: SUCHÝ, T., et al., eds. Biomateriály a jejich povrchy XIV. Herbertov, Horní mlýn, 2021-09-14/2021-09-17. Praha: Czech Technical University in Prague, 2021. p. 9-92. 1. ISBN 978-80-01-06872-4.

[148] MENDOVÁ, K., et al. Experimental evaluation of liposomes biomechanics. In: KUBÁŠOVÁ, K. and Z. PADOVEC, eds. 29th Workshop of applied mechanics book of papers. 29th Workshop of Applied

Mechanics, Praha, 2021-11-05. Praha: CTU FME. Department of Mechanics, Biomechanics and Mechatronics, 2021. ISBN 978-80-01-06909-7.

[149] MENDOVÁ, K., M. DANIEL, and M. VRBKA. Vplyv lipozómov na súčiniteľ trenia v synoviálnych kĺboch. In: SUCHÝ, T., et al., eds. Biomateriály a jejich povrchy XIII. Biomateriály a jejich povrchy XIII, Herbertov, Horní mlýn, 2020-09-15/2020-09-18. Praha: Czech Technical University in Prague, 2020. ISBN 978-80-01-06754-3.

[150] MENDOVÁ, K., K. ELERŠIČ FILIPIČ, and M. DANIEL. Protocol of production of cell sized liposomes using microfluidic device and the effect of plasma treated glass on liposomes fixation. In: PELIKÁN, J., ed. 27th Workshop of Applied Mechanics - Proceedings. Praha: České vysoké učení technické v Praze, Fakulta strojní, 2019. ISBN 978-80-01-06680-5.

[151] MENDOVÁ, K., J. ŠEPITKA, and M. DANIEL. Mechanical properties of phospholipid layers. In: PADOVEC, Z. and J. VONDROVÁ, eds. 26th Workshop of Applied Mechanics. Praha, 2019-06-21. Praha: ČVUT v Praze, Fakulta strojní, Ústav mechaniky, biomechaniky a mechatroniky, 2019. ISBN 978-80-01-06604-1.

[152] MENDOVÁ, K. and P. RŮŽIČKA. Rapid development of microfluidic device using additive manufacturing. In: MORAVEC, J., ed. Studentská tvůrčí činnost 2019. Konference studentské tvůrčí činnosti 2019, Technická 4, Praha 6, 2019-04-09. Praha: České vysoké učení technické v Praze, Fakulta strojní, 2019. p. 15. ISBN 978- 80-01-06564-8. Available from: http://stc.fs.cvut.cz/docs/program_2019_a.pdf

[153] MENDOVÁ, K., M. DANIEL, and P. RŮŽIČKA. Development microfluidic device using additive manufacturing. In: VONDROVÁ, J. and Z. PADOVEC, eds. 24th Workshop of applied mechanics - book of papers. 24th Workshop of Applied Mechanics, ČVUT FS, 2018-06-08. Praha: CTU FME. Division of strength and elasticity, 2018. ISBN 978-80-01-06453-5.

[154] MENDOVÁ, K. and M. DANIEL. Principles of mechanical testing of cells. In: PELIKÁN, J., ed. 23rd Workshop of Applied Mechanics - Proceedings. 23rd Workshop of Applied Mechanics, Praha, 2017-12-15. Praha: České vysoké učení technické v Praze, Fakulta strojní, 2017. p. 20-21. ISBN 978-80-01-06372-9.

[155] MENDOVÁ, K. and M. DANIEL. Tvorba lipozómov mikrofluidným zariadením. In: SUCHÝ, T., et al., eds. Biomateriály a jejich povrchy X. Praha: Czech Technical University in Prague, 2017. p. 50-51. ISBN 978-80- 01-06195-4.

[156] MENDOVÁ, K., DANIEL M., ŠEPITKA J., AND OTÁHAL M. Mechanické vlastnosti buněk. In: XIV. mezinárodní konference Bioimplantologie. Praha: Národní knihovna ČR, 2023. ISBN 978-80-11-03134-3.

List of publications not related to the dissertation thesis

Conference proceedings

HORNÝ, L., et al. Hledání vhodného materiálu pro 3D tisk cévních náhrad. In: KUBÁŠOVÁ, K., et al., eds. Human Biomechanics 2023 – Sborník. Human Biomechanics 2023, Doksy, Máchovo jezero, 2023-06-26/2023-06-28. Praha: České vysoké učení technické v Praze, Fakulta strojní, 2023. p. 50-53. ISBN 978-80- 01-07179-3. Available from: http://www.biomechanika.cz/attachments/57.pdf

KRONEK, J., et al. 3D tisk resorbovatelného materiálu pro náhrady tepen a jeho mechanické testování. In: SUCHÝ, T., et al., eds. Biomateriály a jejich povrchy XVI. Herbertov, Vyšší Brod, 2023-09-19/2023-09-22. Praha: České vysoké učení technické v Praze, Fakulta strojní, 2023. p. 13. 1.. ISBN 978-80-01-07212-7.

ZOUFALÝ, O., K. MENDOVÁ, and M. DANIEL. Optimization of a 3d printed ankle-foot-orthosis. In: 24th international scientific conference applied mechanics 2023. Book of abstracts. 24th international conference applied mechanics, Piešťany, 2023-04-19/2023-04-21. Bratislava: Strojnícka fakulta STU v Bratislave, 2023. p. 137-138. ISBN 978-80-227-5294-7.

MENDOVÁ, K., et al. Mechanické vlastnosti 3D tlačeného polymérneho materiálu slúžiaceho na výrobu cievnej náhrady. In: SUCHÝ, T., et al., eds. Biomateriály a jejich povrchy XVI. Herbertov, Vyšší Brod, 2023- 09-19/2023-09-22. Praha: České vysoké učení technické v Praze, Fakulta strojní, 2023. p. 71-72. 1.. ISBN 978-80-01-07212-7.

MENDOVÁ, K., et al., eds. Vývoj 3D tlačných AFO ortéz. Herbertov, Horní Mlýn, 2022-09-13/2022-09-16. Praha: Czech Technical University in Prague, 2022. ISBN 978-80-01-07023-9.

MENDOVÁ, K., et al. Tensile properties of primary coating materials for fbg sensors. In: PADOVEC, Z., K. KUBÁŠOVÁ, and R. SEDLÁČEK, eds. 23rd International Scientific Conference Applied Mechanics 2022 Book of Abstracts. AM 2022 - Applied Mechanics, Liblice, 2022-04-04/2022-04-06. Praha: CTU FME. Department of Mechanics, Biomechanics and Mechatronics, 2022. p. 129-132. ISBN 978-80-01- 06974-5.

HORNÝ, L.; CHLUP, H.; MENDOVÁ, K.; SOBOTKA, Z.; PETŘIVÝ, Z.; KRONEK, J.; KOHAN, M.; BALINT, T. et al. Mechanical Properties of 3D Printed Resorbable Material for Manufacturing of Vascular Replacements In: Experimental Stress Analysis 2023 Proceedings

MENDOVÁ, K.; ZOUFALÝ, O.; RŮŽIČKA, P.; SEDLÁČEK, R.; DANIEL, M. Additive manufacturing of multimaterial medical devices (3D printed ankle- foot-orthosis). In: Applied Mechanics 2024. High Tatras, Slovakia.

Research Reports

CHLUP, H., et al. Tvorba a rozpustnost malých bublin plynu a jejich monitoring I. [Research Report] Praha: CTU FME. Department of Mechanics, Biomechanics and Mechatronics, 2020. Report no. 12105/20/25.

SCHMIDOVÁ, N., et al. Odborná zpráva o postupu prací a dosažených výsledcích za rok 2020. [Research Report] 2020. Report no. 12105/20/34

CHLUP, H., et al. Experimentální zjišťování charakteristik opt. vláken, FBG snímačů, materiálů primárních a sekundárních ochran. [Research Report] 2020. Report no. 12105/20/33.

SCHMIDOVÁ, N., et al. Odborná zpráva o postupu prací a dosažených výsledcích za rok 2021. [Research Report] 2021. Report no. 12105/21/29.

MENDOVÁ, K., et al. Mechanické vlastnosti lepených spojů s optickými vlákny. [Research Report] 2021. Report no. 12105/21/26.

SCHMIDOVÁ, N., et al. Odborná zpráva o postupu prací a dosažených výsledcích za rok 2022. [Research Report] 2022. Report no. 12105/22/04.

Functional Sample

LAZNOVÁ, V., et al. Upínací zařízení pro zatěžování vzorků s lepeným optickým vláknem. [Functional Sample] 2022.

SCHMIDOVÁ, N., et al. Zkušební zařízení pro testování optomechanických měřidel. [Functional Sample] 2022.

Zoufalý, O.; Mendová, K.; Daniel, M.; Džugan, J.; Síbr, M.; Sýkora, T. Funkční vzorek multimateriálové ortézy [Functional Sample] 2024.